BOSTON UNIVERSITY

GRADUATE SCHOOL OF ARTS AND SCIENCES

Dissertation

BOOSTED DARK MATTER

AND

ATMOSPHERIC NEUTRINO EARTH MATTER EFFECTS

AT SUPER-KAMIOKANDE

by

CHRISTOPHER J. KACHULIS

B.S., Yale University, 2011

Submitted in partial fulfillment of the

requirements for the degree of

Doctor of Philosophy

2018

Approved by

First Reader ____

Edward T. Kearns, Ph.D.
Professor of Physics

Second Reader ____

Christopher P. Grant, Ph.D.
Assistant Professor of Physics

Acknowledgments

The support and guidance of many different people has been instrumental to my successful completion of this thesis, and I am grateful to them all. I would first like to thank my advisor Ed Kearns, whose guidance and mentorship has been truly invaluable. Whether my work was moving along swimmingly, or in a more challenging phase, knowing you would always have my back and nudge me in the right direction if I began to veer off-course made any challenge seem manageable.

At Super-Kamiokande, I would like to particularly thank Roger Wendell for guiding me (and so many others) in my entrance into the collaboration and work with the Super-K atmospheric neutrino oscillation analysis. I would also like to thank Sunichi Mine, Makato Miura, and Yoshinari Hayato for answering my somewhat frequent email questions about the workings of the SK detector and software, Masato Shiozawa and Ed Kearns for their work as conveners of the ATMPD group, and Yoichiro Suzuki (in my early SK years) and Masayuki Nakahata (in my later SK years) for their very successful leadership of the Super-Kamiokande collaboration.

At BU I would like to thank my fellow students and post-docs of the BU neutrino group (present and past), Jeff Gustafson, Flor De Maria Blaszczyk, Dan Gastler, Steve Linden, Sara Sussman, Dan Smith, Silvia Zhang, Zach Collins, and Ryan Linehan for many interesting and entertaining discussions, and always making group meetings something to look forward to. I would like to thank the members of my thesis committee Rob Carey, Chris Grant, Ami Katz, and Alex Sushkov, for their interesting discussions and questions. I would also like to thank the one person I believe should be thanked in every single BU Physics thesis, Mirtha Cabello, for keeping this whole process running as smoothly as possible, and always being the person to go to when we're not sure what we're supposed to do.

Last, but certainly not least, I'd like to thank my family. To my parents Nick and Martha, and my brother Demetri, thank you for you love and support through not just my time in graduate school, but my entire life. And of course I want to thank the one and only Meg Van Wyk. Your love, support, and patience has meant the world to me. I cannot imagine having done this without you.

BOOSTED DARK MATTER AND ATMOSPHERIC NEUTRINO EARTH MATTER EFFECTS AT SUPER-KAMIOKANDE

CHRISTOPHER J. KACHULIS

Boston University Graduate School of Arts and Sciences, 2018

Major Professor: Edward T. Kearns, Professor of Physics

ABSTRACT

This dissertation presents two studies performed with data from Super-Kamiokande, a 50 kT water Cherenkov detector located 1,000 meters below Mt. Ikenoyama in Gifu, Japan, which has been operating since 1996. The first study searches for Earth matter effects in atmospheric neutrino oscillations. Earth matter effects have never before been confirmed in a measurement of atmospheric neutrinos, and observing them is an important step toward measuring the neutrino mass hierarchy, since atmospheric neutrino measurements gain sensitivity to neutrino mass hierarchy through Earth matter effects. We find that our data agrees very well with standard matter effects, and excludes vacuum oscillations at a significance of 1.6σ. The second study searches for boosted dark matter by looking for an excess of elastically scattered electrons above the atmospheric neutrino background, with a visible energy between 100 MeV and 1 TeV, pointing back to the Galactic Center or the Sun. No such excess is observed. Limits on boosted dark matter event rates in multiple angular cones around the Galactic Center and Sun are calculated. These limits can constrain general boosted dark matter theories, as is demonstrated by calculating limits for a baseline model of boosted dark matter produced from cold dark matter annihilation or decay.

Contents

List of Tables

List of Figures

List of Abbreviations

ADC . . . . Analog to Digital Converter

AFS . . . . Away from Source

AFT . . . . After trigger (one of the SK triggers)

ATLAS . . . . A Toroidal LHC ApparatuS

ATM . . . . Analog Timing Module

CC . . . . Charged Current

CC1π . . . . Charged Current Single Pion

CCDIS . . . . Charged Current Deep Inelastic Scattering

CCQE . . . . Charged Current Quasielastic

CMB . . . . Cosmic Microwave Background

CνB . . . . Cosmic Neutrino Background

CP . . . . Charge Parity

DAQ . . . . Data Acquisition System

ESO . . . . European Southern Observatory

FC . . . . Fully Contained

FCFV . . . . Fully Contained Fiducial Volume

FRP . . . . Fiber-Reinforced Plastic

FV . . . . Fiducial Volume

FWHM . . . . Full Width Half Maximum

GC . . . . Galactic Center

HE . . . . High Energy (one of the SK triggers)

HV . . . . High Voltage

ID . . . . Inner Detector

IMB . . . . Irvine-Michigan-Brookhaven

K2K ... KEK to Kamioka KamLAND ... Kamioka Liquid Scintillator Antineutrino Detector

KEK ...... Ko Enerugi Kasokuki Kenkyu Kiko (High Energy Accelerator Research Organization)

LBL .... Long Baseline

λCDM .... λ-Cold Dark Matter

LE .... Low Energy (one of the SK triggers)

MACHO .... Massive Compact Halo Object

MC .... Monte Carlo

MINOS .... Main Injector Neutrino Oscillation Search

NC .... Neutral Current

NFW .... Navarro-Frenk-White

NOνA .... NuMI Off-Axis ν_e Appearance

OD .... Outer Detector

OGLE .... Optical Gravitational Lensing Experiment

PC .... Partially Contained PID .... Particle Identification PMNS Pontecorvo-Maki-Nakagawa-Sakata

PMT .... Photomultiplier Tube

PREM .... Preliminary Reference Earth Model

QAC .... Charge to Analog Converter

QBEE .... QTC Based Electronics with Ethernet

QCD .... Quantum Chromodynamics

QTC .... Charge to Time Converter

RENO .... Reactor Experiment for Neutrino Oscillation

RMS .... Root Mean Square

SHE .... Special High Energy (one of the SK triggers)

SLE .... Super Low Energy (one of the SK triggers)

T2K .... Tokai to Kamioka

TAC .... Time to Analog Converter

UPMU .... Upward Going Muon

WIMP .... Weakly Interacting Massive Particle

Chapter 1

Introduction

This thesis, at a most basic level, concerns two strange ideas from the early 1930's. While both neutrinos and dark matter have been around for ∼13.8 billion years [1, 2], and have coexisted with humans for a slightly shorter but still respectable ∼200,000 years, their existence has only been known to us for the relatively short period of about 90 years. The neutrino was first proposed by Wolfgang Pauli in a letter to a meeting in Tubingen, Germany, in 1930, as a possible explanation for the observed continuous beta decay spectrum [3]. In this letter Pauli wrote:

> ...there could exist in the nuclei electrically neutral particles that I wish to call neutrons, which have spin 1/2 and obey the exclusion principle, and additionally differ from light quanta in that they do not travel with the velocity of light. The mass of the neutron must be of the same order of magnitude as the electron mass and, in any case, not larger than 0.01 proton mass.–The continuous β-spectrum would then become understandable by the assumption that in β decay a neutron is emitted together with the electron, in such a way that the sum of the energies of neutron and electron is constant. [3]

This first proposal was tentative, and it is interesting to note that Pauli first used the name "neutron." The particle we know today as the neutron would not be discovered by James Chadwick for another two years, at which point the light neutral particle proposed by Pauli was renamed the "neutrino" by Enrico Fermi. In 1934, Fermi published a quantitative theory of β-decay which included neutrinos as an assumed component [4], and predicted the continuous beta-decay spectrum.

Just a few years after Pauli proposed the neutrino, Fritz Zwicky proposed the existence of dark matter to explain the velocity dispersion of eight nebulae in the Coma Cluster. In discussing the dispersion of the velocities of these eight nebulae, which was far larger than expected based on the light observed from them, Zwicky wrote:

> If this would be confirmed we would get the surprising result that dark matter is present in much greater amount than luminous matter. [5]

The similarities between neutrinos and dark matter are not confined to the decade of their proposals; both have mass, and importantly, neither interacts electromagnetically. In fact, these similarities have led to the idea that dark matter could in fact be a type of neutrino. While there has been no experimental verification of this even after significant searching, it does remain a viable possibility.

However, this is where the historical stories of neutrinos and dark matter diverge. After its proposal by Pauli, continued measurements of the beta-decay spectrum and observations of new meson decays using nuclear track emulsion strengthened the evidence for the existence of the neutrino. Then in the early 1950's, the neutrino was for the first time explicitly observed. Fred Reines and Clyde Cowan placed a large liquid scintillator detector near a nuclear reactor in Hanford, Washington. They hoped to observe neutrinos produced by the reactor interacting with the protons in the liquid scintillator through inverse beta decay:

$$\bar{\nu} + p \rightarrow n + e^{+}. \tag{1.1}$$

They searched for this process using Cadmium loaded liquid scintillator. Coincidence between scintillation light due to the positron and the γ produced by the capture of the neutron on Cadmium indicated an inverse beta decay event. They noted a change in the measured event rate when the reactor was on versus when it was off, which agreed well with the predicted neutrino event rate [6]. They soon confirmed the result with an upgraded experiment at Savanah River [7, 8].

The story for dark matter is quite different. While there have been additional observations of the gravitational effects of dark matter since it was first proposed by Zwicky, there has been no explicit observation of a dark matter particle to mirror Reines and Cowan's observation of the neutrino (and not for lack of trying). Indeed, as the reader will become aware by comparing Chapter 5 and Chapter 6, significantly more is currently known about the nature of neutrinos than about the nature of dark matter. In fact, the vast majority of what we know about dark matter consists of being able to say what it isn't.

In this thesis, I will attempt to add a little bit more to each of these stories. I will present an observation of hints of Earth matter effects in atmospheric neutrino oscillations, in agreement with theoretical expectations. I will also present a search for a relatively newly proposed type of dark matter called "boosted" dark matter, for which no evidence was found. In the end, this thesis will give us a little bit more confidence in our theories about the nature of neutrinos, and add one more entry to the list of things dark matter appears not to be. To whoever reads the most of it, I hope you find it enjoyable.

Chapter 2

The Super-Kamiokande Detector

The Super Kamiokande detector was originally built int the 1990's to search for nucleon decay and study the nature of neutrinos. In this chapter an overview of the detector apparatus, detection principle, and detector calibration techniques are presented. Detailed overviews of the detector and detector calibration techniques can also be found in [9] and [10].

2.1 Overview

The SK detector is a large water Cherenkov detector located in the Mozumi mine below Mt. Ikenoyama in Gifu, Japan, with a mean overburden of 1000 m of rock (2700 m water-equivalent.). This overburden removes cosmic ray muons with energies less than 1.3 TeV. The detector consists of a 50 kT cylindrical tank of water, which is divided into a 32 kT inner detector (ID) surrounded by an 18 kT outer detector (OD). The ID and the OD are optically separated by black Tyvek sheeting, and both are instrumented with photomultiplier tubes (PMTs) to observe Cherenkov radiation. Its large fiducial volume and high quality reconstruction capabilities make SK an extremely effective detector for nucleon decay searches and studies of neutrinos over a wide range of energies.

The detector's data taking time, which began with its commissioning in April 1996, is divided into four phases. The first phase, known as "SK-I", acquired 1489.2 days of data, running from commissioning until July 2001, when the detector was shut down for maintenance and upgrades. During the refilling of the tank in November 2001, an accident destroyed over half of the PMTs in the detector. The remaining PMTs were fitted with protective cases to avoid a future accident and redistributed, and the second phase, known as "SK-II", ran from October 2002 until October 2005 with half the ID PMT coverage of SK-I [1]. SK-II acquired 798.6 livetime days of data. During the shutdown after SK-II, new ID PMTs were added, and data taking resumed in July 2006 with the ID PMT coverage back at SK-I levels. This third phase is known as "SK-III", and acquired 518.1 livetime days of data, running until September 2008, when the experiment was briefly shutdown for an electronics upgrade. Upon restarting in September 2008, SK entered its fourth phase, known as "SK-IV", which is ongoing as of the writing of this thesis, and which has acquired 2867.2 livetime days of data as of May 2017. In total, SK has recorded 5673.1 livetime days of data (as of May 2017) with just over half of that data coming during SK-IV.

2.2 Detector Structure

The main component of the SK detector is a cylindrical stainless steel tank, with a diameter of 39 m and a height of 42 m, which is filled with about 50 kts of water. The structure of the detector is shown in Fig. 2.1. The tank is segmented into an inner detector (ID), with a diameter of 33.8 m and a height of 36.2 m, which hold 32

[1] OD PMT coverage was fully restored for SK-II

kts of water, and an outer detector (OD) which is the region of the tank outside the ID. The ID is the primary detector used for most physics analyses, while the OD is primarily used as an active cosmic ray veto. The ID and OD are separated from one another by a cylindrical PMT support structure. On the inner surface of the support structure, 11,146 inward-facing 20 inch PMTs, giving a coverage of about 40%, are mounted to observe activity in the ID (for SK-II half as many PMTs were used in the ID). The outer surface of the support structure is instrumented with 1885 outward-facing 8 inch PMTs to observe the OD. Lightproof Tyvek sheeting on both surfaces of the PMT structure optically separates the ID from the OD. It also results in a 55 cm dead space between the ID and the OD, from which light cannot escape. The Tyvek sheeting is black on the side facing into the ID, in order to reduce reflections which would diminish reconstruction accuracy. On the side facing the OD, conversely, the Tyvek sheeting is white, in order to increase reflections. This is done to improve light collection efficiency in the OD, to compensate for its lower PMT coverage. Scattered light in the OD is also much less problematic for physics goals compared to scattered light in the ID.

Since the performance of the PMTs is sensitive to magnetic fields, the roughly 450 mG geomagnetic field at the SK detector must be offset. Therefore, 26 sets of horizontal and verticle Helmholtz coils are arranged around the inner surface of the tank. These reduce the magnetic field in the tank to about 50 mG, which results in an estimated 1-2% effect on the collection efficiency of the ID PMTs.

2.3 Cherenkov Radiation

When a charged particle travels through a material at a speed faster than the phase velocity of light in that material, Cherenkov radiation is produced. Molecules

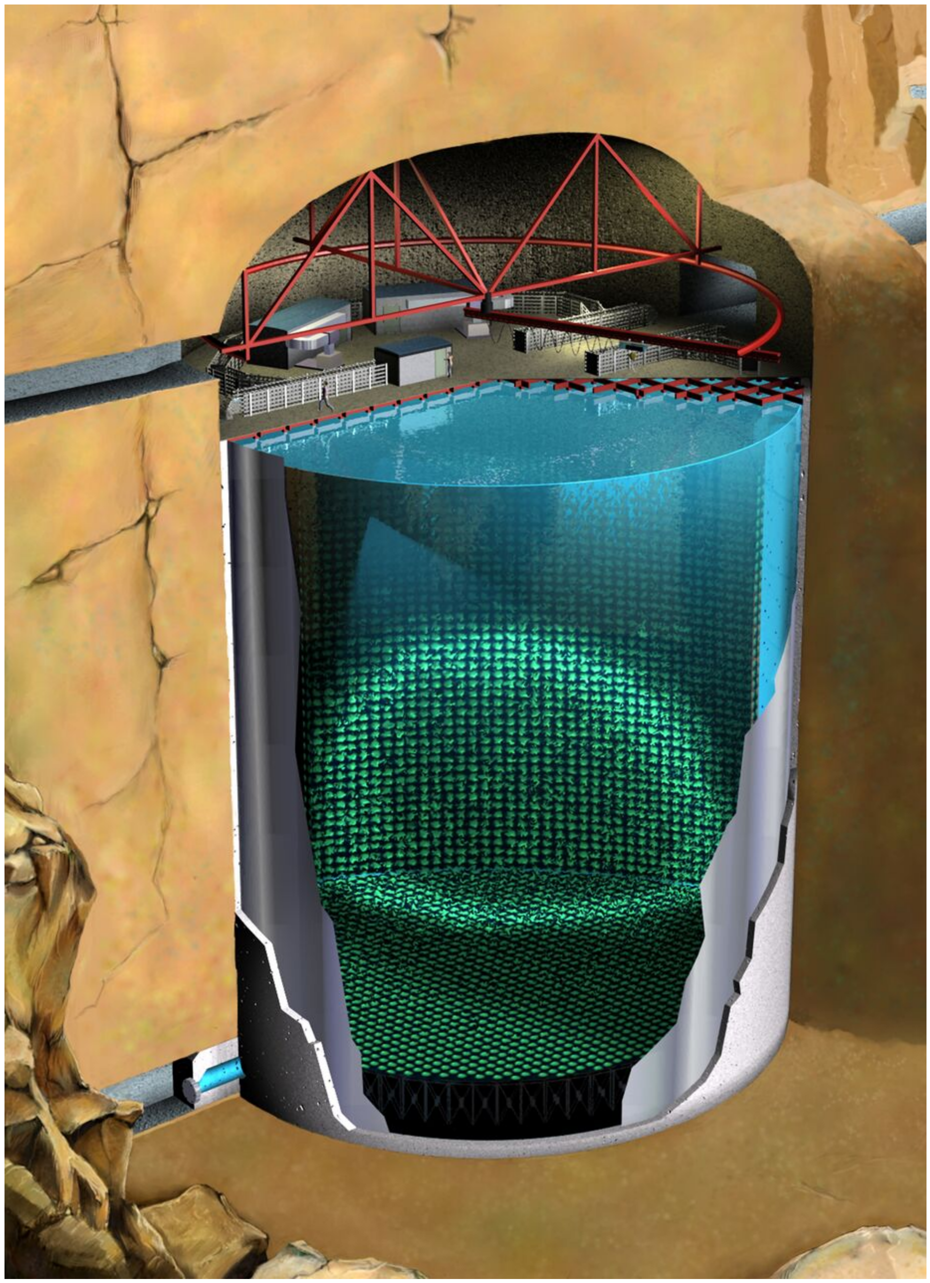

Figure 2.1: Structure of the SK detector. [11]

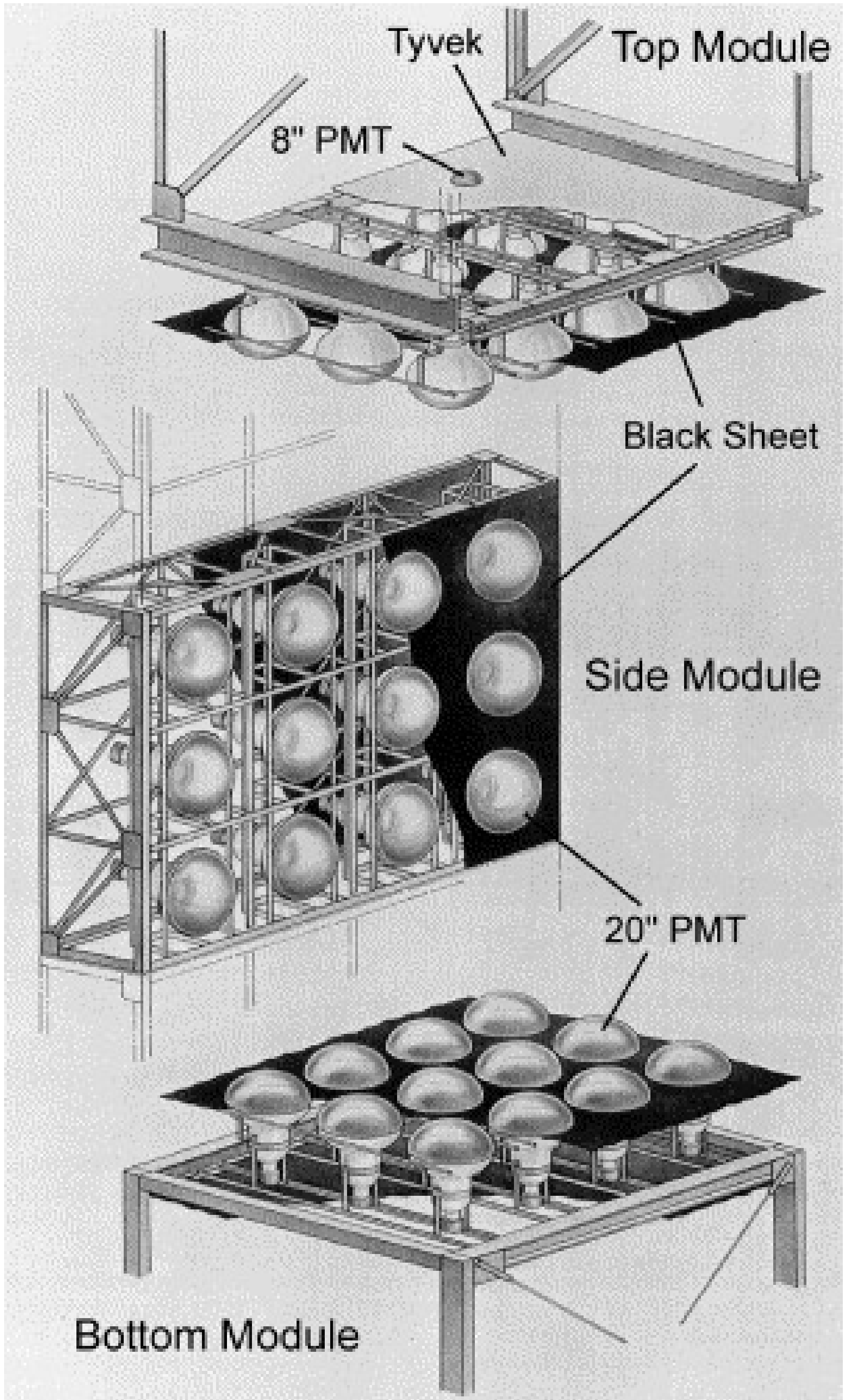

Figure 2.2: PMT support structure. [9]

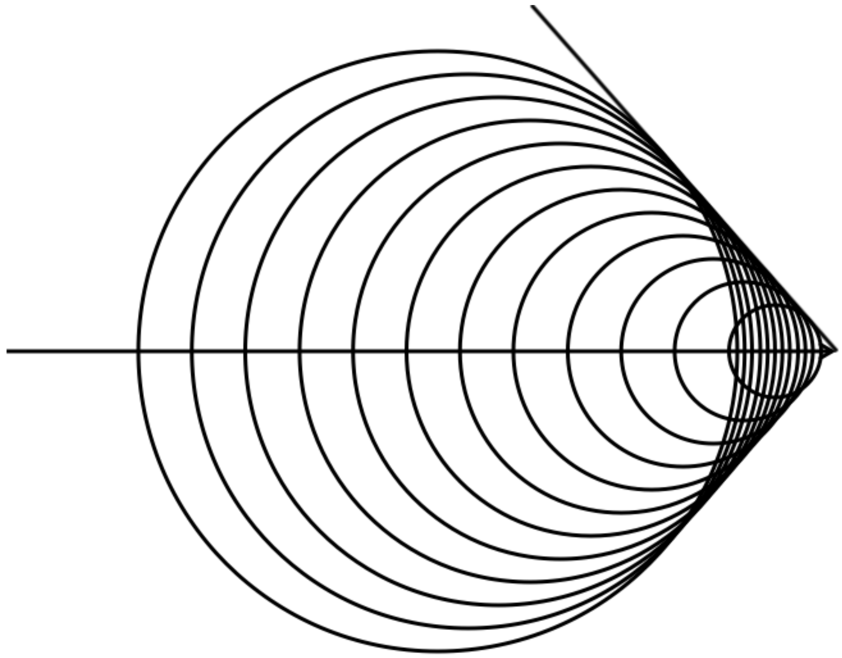

Figure 2.3: Constructive interference resulting in Cherenkov radiation.

excited by the passing particle release light. When the particle is traveling faster than c/n, the light emitted from different points along the particles path interferes constructively to create Cherenkov radiation, as shown in Fig. 2.3. The requirement for Cherenkov radiation is thus

$$\beta > \frac{1}{n}. \tag{2.1}$$

The Cherenkov radiation is emitted from the path of the charged particle along a cone centered on the path with half opening angle θ_C given by:

$$\cos\theta_C = \frac{1}{\beta n}. \tag{2.2}$$

A detailed derivation of these formula based on electrodynamics can be found in [12].

The index of refraction of water is 1.33, so for charged particles in water the Cherenkov threshold corresponds to $\beta > 0.75$. This can be translated to a momentum threshold of 577 KeV/c for electrons, 119 MeV/c for muons, 157 MeV/c for charged pions, and 1.058 GeV/c for protons. The Cherenkov angle for a highly relativistic charge particle in water ($\gamma \gg 1$) is about 42°.

The emitted Cherenkov spectrum is described by the formula[13]:

$$\frac{d^2N}{d\lambda dx} = \frac{2\pi\alpha z^2}{\lambda^2}\left(1 - \frac{1}{\beta^2 n^2(\lambda)}\right) \tag{2.3}$$

where α is the fine structure constant, z is the charge of the particle (in units of electron charge), λ is the wavelength of the emitted light, and x is the distance traveled by the charged particle. It should be noted that while this formula allows for a wavelength dependent index of refraction, the index of refraction of water only changes by a few percent in the range of wavelengths observed by the PMTs.

In SK, Cherenkov radiation is observed as rings (for particles which stop) or filled in circles (for particles which penetrate to the OD) of hit PMTs, as shown in Fig. 2.4. The timing of hits can be used to reconstruct the position of the interaction, and the orientation of the ring indicates the direction of travel of the charged particle. Further, as can be seen from Eq. (2.3), the number of Cherenkov photons produced is a linear function of path length for highly relativistic particles. Since the path length (or sum of path length in a shower, in the case of an electron) is directly related to the energy of the charged particle, the amount of Cherenkov light can be used to reconstruct charge particle energy.

2.4 Photomultiplier Tubes

The ID PMTs are 20-inch PMTs (Hamamatsu R3600) built by Hamamatsu Photonics K.K. A schematic is shown in Fig. 2.5. These PMTs were based off an earlier

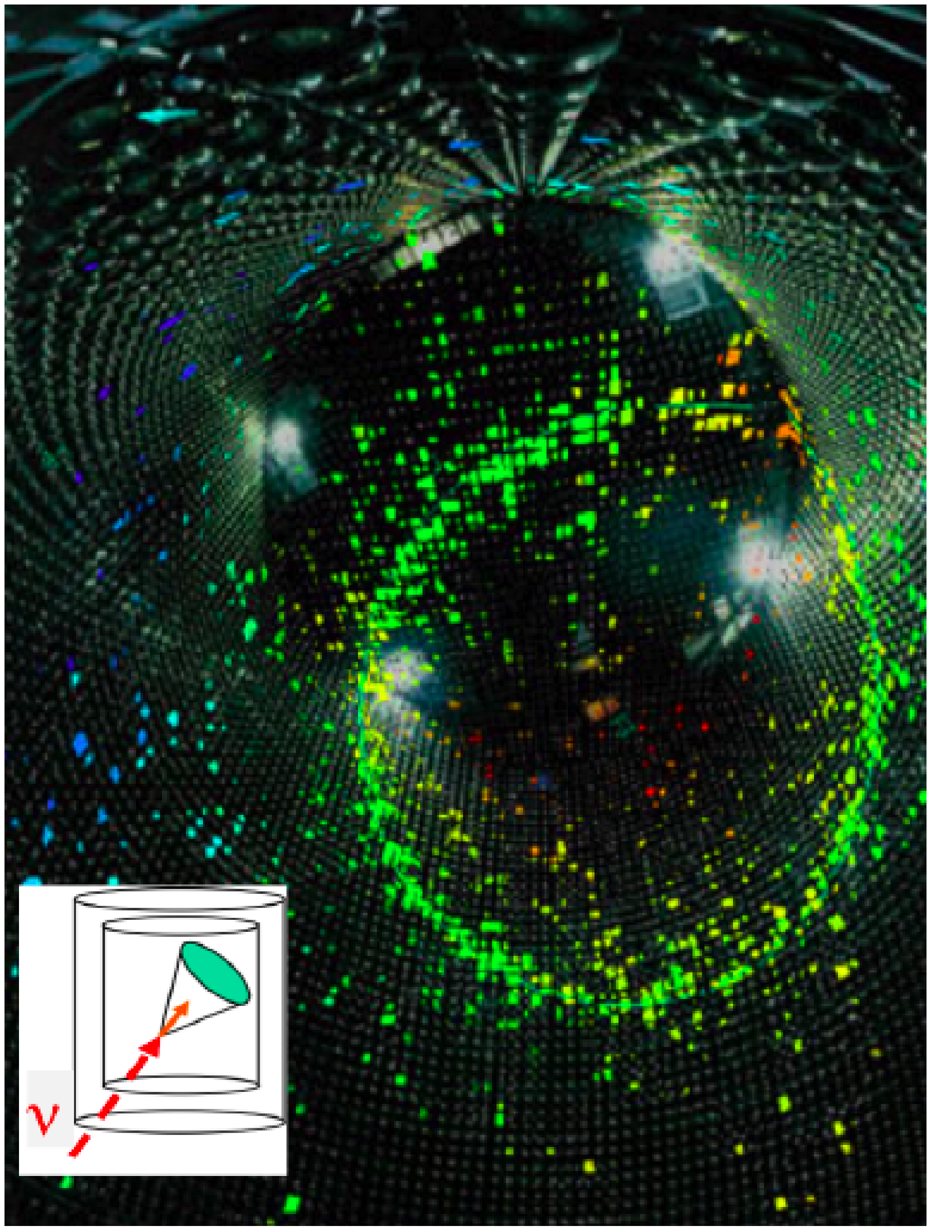

Figure 2.4: Visualization of a Cherenkov ring in SK. The inset shows a neutrino entering the detector, interacting in the inner detector, and the Cherenkov cone from the resulting relativistic charged particle. [14]

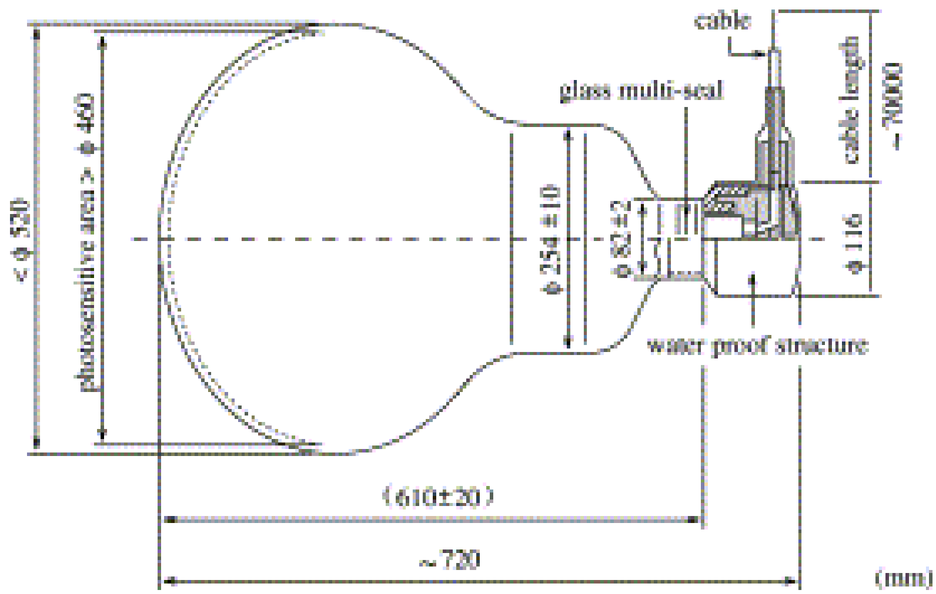

Figure 2.5: Schematic of the ID PMTs. [9]

Hamamtsu designed 20-inch PMT (Hamamatsu R1449) which had been used in the Kamiokande Detector. The photocathode is made of bialkali, which was chosen for its high sensitivity to blue light and low thermionic emission. The quantum efficiency of the photocathode peaks around 21% between 360 and 400 nm, and is shown as a function of wavelength along with the emitted spectrum of Cherenkov light in water in Fig. 2.6. The dynode structure is a venitian blind type, which was optimized to improve photoelectron (p.e.) timing resolution and collection efficiency [15]. The single p.e. pulse height distribution and transit time distribution are shown in Fig. 2.7.

In order to prevent another accident like the one which occurred during refilling prior to SK-II, all PMTs have been enclosed in a protective case since the beginning of SK-II. These protective cases consist of an acrylic dome over the face of the PMT, and a fiber-reinforced plastic (FRP) case around the sides and back of the PMT. The FRP case has holes in it that allow water to flow freely around the PMT, but also restrict the speed with which water can rush into the vacuum of a PMT in case of a PMT implosion. This mitigates the creation of a shock wave, which was determined

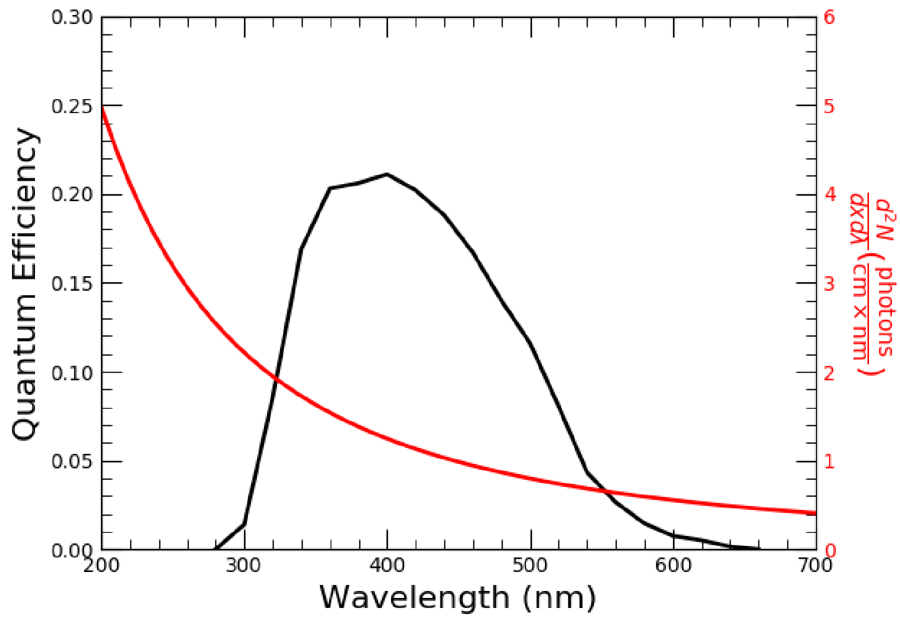

Figure 2.6: Photocathode quantum efficiency in black and emitted Cherenkov spectrum in red. Note different y-axes.

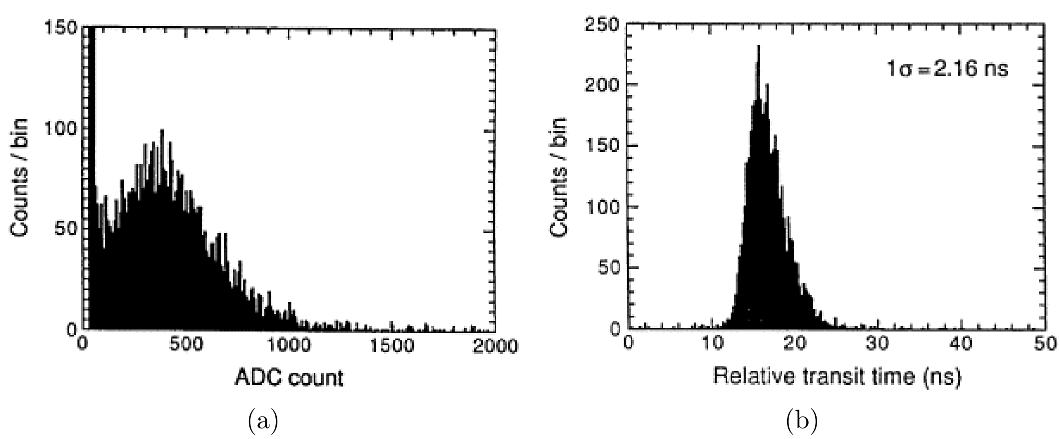

Figure 2.7: Left: ID PMT single p.e. pulse height distribution. The peak near zero ADC counts is the result of dark current. Right: ID PMT relative transit time distribution at 410 nm and single p.e. level. Both from [9]

to be the cause of the original accident.

The OD PMTs are 8-inch PMTs, also produced by Hamamatsu. Five-hundred ninety-one are old Hamamatsu R1408 PMTs, recycled from the IMB experiment, and 1293 are new Hamamatsu R5912 PMTs, installed during the upgrades between SK-I and SK-II, and SK-II and SK-III.

2.5 Electronics and Data Acquisition

The SK Electronics and Data Acquisition System (DAQ) was extensively upgraded between SK-III and SK-IV. As such, the SK-IV electronics will be explained separately from the SK I-III electronics.

2.5.1 SK I-III

The SK I-III DAQ processed ID PMT signals using custom build Analog-Timing-Modules (ATMs), which were originally designed and built by KEK. The PMT signal was split into four separate signals. One of these signals was sent to a discriminator, which compared the signal to a threshold corresponding to 1/4 photoelectron equivalent. When the signal crossed this threshold, a 200 ns wide logic pulse was sent to a hardware trigger module. Simultaneously, the signal from the PMT was stored by a Charge-to-Analog Converter (QAC), and an integration of a constant current was started by a Time-to-Analog Converter (TAC). When a global trigger was received from the hardware trigger module, the TAC integration was stopped and the information in the QAC and TAC were sent to and Analog-to-Digital Converter (ADC) to be digitized and stored in internal memory. Because the TAC integrated a constant charge from the time of the channel trigger to the time of the global trigger, the time of the PMT signal relative to the global trigger can be calculated from the total integrated charge on the TAC. Each channel was assigned two TACs and QACs, in order to process events which might occur in rapid succession, such as a decay electron following a muon. The charge dynamic range of the ATM was about 450 pC, with a resolution of 0.2 pC, while the timing dynamic range was 1.3 μs, with a resolution of 0.4 ns.

A hitsum was calculated by the hardware trigger module by simple analog sum of the logic signals from the ATMs. When the hitsum crossed a given threshold, a global trigger would be issued to the ATMs. Three different triggers were used: high energy (HE), low energy (LE) and super low energy (SLE). The HE and LE triggers were set at 31 and 29 hits, respectively, with the LE threshold corresponding to an electron energy of 5.7 MeV. The SLE trigger was added to lower the energy threshold to 4.6 MeV. The OD operated with a similar trigger system, and OD triggers were issued with a threshold of 19 hits. Additional details of the ID and OD electronics and DAQ for SK I-III can be found in [9].

2.5.2 SK-IV

The SK electronics were upgraded between SK-III and SK-IV [16, 17]. The ATM was replaced by a front end electronics board called a QBEE, which stands for "QTC (Charge-to-Time Converter) Based Electronics with Ethernet." A QBEE is shown in Fig. 2.8. PMT signals are processed by a QTC, which encodes the time and charge of the PMT pulse into the timing of a single pulse, as shown in Fig. 2.9. When the PMT signal crosses a threshold which corresponds to about 1/4 pe (the same as in SK I-III), the QTC begins an output pulse, and a capacitor charges up over 400 ns with the charge from the PMT pulse. The capacitor is then discharged at a constant rate, and the QTC output pulse is stopped when the capacitor charge drops below a comparator level. The QTC output pulse thus encodes the time of the PMT pulse as the time of its leading edge, and the charge of the PMT pulse as its width. This full encoding and processing results in a deadtime of 900 ns.

Each PMT signal is processed by a QTC under three different gain settings, with gain ratios 1:$\frac{1}{7}$:$\frac{1}{49}$. The charge dynamic ranges of the three gain setting are shown in Table 2.1. While each PMT signal is process under all three gain settings, only the result from the lowest gain setting which is not saturated is used. This results in a charge resolution similar to the ATMs used in SK I-III, but with about five times the dynamic range.

The hardware trigger used in SK I-III is replaced by a software trigger for SK-IV. Every hit recorded by the QBEEs is sent to Front-End PCs, with each Front-End PC receiving the hits from 30 QBEEs. The data from the Front-End PCs is then sent on to Merger PCs, which combine the hits from all PMTs and apply software triggers to search for physics events. When a software trigger is generated, the event data is sent to an Organizer PC, which writes the data onto disk for offline analysis. This data flow is visualized in Fig. 2.10.

The software trigger of SK-IV has multiple advantages over the hardware trigger of SK-III. Primarily, it allows for any length of event, more complex trigger logic, and introduction of new triggers. The main triggers used in SK-IV are summarized in Table 2.2. While the SLE, HE, SHE, and OD triggers perform functions achievable with the SK I-III hardware trigger, the AFT trigger shows the true power of moving to a software trigger for SK-IV. The AFT trigger is used for tagging neutrons, which capture on Hydrogen and produce a 2.2 MeV γ a few hundered μs after a primary neutrino event. They do not produce enough hits to generate an SK I-III hitsum trigger, and lowering the hitsum threshold to catch such events would significantly increase the data rate and require substantially more computing power and disk space

Gain Setting	Dynamic Range	Resolution
Low	51 pC	0.1 pC
Medium	357 pC	0.7 pC
High	2500 pC	4.9 pC

Table 2.1: Charge dynamic ranges for the three gain settings of the SK-IV QTC.

to handle. This means that neutron tagging is impossible in SK I-III. The software trigger of SK-IV solves all of these problems with the AFT trigger, which takes advantage of both the complex trigger logic and variable event width available in the software trigger system.

SK-IV Triggers	Trigger Logic	Event Width (μs)
SLE	34 (31) hits in 200 ns	-0.5$\rightarrow$ 1.0
HE	50 hits in 200 ns	-5$\rightarrow$ 35
SHE	70 (58) hits in 200 ns	-5$\rightarrow$ 35
OD	22 hits in 200 ns (in OD)	
AFT	SHE, no OD	35 $\rightarrow$ 535

Table 2.2: Trigger information for SK-IV. The abbreviations are as follows: OD (outer detector), SLE (super low energy), HE (high energy), SHE (special high energy) and AFT (after). The SLE and SHE trigger thresholds were lowered from 34 to 31 and 70 to 58 hits respectively, during SK-IV running. There are $\sim$9 hits of dark noise in 200 ns and $\sim$6 hits corresponds to 1 MeV electron equivalent energy.

2.6 Water System

Keeping the SK water as transparent and stable as possible is extremely important for physics analyses. To this end, a water purification system is used to continuously reprocess the water in the SK tank, at a rate of about 60 tons/h. This system is described extensively in [9]. The system takes in water from the SK Tank, a UV sterilizer kills any bacteria in the water, multiple filters reduce the concentration of particles larger than 0.2 μm to 6 particles/cc, and a vacuum degasifier and mem-

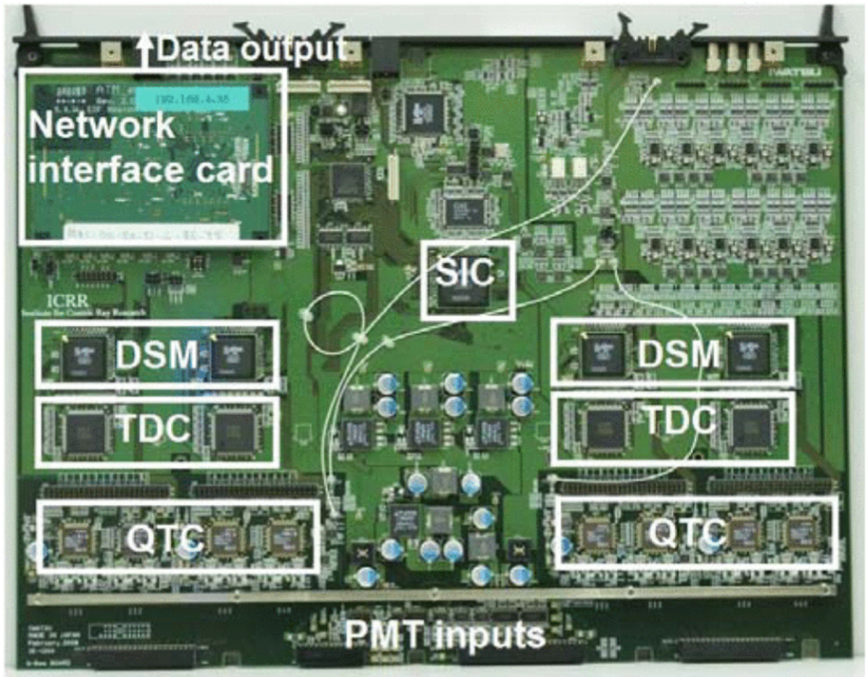

Figure 2.8: Front end electronics used in SK-IV, called QBEE [16]

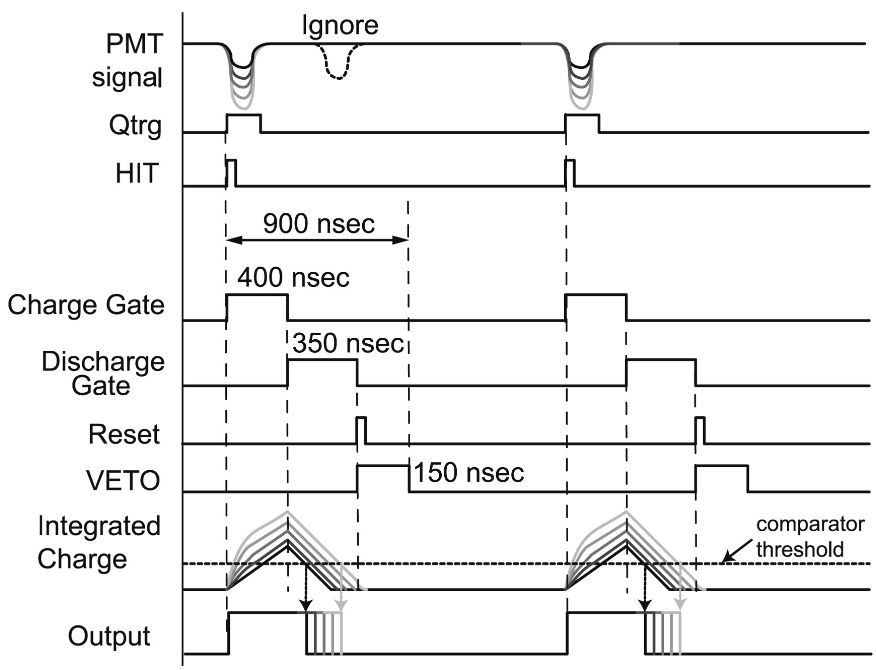

Figure 2.9: QTC charge and time encoding for QBEE [17].

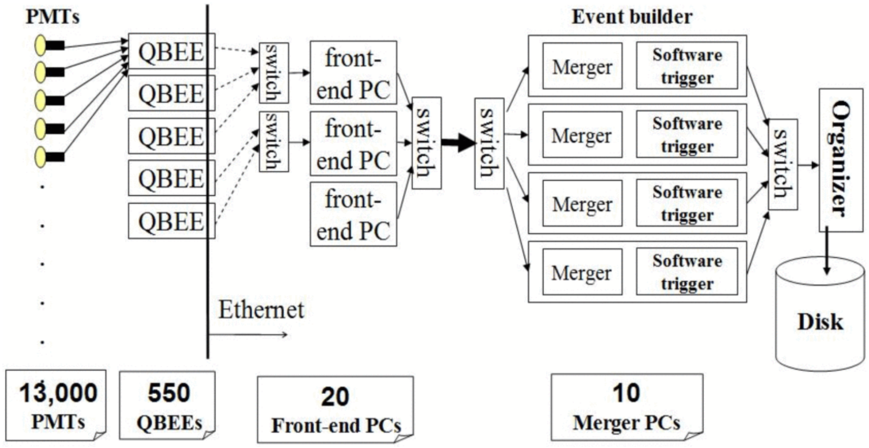

Figure 2.10: SK-IV data flow [16]

brane degasifier together reduce the concentration of radon in the water to about 0.4 mBq/m^3, before the water is returned to the tank. A heat exchanger maintains the water at a temperature of about 13°C.

Because the air in the mine has a naturally high radon concentration (ranging from a few hundred to a few thousand Bq/m^3, depending on the season), the gap between the top surface of the water and the top of the tank is filled with radon-reduced air at a slight overpressure. This radon-reduced air is processed by an air purification system which outputs air with a radon concentration of a few mBq/m^3. The radon concentration of the air in the dome above the SK cavity is maintained at around 40 Bq/m^3 by pumping air from outside the mine into the dome, and the walls of the dome are additionally coated with a radon tight plastic material from Mineguard.

2.7 Detector Calibration

Calibration enables the translation of the response of the detector into actual physical properties of the observed process. The response of the SK detector to a particular physics process is essentially the combination of three responses:

- The physics of the initial process and production of photons through Cherenkov radiation
- The propagation of photons through the water to the PMTs (water transparency)
- The response of the PMTs and electronics to the incident photons

Since the first response is what we are actually interested in observing, calibration is necessary to understand the second and third responses, so that we can translate the full detector response into an understanding of the actual physics process being observed. In this section, I will discuss the main components of detector calibration. A detailed description can be found in [10].

2.7.1 Water Transparency

The propagation of photons through water is described by the equation:

$$I(l, \lambda) = I_0(\lambda) e^{\frac{l}{L(\lambda)}} \tag{2.4}$$

where $I(l, \lambda)$ is the intensity of light of wavelength λ a distance l from the source, $I_0(\lambda)$ is the initial intensity of the light, and $L(\lambda)$ is the total attenuation length at the given wavelength, which includes both scattering and absorption. The attenuation length can be broken into three components:

$$L(\lambda) = \frac{1}{\alpha_{abs}(\lambda) + \alpha_{sym}(\lambda) + \alpha_{asy}(\lambda)}. \tag{2.5}$$

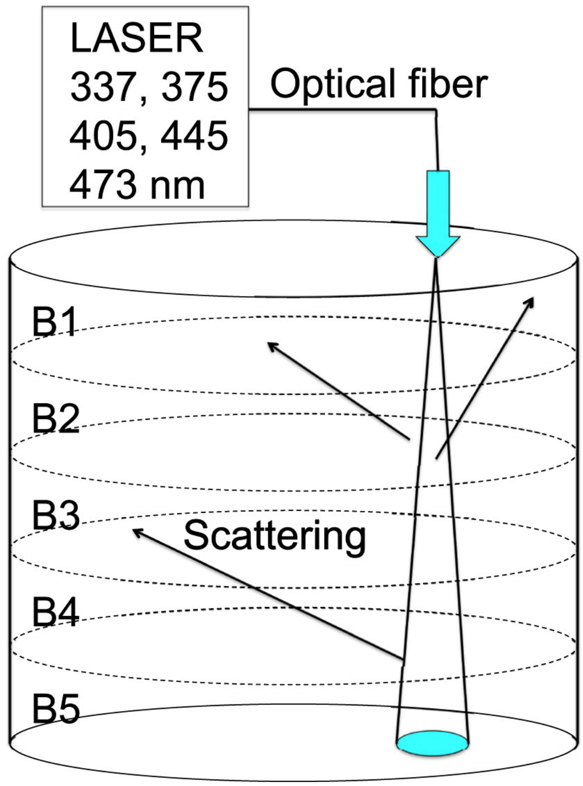

Figure 2.11: Laser setup for water transparency measurement [10].

Here $\alpha_{abs}(\lambda)$ is the absorption amplitude, $\alpha_{sym}(\lambda)$ is the "symmetric" scattering amplitude, which is composed of Rayleigh scattering and symmetric Mie scattering, and $\alpha_{asy}(\lambda)$ is the "asymmetric" scattering amplitude, which is composed of forward Mie scattering. In order to measure these amplitudes, a collimated laser beam is injected at a few different wavelengths downward into the SK detector, as shown in Fig. 2.11. The detector is divided into seven regions, (top, bottom, five barrel regions), and the absorption and scattering amplitudes are tuned in MC so that the distribution of hits as a function a time in MC agrees with what is seen in data. The results at the different wavelengths are used to fit the amplitudes as a function of wavelength to predetermined polynomial forms. The results of these fits from a typical calibration run are shown in Fig. 2.12.

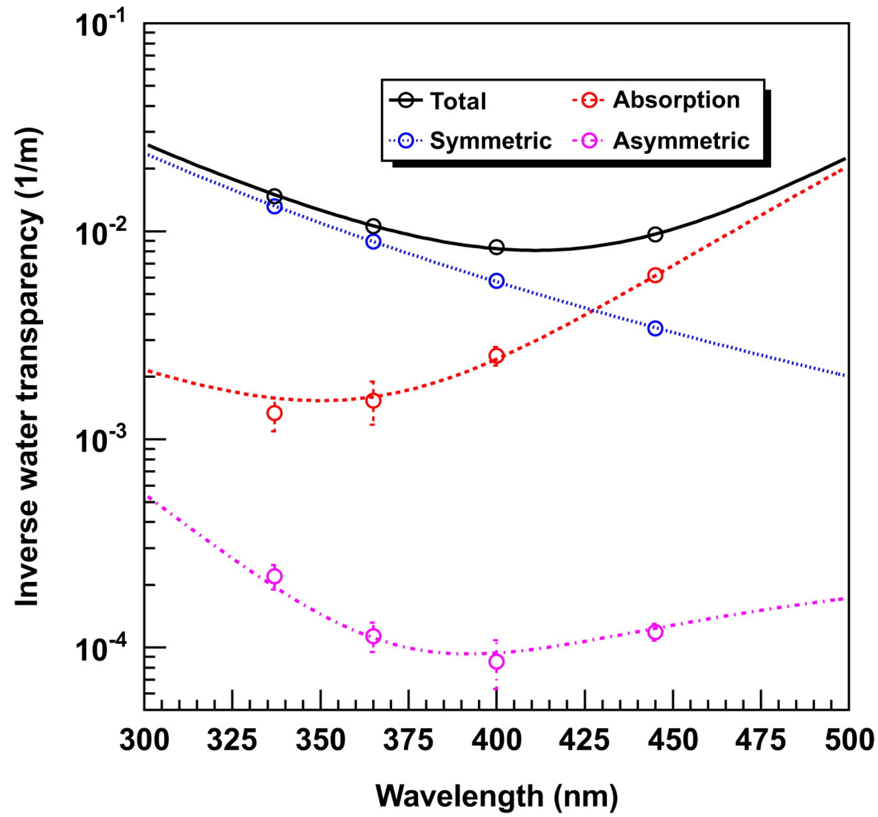

Figure 2.12: Absorption amplitude results from a typical laser calibration run [10].

2.7.2 PMT and Electronics Response

When light hits a PMT, a current pulse is produced by the PMT. The information recorded by the SK electronics is the charge of the pulse, and the time the rising edge of the pulse crossed a discriminator threshold. In order to correctly simulate how the number of photons at a particular time will be translated into an electronics response, calibration of the PMTs and SK electronics is required.

2.7.3 Charge Response

First, the high voltage (HV) for each PMT was set so that each PMT would produce the same amount of charge from the same intensity of light. To do this, 420

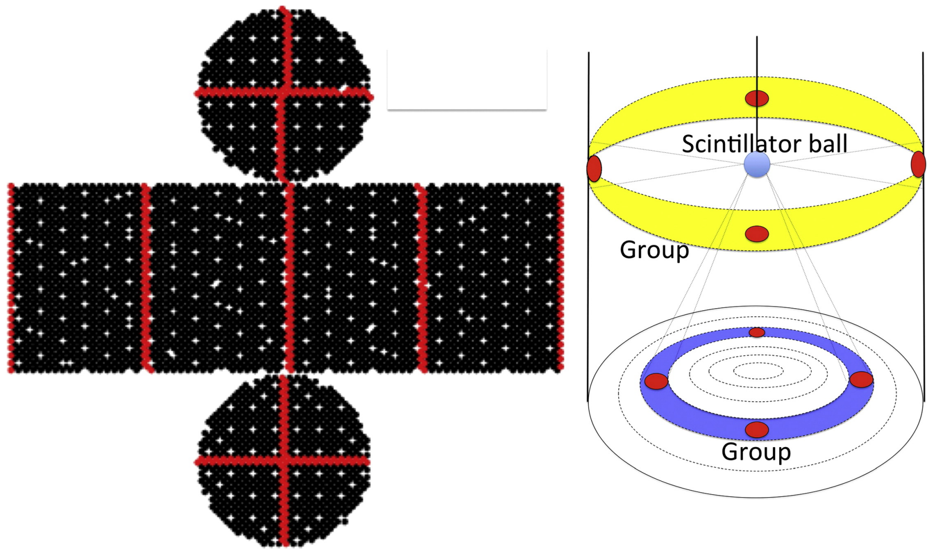

Figure 2.13: Location of the 420 reference PMTs used for HV calibration [10].

"reference" PMTs were calibrated in a dedicated pre-calibration system before their installation, so that their desired HV settings were known [10]. These 420 PMTs were then arranged in the detector in order to take advantage of the cylindrical symmetry of the detector, as shown in Fig. 2.13. For a light source on the central axis of the detector, the intensity of light at any PMT could be estimated by the response of the reference PMTs with the same geometric relationship to the light source. A Xe-lamp fed into a scintillator ball producing isotropic light was used as the light source in both the pre-calibration of the 420 reference PMTs and in the calibration of all the PMTs in the tank.

Once the HV setting for each PMT has been assigned, the expected charge from incident light of intensity I on the i^{th} PMT can be written as:

$$Q_i = I \times QE_i \times G_i \tag{2.6}$$

where QE_i and G_i are the quantum efficiency and gain of the i^{th} PMT. Simulation of PMT response thus require the measurement of quantum efficiency and gain for each

PMT.

Gain calibration is performed first, and is done in two steps. In the first step, the relative gain of each PMT compared to the average over the whole detector is calculated. Then the absolute gain of the full detector is found. Between these two measurements, the absolute gain of each individual PMT can be found.

The relative gain measurement is performed as follows. A stable light source which emits constant amplitude flashes is placed in the detector and run in two different modes. In the first mode, the source produces high-intensity flashes, so that each PMT observes a reasonable number of photons. In this mode, the average charge observed by PMT i can be written as

$$Q_{obs}(i) \propto I_{high} \times a_i \times QE_i \times G_i \tag{2.7}$$

where I_{high} is the intensity of the light source in the high-intensity setting and a_i is the acceptance of the i^{th} PMT, which accounts for water transparency and geometrical affects. In the second mode, the light source produces low-intensity flashes, so that hits on PMTs can be assumed to be only single photo-electrons (pe's). In this mode, the number of hits when the charge crosses a threshold value can be written as

$$N_{obs}(i) \propto I_{low} \times a_i \times QE_i. \tag{2.8}$$

Note that in this mode, the number of hits is mostly independent of gain. In this way, the relative gain for each PMT can be extracted as

$$G_i \propto \frac{Q_{obs}(i)}{N_{obs}(i)} \tag{2.9}$$

where the proportionality constant is the same for all PMTs.

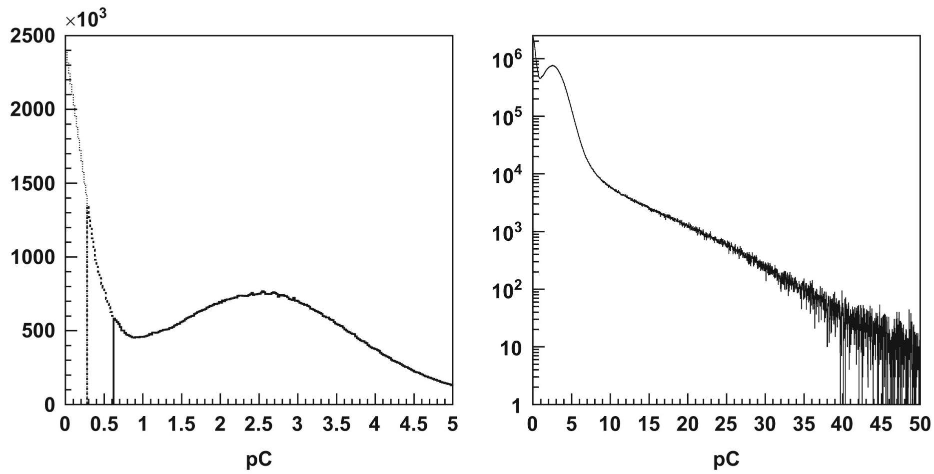

Figure 2.14: Single pe distribution as measured during SK-III. The figure on the right shows the same data as on the left, just with a log scale [10].

With the relative gains of each PMT known, a nickel source which produces gamma-rays isotropically is placed in the detector. This source produces γ rays with energies around 9 MeV from neutron capture on ^{58}Ni. The neutrons are provided by a ^{252}Cf source. The nickel source is faint enough that over 99% of observed PMT hits come from single pe. The charge of the resulting pulses are corrected by the relative gains for each PMT, and the single p.e. distribution of the entire detector is thus found. This distribution as measured during SK-III is shown in Fig. 2.14.

The quantum efficiency of each PMT was found by comparing the number of single-pe hits in a nickel source run to that expected by MC simulation. The QE in the MC was adjusted until the simulation matched the data well.

The response of the PMTs and electronics was also tested by injecting laser light at 30 different intensities into the ID. This response is shown in Fig. 2.15, and is used in MC simulation.

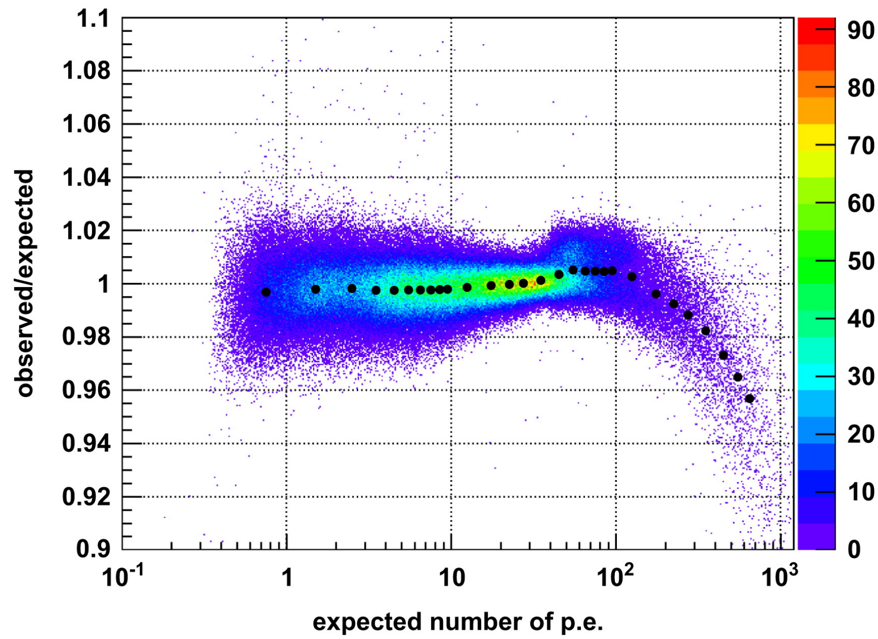

Figure 2.15: PMT response linearity [10].

2.7.4 Timing Response

The relationship between the time when a photon hits a PMT and the time when the PMT pulse crosses the discriminator threshold is effected by PMT transit time, cable lengths, and electronics readout time. Additionally, larger pulses will cross the discriminator threshold faster, and so appear to be earlier hits than smaller pulses, a phenomenon known as "time-walk". All of these effects must be accounted for by calibration.

A nitrogen laser is used to perform timing calibration. The laser produces fast pulses of light with 0.4 ns FWHM. These pulses are monitored by a fast response PMT, which defines the time of the pulse. The laser light is wavelength shifted to 398 nm, and injected in a diffuser ball in the center of the SK tank, which results in isotropic light. A variable optical filter is used to vary the intensity of the light.

During these laser runs, hits in ID PMTs are time-of-flight (TOF) subtracted based on the location of the diffuser ball to account for the time it takes the light

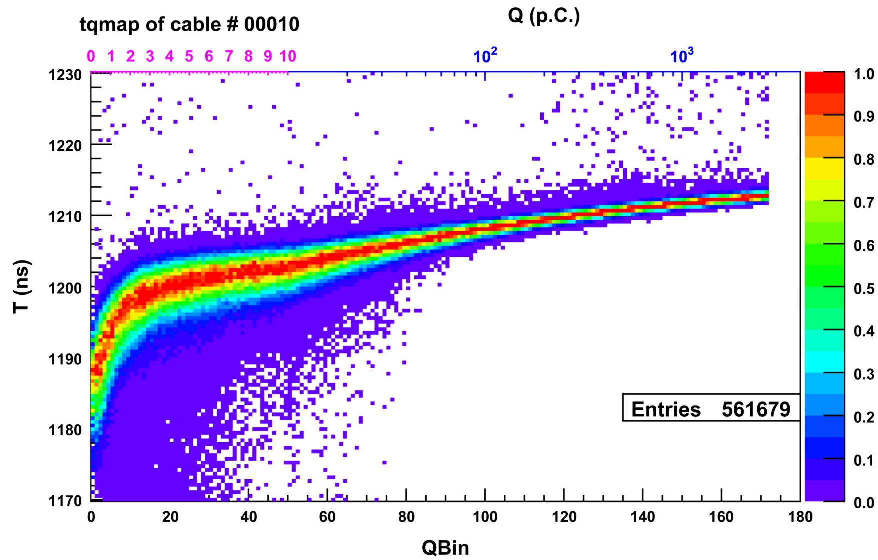

Figure 2.16: TQ-map for a PMT. In this figure larger T corresponds to earlier times, while smaller T corresponds to later times [10].

to travel from the diffuser ball to the particular PMT. These "residual" times are then compared to the reference time of the laser pulse, based on the monitor PMT. This comparison gives a conversion between the time that the PMT pulse crosses the discriminator threshold and the time the light actually hit the PMT. To account for time-walk, this comparison is done as a function of the charge recorded by the PMT, and is called a "TQ-map". An example TQ-map for a PMT is shown in Fig. 2.16

Chapter 3

Data Processing

Super-Kamiokande records around 10^6 events every day. However, the vast majority of these events are either low energy radioactive backgrounds ($\sim$11 Hz) or cosmic ray muons ($\sim$3 Hz). For comparison, the rate of atmospheric neutrino interactions in SK is about 10 per day. Data reduction is used to select only the reatively small number of interesting physics events. In the high energy range ($>$ 100 MeV), three samples are used, each selected by a distinct data reduction process:

- Fully Contained (FC) reduction selects events with activity in the ID and no activity in the OD. These events are the best reconstructed, since all the deposited energy is contained within the ID.

- Partically Contained (PC) reduction selects events with activity in both the ID and OD, but where it has been determined that the primary particle started in the ID and exited into the OD. These events are almost all muons, since most electromagnetic showers will not have the energy to puncture from the FV into the OD. Much of the energy of these events can be deposited outside the ID, and even outside the OD, meaning that energy often cannot be reconstructed as precisely for PC events as it can for FC events.

- Upward Going Muons (UPMU) reduction selects events with activity in both the ID and the OD, where the event starts in the OD, but where the event is coming from below the horizon. Since these events come from below, the Earth acts as a shield for the detector, removing the cosmic ray background. These events are thus due to neutrinos interacting in the rock below the detector.

3.1 Fully Contained Reduction

The FC data reduction consists of five steps, labeled FC1-FC5. Combined, they select around 8 events per day from the 10^6 events recorded by SK, with an efficiency for selecting events which originate in the FV of about 98%. The FC samples contains the events which pass the cuts described here.

3.1.1 FC1

FC1 consists of a two simple cuts:

- The number of pe in a 300 ns sliding time window in the ID is greater than 200 (100 for SK-II).
- There are fewer than 50 (55 for SK-IV) OD hits between -500 ns and +300 ns.

The first cut removes low energy radioactive background events and solar neutrinos, while the second cut removes obvious cosmic ray muon and PC or UPMU events. Of the 10^6 events recorded by SK each day, about 3,500 pass FC1.

3.1.2 FC2

FC2 also consists of two simple cuts:

- No ID PMT can be responsible for greater than 50% of the pe observed in the ID.

- If the number of pe in the ID is less than 100,000 (50,000 for SK-II), there must be fewer than 25 hits in the OD between -500 ns and +300 ns (30 for SK-IV).

This first cut removes electrical noise events where a single large pulse on one PMT accounts for most of the measured ID charge. The second cut is a stricter version of the second FC1 cut, but allows for situations where a very high energy event which is contained to the ID may have more OD hits than lower energy events in the ID, due to electronic cross-talk between channels [1] Of the about 3000 events which pass FC1 each day, about 900 pass FC2.

3.1.3 FC3

Compared to FC1 and FC2, FC3 consists of more complicated sets of cuts designed to remove particular classes of events which are sometimes able to pass FC1 and FC2. First, very high energy muons with $E \gtrsim 1$ TeV loose much of their energy through bremsstrahlung and pair production as opposed to ionization. Because of this, these muons can make a large number of OD hits in a short period of time, but still not enough hits to trigger one of the OD cuts in FC1 or FC2. To remove these events then, the following cut is applied:

- There must be fewer than 40 OD hits in a 500 ns sliding window.

[1]As will be discussed in Section 6.9, in very high energy events (> 20 GeV) sometimes there is such significant electronic cross-talk that this adjustment is not enough. Please see Section 6.9 for a discussion of how FC reduction can be adjusted to avoid problems of electronic cross talk in very high energy events.

To remove through-going muons which are not so high energy, a through-going muon fitter is applied under certain conditions. If an event has greater the 1000 ID hits and at least one ID PMT with greater than 230 pe, then the fitter is applied. The fitter assumes the entry point to be the first hit ID PMT, and the exit point to be the center of the ID exit cluster. A goodness by comparing the timing of hits to the expectation from MC. If there are eight or more hits in the OD within 8 meters of both the entry and exit points, then the through going muon fitter goodness must be less than 0.75.

A similar fitter is applied to remove stopping muons, although for this fitter only an entry point and a direction of the muon are assumed. If there are 10 or more OD hits (5 or more for SK-I) within 8 meters of the entry point, the stopping muon fitter goodness must be less than 0.0 (0.5 for SK-I).

Muons can also enter the ID with minimal OD activity by passing through gaps in the OD PMT coverage where the PMT cables pass into the detector, as shown in Fig. 3.1. There are 12 such gaps in the SK detector, and four of them are instrumented with plastic scintillator paddles which act as hardware vetos. To remove cable hole, muons, if the stopping muon fitter has a goodness greater than 0.0, there must not be a veto paddle which registered a hit within 4 meters of the assumed muon entry point. Further cuts to eliminate cable hole muons are performed in FC5.

In order to remove low energy events, a time-of-flight (TOF) based "point-fit" vertex fitter is used to select a vertex for the event. This fitter is a timing based fitter, which searches for a vertex in the detector which minimizes the spread in the residual time distribution of PMT hits. PMT hits are TOF subtracted to this "point-fit" vertex, and the number of ID hits in a sliding 50 ns residual time window must be 50 or more (25 or more for SK-II).

Low energy events can evade this cut if they occur in coincidence with a cosmic

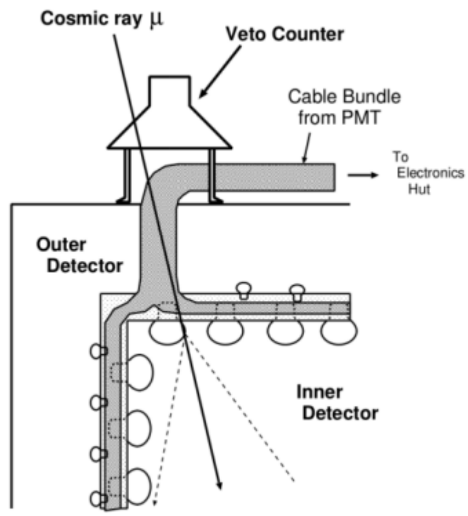

Figure 3.1: Gaps in OD PMT coverage, through which cosmic ray muons can pass with minimal OD activity [18].

ray muon. If the muon arrives just after the low energy event, the energy deposited by the muon allows the event to pass cuts meant to remove low energy events, while the hits in the OD occur to late to be picked up on by OD cuts up to this point. To remove these "coincidence muon" events, if there are 5,000 or more pe in the ID (2,500 or more for SK-II), there must be fewer than 20 OD hits between +300 ns and +800 ns.

Another type of event which must be removed are so-called "flasher" events. These are events where an individual PMT experiences an electrical discharge that produces some light, that can be detected by nearby PMTs. These flasher events generally have longer tails in their timing distributions than true neutrino events. To search for flashers, the minimum number of ID hits in a 100 ns sliding window which searches in the region from +200 ns to +700 ns is found. The following cut is then applied

- (For SK II-IV) The minimum number of ID hits in the 100 ns sliding window must be less than 20.

- (For SK-I) The minimum number of ID hits in the 100 ns sliding window must be less than 10, unless there are more than 800 ID hits, in which case the minimum number of ID hits in the 100 ns sliding window must be less than 15.

The long tail of flasher events makes the "point-fit" perform poorly, so the point-fit goodness must be great than 0.4.

Of the about 900 events that pass FC2 each day, only about 80 pass FC3. The complex reconstruction software "APFIT", which will be described in detail in Chapter 4, is applied to all events which pass FC3.

3.1.4 FC4

FC4 specifically targets flasher events which have made it through the flasher cuts in FC3. The algorithm used in FC4 is based on the idea that flasher tubes will result in multiple events with very similar hit patterns. A database of events is maintained, and each event is compared to events in the database. To compare events, two variables are used. First a variable r is computed, which represents the spacial correlation between two events. The ID wall is segmented into patches about 4 m^2 in size. Comparing two events A and B, r is calculated as:

$$r = \frac{1}{N} \sum_{i}^{N} \frac{(Q_i^A - < Q^A >) \times (Q_i^B - < Q^B >)}{\sigma^A \sigma^B}. \tag{3.1}$$

where N is the number of patches, Q_i is the summed charge (in pe) in the i^{th} patch, and σ is the RMS of Q_i. The variable r is then increased by 0.15 if the highest charge tube in events A and B is the same. Next, a variable d_{ks} is calculated, which is the Kolmogorov-Smirnov test applied to the distribution of charge in the different patches. For a particular event, the 10 largest values of r and smallest values of

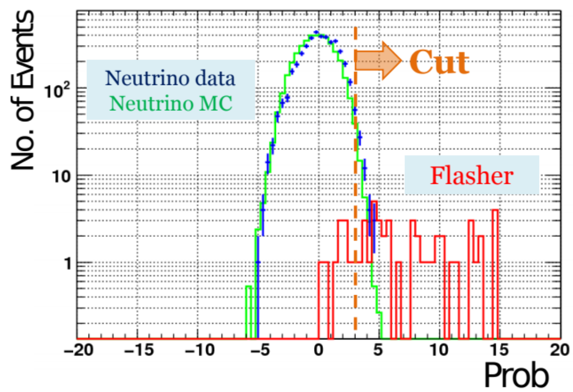

Figure 3.2: Likelihood variable used for flasher cut in FC5 [19].

d_{ks} (large values or r and small values of d_{ks} indicate similar hit patterns) are used to compute a likelihood variable based on the expectation for flasher events. If the likelihood variable is greater than a cut threshold, then the event is removed, as shown in Fig. 3.2. FC4 removes a few events each day.

3.1.5 FC5

FC5 focuses on a removing a few particular types of events from the final sample. First are muons which drop below Cherenkov threshold while traversing the OD. Known as "invisible" muons, these can leave minimal activity in the OD, but then decay to an electron in the ID which will trigger the detector. Therefore, if the number of pe in the ID is less than 1000 (500 for SK-II), which corresponds to the maximum energy of a Michel electron, the following procedure is used to remove these events. Two clusters of OD hits are defined. One is the number of clustered OD hits in a 200 ns sliding window with searches from -9000 ns to -200 ns. This cluster corresponds to hits from before the muon dropped below Cherenkov threshold. The second is the number of clustered OD hits between -200 ns and 300 ns. If the locations of the two clusters are less than 500 cm apart, the number of hits in the early cluster must be less than 5, or the number of hits in the two clusters combined must be less than 10. Otherwise, the number of hits in the early cluster must be less than 10.

Coincidence muons which were not removed during FC3 are targeted by the next cut. If there are fewer than 300 pe in the ID, the number of OD hits in a 200 ns sliding time window search from +300 ns to +2100 ns must be less than 20. This cut searches a wider late time region than the FC3 coincidence muon cut, but only for very low energy events.

An additional set of cuts to remove cable hole muons which passed FC3 is applied for SK-IV only. If the stopping muon fitter's goodness is greater than 0.4 and there are more than 1000 pe in the ID and the fitted direction of the muon comes from greater than 37° above the horizon, the distance between the stopping muon fit entry point and the nearest cable hole must be greater than 2.5 m.

There is also a cut based on the APFIT reconstructed direction, aimed at removing stopping muons:

- There must be fewer than 4 OD hits within 8 m of the APFIT entry point in a 200 ns sliding window between -500 ns and +300 ns.

Finally, there is an additional cut to remove flasher events which made it through FC3 and FC4. This cut is based on a more complex timing based vertex fitter than was used in FC3. Similarly to the vertex fitter used in FC3, the goodness of the fit is expected to be low for flasher events with long timing tails. As in FC3, the minimum number of ID hits in a sliding 100 ns window between +200 ns and +700 ns is found. If the minimum number of hits in the 100 ns window is six or greater, then the goodness of the vertex fit must be better than 0.4. For SK II-IV, a looser cut on the goodness is applied if the minimum number of hits in the 100 ns window is less than 6. In that case, the goodness of the vertex fit must be better than 0.3.

Like FC4, only a few events each day are removed by FC5, leaving an event rate of 50-80 events per day.

3.1.6 Final Analysis Sample

The events passing FC5 still contain some background, mostly in the form of low energy radioactive background. To produce the final analysis sample, three final cuts are applied:

- The distance from the reconstructed vertex to the ID wall must be greater than 2 m.
- The reconstructed visible energy must be greater than 30 MeV.
- The maximum number of hits in an OD cluster must be less than 16 (less than 10 for SK-II).

After these cuts, about 8 events per day remain, which agrees well with atmospheric neutrino MC expectation. This final analysis sample is called "Fully-Contained Fiducial Volume" (FCFV), and it is estimated that the efficiency of the FCFV selection for selecting neutrino events in the FV which do not penetrate the OD is about 98%. The fraction of FCFV events which are background is estimated to be around 0.3%-0.4% in SK II-III, and 0.02% is SK-IV [19].

3.2 Partially Contained Reduction

The PC reduction searches for muons that originated in the ID but were able to penetrate into the OD, as in Fig. 3.3. Similarly to the FC reduction, this is done in a sequence of five steps, labeled PC1-PC5. The PC reduction selects about two events every three days from the 10^6 events recorded by SK. Between SK-II and SK-III, the top, bottom, and barrel of the OD were optically separated from one another. This segmentation allowed for a more efficient PC selection from SK-III onward. I will describe here the PC selection in SK-III and SK-IV. A description of the selection for SK-I and SK-II can be found in [20].

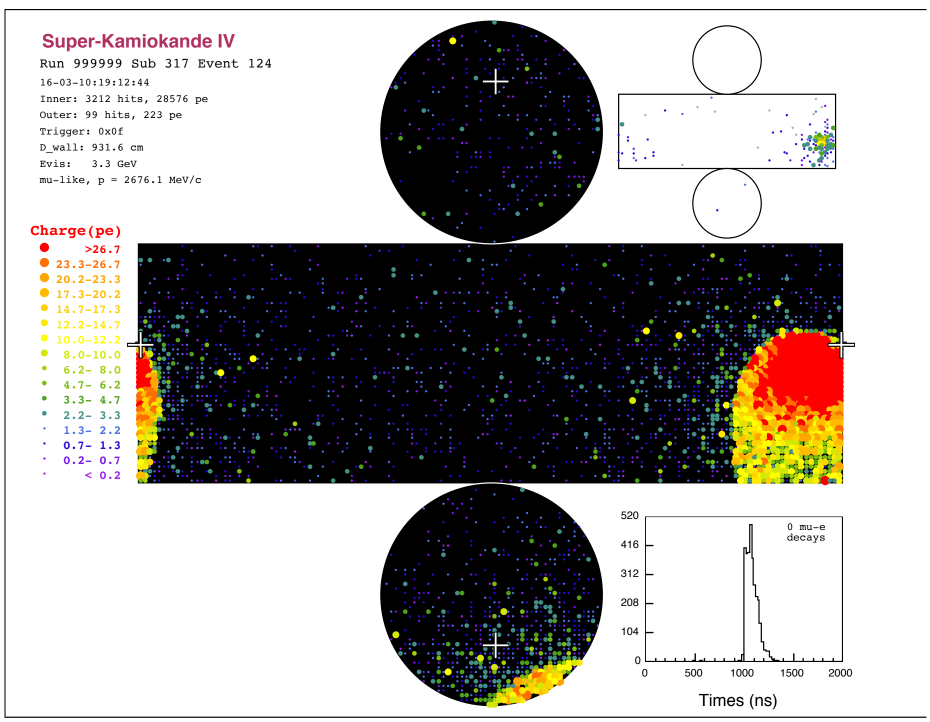

Figure 3.3: A Partially Contained MC event.

3.2.1 PC1

PC1 consists of a few simple cuts. First, since PC events must be able to penetrate from the FV to the OD, there must be enough light deposited in the ID to indicate the particle had enough energy to travel at least 2 meters. So, there must be at least 1000 pe deposited in the ID.

Next are cuts to remove events with more than one cluster of hits in the OD. First, are two simple cuts on the numbers of hits in the three different sections of the OD.

- There cannot be 11 or more hits in the top section of the OD along with 10 or more hits in the bottom section of the OD.
- There cannot be more than 28 hits total in the OD top and bottom along with 84 or more hits in the OD barrel.

Next, a simple variable ODR_{mean}, which is the average distance between pairs of hits, is calculated:

$$ODR_{mean} = \frac{1}{N_{pair}} \sum_{i} \sum_{j \neq i} |\vec{x_i} - \vec{x_j}|. \tag{3.2}$$

Since ODR_{mean} should be smaller when there is only one cluster of hits in the OD, ODR_{mean} must be less than 2140 cm. Of the 10^6 events recorded by SK each day, about $34,000$ event per day pass PC1.

3.2.2 PC2

PC2 continues removing events with more than one cluster of hits in the OD. First, a clustering algorithm is applied, where the OD is divided into 121 patches, and the hits in each patch are merged into the neighboring patch with the most hits.

Based on these clusters, there can be no more than one OD cluster with 10 or more hits.

Next, a cut is applied similar to the cuts on the numbers of top and bottom and barrel hits from PC1. A function of the number of hits in the OD barrel is defined:

$$f(n_{ODbarrel}) = \begin{cases} e^{5.8-0.023n_{ODbarrel}}, n_{ODbarrel} < 75 \\ e^{4.675-0.008n_{ODbarrel}}, \text{else.} \end{cases} \tag{3.3}$$

If there are 20 or more total hits in the OD top and bottom, the total number of OD top and bottom hits must be less than $f(n_{ODbarrel})$. The functional form of $f(n_{ODbarrel})$ is such that this is a more finely tuned version of the cuts in PC1, allowing events with a large number of hits in the OD barrel or endcaps, but not both.

Of the about $34,000$ events which pass PC1 each day, about 11,000 pass PC2.

3.2.3 PC3

PC3 removes flasher events using the same technique as FC3. The minimum number of ID hits in a 100 ns sliding window which searches in the region from +200 ns to +700 ns is found, and the following cut is then applied:

- The minimum number of ID hits in the 100 ns sliding window must be less than 10, unless there are more than 800 ID hits, in which case the minimum number of ID hits in the 100 ns sliding window must be less than 15.

Only a small number of events are removed by PC3.

3.2.4 PC4

For PC4, two fitters are applied. The first is a dedicated entering muon fitter which assumes a muon starting outside the ID, and defines the entrance point as the earliest hit ID cluster. This fitter is called “muboy” and labels the event as either stopping, though-going, multiple muons, or corner clippers. Most events originating outside the ID are categorized as stopping or through-going, while most events originating inside the ID are categorized as multiple muons or corner clippers by this fitter. This fitter also finds worse goodness-of-fit for events originating inside the detector, since is explicitly assumes a vertex outside the ID as part of its fitting procedure. The second fitter is a simpler “point-fit” fitter, which determines vertex position reasonably well for events originating both inside and outside the ID. From these two fits, the following five “soft cuts[2]” are defined:

- (soft cut) The angle between the muboy direction and the direction from the point-fit vertex to the OD cluster with the most charge must be less than 90°.
- (soft cut) The angle between the muboy direction and the direction from the point-fit vertex to the earliest saturated ID pmt must be less than 143.13°.
- (soft cut) The length of the muboy track must be less than 1750 cm.
- (soft cut) The goodness of the muboy fit must be less than 0.52.
- (soft cut) The distance from the corner of the tank to the muboy entrance point must be 300 cm or larger.

If an event is classified as multiple muons or corner clipper, then is must pass two of the five cuts. If it is classified as through-going, then is must pass four of the five

[2] “soft cuts” are cuts which events can fail while still passing the selection. Generally events are allowed to fail a certain number of a set of soft cuts.

cuts. If it is classified as stopping then it must pass four of the five cuts, in addition to one of the following two soft cuts:

- The goodness of the muboy fit must be less than 0.5.
- There must be fewer than 10 hits in the OD within 8 m of the muboy entrance point in a fixed 500 ns window.

Of the about 11,000 events which pass PC1-PC3 each day, about 900 pass PC4.

3.2.5 PC5

PC5 consists of a sequence of specialized cuts to remove different types of background. First are two sets of cuts to remove through going muons. The first set applies a clustering algorithm like the one applied in PC2, but with the OD divided into only 36 patches. If there are more than two clusters with at least 10 hit PMTs, then the clusters found in PC2 are considered. If the second highest charge cluster found in PC2 has 10 or more pe's, the distance between the two highest charge clusters found in PC2 must be less than 20 m.

The next set of through going muon cuts removes muons which enter and exit the detector near the edges of the top and bottom of the detector. To remove these events, combinations of 8 m spheres centered on the edges of the top and bottom of the detector are examined, and the following cut is applied:

- There cannot be a combination of an 8 m sphere on the top edge and an 8 m sphere on the bottom edge which satisfy the following criteria:
  - Seven or more OD hits within both spheres.
  - Ten or more pe within each sphere.

– The time interval between the average hit time in the two spheres is more than 0.75c/40 m and less than 1.5c/40m.

Next is a cut to remove stopping muons. For this cut, two event reconstruction algorithms are applied, which find vertices and directions of Cherenkov rings. The angle between the direction to the largest OD hit cluster and the direction of the first Cherenkov ring must be less than 90°.

Next, cable hole muons are removed using the veto counters described in FC3. If there is a hit veto counter, the cosine of the angle between the TDC-fit ring direction and the direction from the hit veto counter to the reconstructed vertex must be less than 0.8.

Finally, corner clipping muons are removed by requiring that the shortest distance from the fitted vertex to a corner of the ID must be more than 150 cm.

In addition to these cuts, a number of "soft cuts" are also applied. Events can fail at most one soft cut and still pass PC5 reduction. First are two soft cuts to remove through-going muons. The first takes the vertex and direction of a precise Cherenkov ring fitter, and extrapolates forward and backward from the vertex along the direction of the ring to find an entrance and exit point. If the time interval between the average time of OD hits within 8 m of the entrance point and OD hits within 8 m of the exit point is between 0.75 and 1.5 times the speed of light divided by the distance between the entrance and exit points, then the following soft cut is applied:

- (soft cut) There cannot be more than 5 hit OD PMTs within 8 m of both the entrance and exit points.

The second through-going muon soft cut uses the 36 patch OD clustering algorithm. The following soft cut is applied:

- (soft cut) There cannot be 17 or more hits in one OD cluster along with 10 or more hits in another OD cluster.

Next are soft cuts to remove stopping muons. The first again takes the extrapolated entrance point of the track, and counts the number of hit OD PMTs within 8 m of the entrance point. The following soft cut is applied:

- (soft cut) There cannot be 10 or more hit OD PMTs within 8 m of the entrance point.

The next stopping muon soft cut uses a stopping muon fitter, which chooses as the entrance point the position of the earliest hit ID cluster, and reconstructs the direction of the muon track. Events which started in the ID will be badly reconstructed by this fitter, since the assumption of an entrance point is incorrect. The following soft cut is the applied:

- (soft cut) The below criteria of a good stopping muon fit cannot all be satified:
  - The goodness of the stopping muon fit is positive.
  - 60% or more of observed ID pe's are within a 42° cone around the fitted muon direction.
  - There are more than 6 OD hits within 8 m of the entrance point.

The third stopping muon soft cut compares the results of two fitters. If the extrapolated entrance points for the fitters are within 15 m of each other, then the following soft cut is applied to the result of one of the fitters.

- (soft) There can be no more than 10 OD hits within 8 m of the entrance point.

If the extrapolated entrance points are not within 15 m of each other, then the above soft cut is applied to both entrance points. The final stopping muon soft cut is a reapplication of one of the soft cuts from PC4:

- (soft cut) The angle between the muboy direction and the direction from the point-fit vertex to the OD cluster with the most charge must be less than 90°.

The next soft cut removes corner clipping muons. Corner clipping muons often have a single small hit cluster in the ID, and a mis-reconstructed vertex somewhere away from this cluster in the ID. This soft cut compares two estimated track lengths. One is the distance between the reconstructed vertex and the exit point, and the other is found by dividing the visible energy of the event by 2 MeV/cm. The following soft cut is then applied:

- (soft cut) The vertex based track length cannot be more than 15 m longer than the energy based track length

Finally, a decay electron soft cut is applied. Since high energy neutrino events will interact mostly though DIS and produce charged pions which will decay to muons which will decay to electrons, the following soft cut is applied to events with more than 25 GeV of visible energy:

- (soft cut) There must be at least 1 decay electron in the event.

Of the about 900 events which pass PC1-PC4 each day, only about 1.2 pass PC5.

3.2.6 Final Analysis Sample

The final PC analysis sample is selected from the events passing PC1-PC5 by the following final cuts:

- The reconstructed vertex must be more than 2 meters away from the ID wall.

- The reconstructed visible energy must be greater than 350 MeV.

- There must be an OD hit cluster with at least 16 hits.

After these final analysis cuts about two events every three days remain. The efficiency of the selection is estimated to be around 85%, and the background contamination is estimated to be less than 1%.

3.2.7 PC Stopping/PC Through-Going Separation

PC events are further categorized as either stopping (the muon stopped in the OD) or through-going (the muon passed through and exited the OD). This categorization is done by comparing the number of OD pe's in a 500 ns sliding window to the number expected if the muon had passed through and exited the OD. If the number of observed pe is less than 67% the expectation for a through going muon, the event is categorized as PC Stopping, otherwise it is categorized as PC Through-Going. sectionUpward Going Muon Reduction The UPMU data reduction searches for high energy muons which enter the detector from below the horizon. Because the earth is acting as a shield for events in these direction, all cosmic ray background in removed (except for nearly horizontal events), so upward going muons must come from neutrino interactions below and around the detector. The reduction is performed by the application of a simple charge cut, followed by seven dedicated muon fitters to ensure that the event is upward going.

3.2.8 Charge Cut

Only upward going muons with a path length of greater than 7 m are used for physics analysis. As a conservative step toward this goal, the total charge deposited in the ID must be greater than 8000 pe. This cut corresponds to the amount of charge expected from a muon with a path length of 3.5 m. Additionally, if too much charge is deposited in the ID, the muon fitters applied in the next step of the UPMU reduction can perform poorly. Therefore, in order to save very high energy astophysical events, events with more than 1,750,000 p.e. are automatically passed to the eye-scanning step of the UPMU reduction (Section 3.2.10).

3.2.9 Dedicated Muon Fitters

Seven dedicated muon fitters are then used to determine if the event is an upward going muon. The different fitters specialize in fitting different types of muon events. The fitters are applied sequentially, and for each fitter, the following logic is applied:

- If the goodness of the fit is above a threshold and the event is fit as upward, the event passes the selection (no additional fits are applied).
- If the goodness of the fit is above a threshold and the event is fit as downward, the event is rejected (no additional fits are applied).
- If the goodness of the fit is below the threshold or the event is fit as horizontal, the event is passed to the next fitter.

If none of the fitters have a goodness above threshold then the event is rejected. However, if at least one fit has a goodness above threshold but all fits with a goodness above threshold fit the event as horizontal, then the event passes the selection. Events which pass the selection are then fit with a more sophisticated "precise-fit". If the reconstructed cosine of the zenith angle from the precise-fit is negative, the event is selected as upward going.

3.2.10 Eye Scanning

Only about half of events which make it through the charge cuts and dedicated muon fitters are true upward going muons. To remove the other background events, all events which are passed through those cuts are eye-scanned by two physicists. Since these events are easy for humans to recognize visually, the efficiency of the eye-scanning procedure is estimated to by essentially 100%.

3.2.11 Stopping and Through-Going Selection

UPMU event selection is further subdivided into stopping and through-going selection. For events passing the Eye Scanning, stopping UPMU selection consists of the following cuts:

- The event must be categorized as stopping by a dedicated muon fitter.
- The fitted momentum must be greater than 1.6 GeV.
- The number of OD hits within 8 m of the projected exit point must be less than 10.

Selection for through-going UPMU events consists of related cuts:

- The event must be categorized as through-going by a dedicated muon fitter.
- The distance between the ID entrance and exit points must be larger than 7 m.
- the number of OD hits within 8 m of the exit point must be 10 or greater.

The UPMU stopping selection selects about 0.25 events per day, while the UPMU through-going selection selects about 1.2 events per day. The efficiency of both selections are estimated to be about 99%.

3.2.12 Through-Going Showering/Non-Showering Separation

Through-Going muons are further separated into "showering" and "non-showering". Non-showering events deposit energy at a continuous, consistent rate, whereas showering events deposit large amounts of energy is short bursts through radiative effects such as Bremstrahlung radiation. Events are separated into showering and non-showering by comparing the observed charge distribution to that expected from a non-showering event. If there is good agreement, the event is classified as non-showering. Otherwise the event is classified as showering.

Chapter 4

Event Reconstruction

Reconstruction of events is an essential step in physics analysis at Super-Kamiokande. Reconstruction converts the raw hit information recorded in the PMTs into more understandable physics quantities, which can then be used in physics analyses. Reconstruction of SK events consists primarily of finding the vertex location and counting, classifying, and assigning energy and direction to Cherenkov rings. Additionally, activity after the primary event, such as decay electrons and neutron captures, can be tagged. In this chapter, I will discuss reconstruction of FC events. Since I was in charge of maintenance and continued application of the neutron tagging algorithm, and neutron tagging results are of great importance to the boosted dark matter search presented in Chapter 6, the description of the neutron tagging algorithm will be presented in particular detail.

4.1 Vertex Reconstruction

Vertex reconstruction begins with the concept of "residual time". Residual time is "time-of-flight" subtracted, and can be calculated for a hit at raw time t_i^{raw} on a

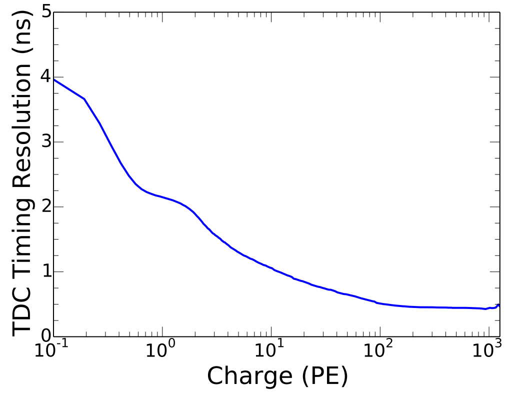

Figure 4.1: Timing resolution as a function of charge deposited in PMT. Used in Eq. (4.2).

PMT at position $\vec{p_i}$ for a vertex at $\vec{x}$ as

$$t_i^{resid}(\vec{x}) = t_i^{raw} - \frac{n}{c}|\vec{p_i} - \vec{x}| \tag{4.1}$$

where n is the index of refraction of water (about 1.36). The residual time is thus the time of production of the photons assuming they were produced at the vertex $\vec{x}$ and experienced no scattering on their way to the PMT. Since we expect all the Cherenkov light to be produced in a short time period from a small region in space, we expect that most hits should have very similar residual times when the correct vertex is used. The initial vertex reconstruction is therefore performed by choosing the vertex to maximize a goodness of fit which is related to the width of the residual timing peak:

$$G_{\vec{x},1} = \sum_i \frac{1}{\sigma_{TDC}(q_i)} \exp\left(-\frac{(t_i^{resid} - t_0)^2}{2 \times (1.5\sigma_{TDC}(q_{avg}))^2}\right). \tag{4.2}$$

Here t_0 is a free parameter which is the time of the peak, and $\sigma_{TDC}(q)$ is the timing resolution as a function of charge deposited in the PMT, which is shown in Fig. 4.1.

Once a reasonable starting vertex has been found, the brightest ring is sought.

First, a vector sum of hit PMTs weighted by corrected charge is computed. Corrected charge is the charge deposited in a PMT corrected for light attenuation over the distance traveled from the reconstructed vertex, and for the angular acceptance of the PMT, $f(\theta)$:

$$q^{corr} = q^{obs} e^{r/L_{atten}} \frac{\cos\theta}{f(\theta)} \tag{4.3}$$

where q^{obs} is the measured raw charge, r is the distance from the vertex to the PMT, L_{atten} is the attenuation length of the water, and θ is the angle of incidence from the vertex to the PMT. The vector sum of hit PMTs weighted by corrected charge is taken as a very rough guess of the direction of the brightest ring. Various adjustments are made to this direction, until finally a first ring and Cherenkov opening angle are chosen by maximizing the following goodness-of-fit:

$$G_{\vec{d_1},\theta_C} = \frac{1}{\sin\theta_C} \left(\left. \frac{dq^{corr}}{d\theta} \right|_{\theta_C} \right)^2 \exp\left(-\frac{\theta_C - \theta_{exp}}{2\sigma_\theta^2} \right) \int_0^{\theta_C} q^{corr}(\theta) d\theta \tag{4.4}$$

where $q^{corr}(\theta)$ is the corrected charge (as calculated in Eq. (4.3)) as a function of opening angle around the ring direction being tested d_1, θ_C is the Cherenkov opening angle being tested, σ_θ is the angular resolution, and θ_{exp} is the expected Cherenkov opening angle. Three values of θ_{exp} are tested. First, $\theta_{exp} = 42°$, which corresponds to the maximum Cherenkov opening angle in water. Second, a rough estimate of the momentum of the particle assuming it is a muon is made, and θ_{exp} is calculated from Eq. (2.1). Third, an estimate of the expected Cherenkov ring is made from the light pattern assuming the particle is an electron.

Once the brightest ring and opening Cherenkov angle for that ring have been found, the vertex search is redone with the residual time of each hit within the Cherenkov ring adjusted from Eq. (4.1). First an emission point $\vec{e_i}$ is found along the direction of the ring for each hit within the Cherenkov ring by intersecting the direction of the ring from the vertex x being tested with a ray to the i^{th} PMT at the correct Cherenkov angle. The adjusted residual time is then calculated for hits inside the Cherenkov ring as:

$$t_i^{resid}(\vec{x}) = t_i^{raw} - \frac{1}{c}|\vec{x} - \vec{e_i}| - \frac{n}{c}|\vec{p_i} - \vec{e_i}|. \tag{4.5}$$

Hits outside the Cherenkov ring still use the residual time from Eq. (4.1). The vertex is then found by maximizing the goodness-of-fit summed over each hit. For hits within the Cherenkov ring, the goodness-of-fit is Eq. (4.2), where the residual time is from Eq. (4.5). For hits outside the Cherenkov ring, the goodness-of-fit is

$$G_{outside} = \begin{cases} \sum_i \frac{1}{\sigma_{TDC}(q_i)} \left(\exp\left(-\frac{(t_i^{resid} - t_0)^2}{2\times(1.5\sigma_{tdc}(q_{avg}))^2} \right) \times 2 - 1 \right), \text{for } t_i \leq t_0 \\ \sum_i \frac{1}{\sigma_{TDC}(q_i)} \left(\max\left[\exp\left(-\frac{(t_i^{resid} - t_0)^2}{2\times(1.5\sigma_{tdc}(q_{avg}))^2} \right), G_{scatt}(t_i, t_0) \right] \times 2 - 1 \right), \text{else} \end{cases} \tag{4.6}$$

where

$$G_{scatt}(t_i, t_0) = \frac{R_C}{1.5^2} \exp\left(-\frac{(t_i^{resid} - t_0)^2}{2 \times (1.5\sigma_{tdc}(q_{avg}))^2} \right) + \left(1 - \frac{R_C}{1.5^2} \right) \exp\left(-\frac{t_i - t_0}{\sigma_{scatt}} \right) \tag{4.7}$$

where R_C is the fraction of the total charge which is inside the Cherenkov ring and $\sigma_{scatt} = 60$ ns.

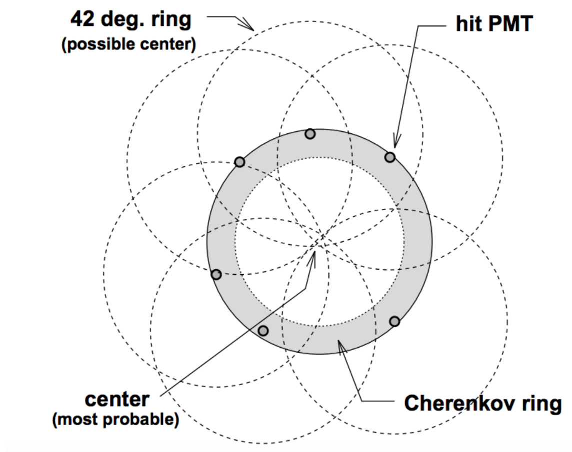

Figure 4.2: Visualization of Hough transform. The gray circle is the Cerenkov ring, and the dotted circles are the circles drawn around hit PMTs. Their intersection represents the direction of the ring [21].

4.2 Ring Counting

Once the vertex and first ring [1] of the event have been found, the number of Cherenkov rings is counted. Candidate rings are first found using a Hough transform, which changes a ring finding search into a peak finding search. The idea of a Hough transform is to draw circles of 42° half-opening angle around hit PMTs. The overlap of all of these circles then corresponds to a candidate ring direction, as shown in Fig. 4.2. In this particular application, instead of a simple circle, an expected charge distribution function $f(\theta)$ is weighted by the observed charge and mapped onto the (Θ, Φ) plane for each hit PMT. Peaks in the resulting map correspond to candidate rings. An example map for a two ring event is shown in Fig. 4.3

Candidate rings are then considered iteratively through a likelihood method, which compares the hypothesis of adding an $(\mathrm{N}+1)^{th}$ ring to the hypothesis of including only

[1]It is important to note that the “first ring” is simply the ring found by the algorithms in Section 4.1. While the first ring is often the most energetic ring, it should be remembered that this is not always the case.

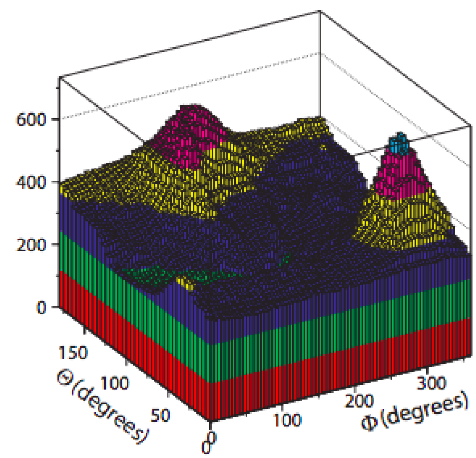

Figure 4.3: Example Hough transform map for a two ring event. The peaks are the directions of the two rings [21].

the N rings already found. The likelihood function for a hypothesis of N rings is:

$$L_N = \sum_{i}^{N_{PMT}} \log \left(P(q_i^{obs}, \sum_{j}^{N} \alpha_n q_{i,j}^{exp}) \right), \tag{4.8}$$

where α_j is the weight for the j^{th} ring, which is adjusted with a minimum requirement to maximize L_N, and $P(q_i^{obs}, q_i^{exp})$ is the probability of observing a charge q_i^{obs} in the i^{th} PMT when the expected charge is q_i^{exp}. If $q_i^{exp} \geq 20p.e.$, then this probability is taken to be Gaussian:

$$P(q_i^{obs}, q_i^{exp}) = \frac{1}{\sqrt{2\pi\sigma^2}} \exp\left(-\frac{(q_i^{obs} - q_i^{exp})^2}{2\sigma^2} \right), \tag{4.9}$$

where $\sigma = \sqrt{1.44 q_i^{exp} + (0.1 q_i^{exp})^2}$. If $q_i^{exp} < 20p.e.$, then the probability is computed numerically based on a Poisson distribution. If $L_{N+1} > L_N$, then the candidate ring is added, up to a total of five rings. The multi-ring likelihood $L_{multi} = L_2 - L_1$ is shown for Sub-GeV and Multi-GeV events in Fig. 4.4.

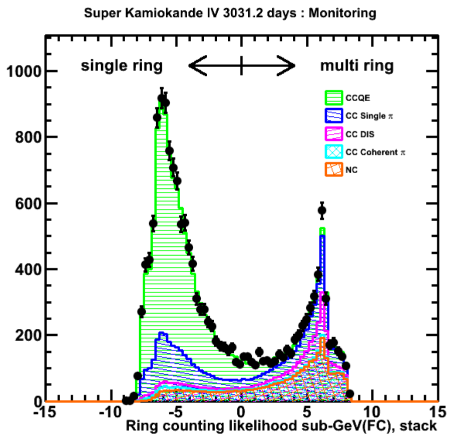

(a) Sub-GeV

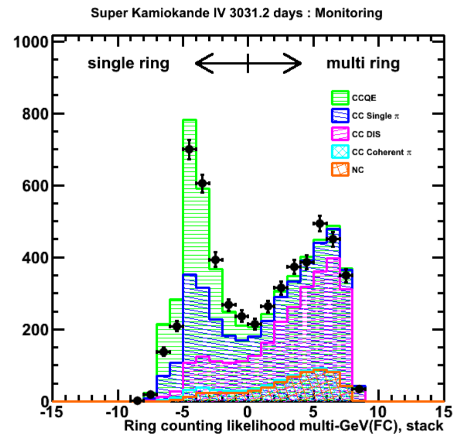

(b) Multi-GeV

Figure 4.4: Multi Ring likelihood $L_{multi} = L_2 - L_1$ for Sub-GeV (left) and Multi-GeV (right) events. The stacked hatched histrograms are MC, while the black dots are Data.

4.3 Particle Identification

Once Cherenkov rings have been identified, each ring is classified as e-like (for electrons and photons) or μ-like (for muons and charged pions). High energy electrons passing through water loose energy through bremsstrahlung, while photons loose energy through pair production. These processes lead to the creation of electromagnetic showers from high energy electrons or photons. Muons and charged pions, conversely, loose energy mostly though ionization, and thus produce Cherenkov rings which are sharper than those produced by electromagnetic showers. Representative event displays of a 1 GeV electron and a 1 GeV muon are shown in Fig. 4.5.

Quantitatively, ring classification is performed by comparing the observed charge to the expected charge under μ-like and e-like hypotheses. The expected charge in

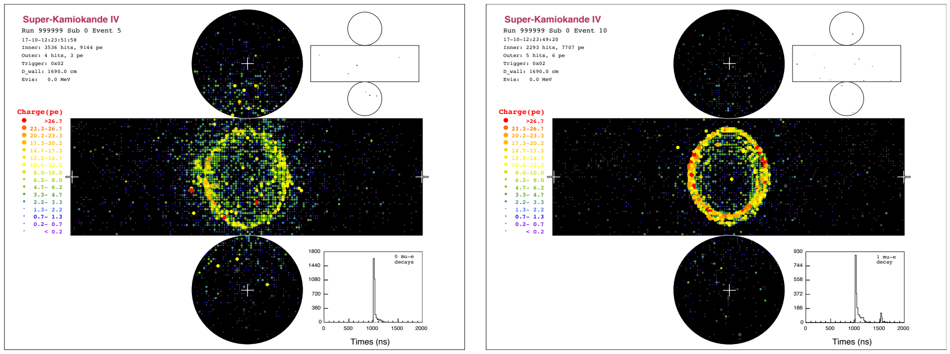

(a) Electron (b) Muon

Figure 4.5: Example event displays of a 1 GeV electron (left) and 1 GeV muon (right). The Cherenkov ring associated with the muon is clearly sharper than that associated with the electron.

the i^{th} PMT due to a ring under each hypothesis is:

$$q_i^{exp}(e) = \frac{\alpha_e f(\Theta_i)}{e^{\frac{r_i}{L}}} \times Q^{exp}(p_e, \theta_i) \times \left(\frac{R}{r_i}\right)^{1.5} + q_i^{scatt}, \tag{4.10}$$

$$q_i^{exp}(\mu) = \frac{\alpha_\mu f(\Theta_i)}{e^{\frac{r_i}{L}}} \times \left(\frac{\sin^2 \theta_{x_i}}{r_i \left(\sin\theta_{x_i} + r_i \left.\frac{d\theta}{dx}\right|_{x_i} \right)} + q_i^{knock} \right) + q_i^{scatt}. \tag{4.11}$$

where $\alpha_{e,\mu}$ are weights for the ring, $f(\Theta_i)$ is the PMT angular acceptance at incident angle Θ_i, r_i is the distance from the vertex to the i^{th} PMT, and L is the light attenuation length of the water. In the e-like expected charge, $Q^{exp}((p_e, \theta_i)$ is the expected charge distribution based on MC for an electron track 16.9 m from the wall as a function of momentum p_e, and the angle θ_i between the direction of the track and the direction from the vertex to the PMT. The factor $(R/r_i)^{1.5}$ corrects this expected charge distribution for the distance from the vertex to the PMT. In the μ-like expected charge, the term in parentheses encodes the angular dependence of expected charge, and also includes the effect of the non-zero track length of the muon, with x_i being the emitted position of the photon along the muon track, and the angle to the PMT θ_{x_i} being calculated based on this position instead of the fitted vertex. The μ-like expected charge also accounts for "knock-on" electrons, which are delta-rays produced by the ionizing muon. Finally, both expected charges account for scattered light in the q_i^{scatt} term.

The expected charge and observed charge are then used to compute a charge pattern likelihood:

$$L_n^{pattern}(e,\mu) = \prod_{\theta_i<1.5\theta_C} P\left(q_i^{obs}, q_{i,n}^{exp}(e,\mu \sum_{j\neq n}^{N_{ring}} q_{i,j}^{exp}\right) \tag{4.12}$$

where the product is over all PMTs within a cone of angle $1.5\theta_C$ around the ring direction, and the probability is as defined in Eq. (4.9). The direction and opening angle of both the μ-like and e-like hypotheses are adjusted to maximize this likelihood. The likelihood is then converted into a χ^2 parameter

$$\chi_n^2(e,\mu) = -2\log L_n^{pattern}(e,\mu) \tag{4.13}$$

which is then converted into a probability

$$P_n^{pattern}(e,\mu) = \exp\left(-\frac{(\chi_n^2(e,\mu) - \min(\chi_n^2(e), \chi_n^2(\mu)))^2}{2\sigma_{\chi_n^2}^2}\right) \tag{4.14}$$

where $\sigma_{\chi_n^2} = \sqrt{2N}$ for the N PMTs include in Eq. (4.12).

If there is only a single Cherenkov ring, a second probability is calculated which compares the reconstructed Cherenkov angle θ^{obs} to the expected angle $\theta^{exp}(e,\mu)$ based on the reconstructed e-like or μ-like momentum:

$$P^{angle}(e,\mu) = \exp\left(-\frac{(\theta^{obs} - \theta^{exp}(e,\mu))^2}{2\sigma_{theta}^2}\right) \tag{4.15}$$

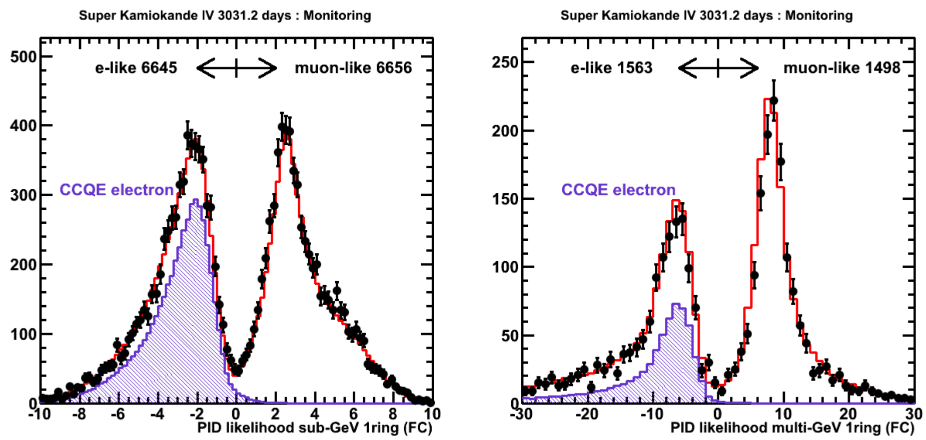

(a) Sub-GeV (b) Multi-GeV

Figure 4.6: PID likelihood distributions for Sub-GeV (left) and Multi-GeV (right) events. The black is Data, the red is oscillated MC, and the hatched histogram is CCQE ν_e events.

where σ^2_{theta} is the angle fitting uncertainty.

The product of the pattern and angle probabilities is then used as the final PID likelihood:

$$P(e,\mu) = P^{pattern}(e,\mu) \times P^{angle}(e,\mu) \tag{4.16}$$

where $P^{angle}(e,\mu) = 1$ is used if the event has more than one Cherenkov ring[2] . The final PID classifier is defined as:

$$L_{PID} = \sqrt{-\log P(\mu)} - \sqrt{-\log P(e)}. \tag{4.17}$$

Here positive values indicate a μ-like ring, while negative values indicate an e-like ring. The distributions of L_{PID} for Data and MC are shown in Fig. 4.6.

[2] Although the official PID reconstruction uses $P^{(}angle)$ for single ring events only, the μ-like and e-like likelihoods for each ring can be found in official SK `ROOT` files both including angle information (in `PROBMS`) and excluding angle information (in `PRMSLG`) for both single-ring and multi-ring events.

4.4 Precise Vertex Reconstruction

For one-ring events, the PID information of the Cherenkov ring is used to improve the vertex fit. The vertex position and ring direction are adjusted iteratively according to the following procedure:

1. The vertex position is adjusted in the plane perpendicular to the direction of the ring to maximize the time based goodness-of-fit used at the end of Section 4.1.

2. The vertex position is adjusted along the direction of the ring to maximize $L_n^{pattern}(\alpha)$ defined in Eq. (4.12), with α set to the PID of the ring.

3. The direction of the ring is adjusted to maximize $L_n^{pattern}(\alpha)$ defined in Eq. (4.12), with α set to the PID of the ring.

This process is then repeated based on the new vertex position and direction of the ring, until the vertex moves less than 5 cm and the direction changes by less than 0.5° between successive iterations, up to a maximum of seven iterations.

4.5 Momentum Reconstruction

The momentum of each ring is estimated by summing up the observed charge associated with each ring. The observed charge in each PMT is divided between the reconstructed rings by:

$$q_{i,n}^{obs} = q_i^{obs} \frac{q_{i,n}^{exp}}{\sum\limits_j q_{i,j}^{exp}}. \tag{4.18}$$

The variable R_j^{tot} is then calculated for the j^{th} ring as:

$$R_j^{tot} = \frac{G_{MC}}{G_{DATA}} \left[\sum_{\substack{\theta_{i,j}<70^\circ \\ -50\text{ns}<t_i<250\text{ns}}} \left(q_{i,j}^{obs} e^{\frac{r_i}{L}} \frac{\cos\Theta_i}{f(\Theta_i)} \right) - \sum_{\theta_{i,j}<70^\circ} S_i \right] \quad (4.19)$$

where G_{MC} and G_{DATA} are the relative PMT gains for MC and data, respectively, r_i is the distance from the vertex to the i^{th} PMT, L is the attenuation length of light in water, Θ_i is the angle of incidence on the i^{th} PMT, $f(\Theta_i)$ is the angular efficiency of the PMT, S_i is the expected scattered light in the i^{th} PMT, and the summations are done over hits within 70° of the ring direction and with a residual time t_i between -50 ns and 250 ns. R_j^{tot} is then converted into momentum by comparing the R^{tot} values for simulated particles of the reconstructed particle type with known momentum.

4.6 Ring Counting Correction

Once momentum is assigned to each ring, a correction is applied to remove low energy mis-fit rings. A lower momentum ring is merged into a higher momentum ring if:

- $\theta_{i,j} < 30^\circ$ and $p_i \cos\theta_{i,j} < 60$ MeV/c

where $\theta_{i,j}$ is the angle between the two rings, and p_i is the momentum of the lower energy ring. A ring is also removed if:

- $p_i < 50$ MeV/c and $p_i/p_{tot} < 0.05$

where p_{tot} is the sum of the momenta of all the rings.

4.7 Decay Electron Search

Decay electrons are searched for out to 20 μs after a primary event trigger. As described in Section 2.5.1, during SK I-III only 1.3 μs of data was recorded around a trigger, so decay electrons must be searched for both in the primary event (these are called "in-gate" decay electrons) and in the events just after the primary event (these are called "sub-event" decay electrons). Sub-event candidates have at least 50 hits (25 for SK-II) but no more than 2000 p.e. deposited (1000 p.e. for SK-II), and occur between 1.2 μs and 20 μs after the primary event. In-gate candidates are found by looking for 30 ns peaks in residual time above background. The background is μ_{bckg} estimated by counting the hits in a short time window before the peak, and scaling to the 30 ns time window of the peak. The fluctuation of this background is then taken as $\sigma_\mu = \sqrt{\mu_{bckg}}$. A peak is accepted as a candidate if

- $N_{peak} - \mu_{bckg} \geq 50$ (25 for SK-II)

and

- $\frac{N_{peak}-\mu_{bckg}}{\sigma_\mu} > 6.63$ (5.17 for SK-II)

where N_{peak} is the number of hits in the 30 ns window around the peak. As described in Section 2.5.2, the SK-IV DAQ records 40 μs of data around each SHE trigger, so all decay electrons in SK-IV are in-gate.

Each candidate decay electron is then run through a time based fitter which searches for a decay vertex minimizing $G_{\vec{x},1}$ defined in Eq. (4.2). Residual time is then defined according to this decay vertex, and the number of hits in a 50 ns residual time window around the candidate is defined as N_{50}. Candidates are chosen as decay electrons if $G_{\vec{x},1} > 0.5$ and $N_{50} > 30$ (16 for SK-II).

During SK I-III, a cabling impedance mismatch resulted in reflections which caused some fake hits around 1 μs after real hits. As a result, in SK I-III the time between 800 and 1200 ns after a primary event cannot be searched for decay electrons. This impedance mismatch was fixed during the electronics upgrade for SK-IV, so this region can be searched in SK-IV, leading to improved decay electron tagging efficiency for SK-IV over SK I-III. The efficiency, as measured by MC, is 80% for μ^+ and 63% for μ^- in SK I-III, and 96% for μ^+ and 80% for μ^- in SK-IV. The reduced efficiency for μ^- is due to μ^- capturing on Hydrogen or Oxygen instead of decaying.

4.8 π^0 Reconstruction

If perfectly reconstructed, a π^0 should be seen as two e-like rings, one for each gamma from the $\pi^0 \to \gamma\gamma$ decay ($\tau = 8.4 \times 10^{-17}$ s). However, sometimes only one e-like ring will be reconstructed, due to one of the gammas being low energy or a significant overlap between the two gammas. The π^0 (`POLFIT`) fitter is applied to all events for which the first ring has a reconstructed energy greater than 30 MeV. It is a likelihood based fitter which adjusts the momentum and angular separation of two gammas to maximize the likelihood of the observed charge distribution.

An additional π^0 fitter is applied to SK-IV events, which is based on the separate reconstruction package fiTQun. This package performs all event reconstruction based on a maximum likelihood method, comparing observed charge and times of hits to those expected for particular event detail. A detailed description of fiTQun can be found in [22].

4.9 Neutron Tagging

When a neutron is produced by an interaction in the SK tank, it thermalizes, and is then captured by an oxygen or hydrogen nucleus. As the cross sections for these capture processes are 0.19 mb and 0.33 b respectively, almost all the neutrons are captured by hydrogen, with a characteristic capture time of $204.8 \pm 0.4 \mu$s [23]. This then results in the emission of a 2.2 MeV γ-ray:

$$n + p \rightarrow d + \gamma \text{ (2.2 MeV)} \tag{4.20}$$

The γ-ray Compton scatters off electrons in the water, accelerating some of them above Cherenkov threshold. Therefore, neutrons can be identified by detecting the Cherenkov light induced by the presence of these 2.2 MeV γ-rays, which each produce about 7 hits in SK. As described in Section 2.5.2, neutron tagging is performed only on SK-IV data, because its $O(100\mu\text{s})$ lifetime requires the long AFT trigger which was introduced with the software trigger of SK-IV.

Neutron tagging is performed as a two-step process. The around 7 Cherenkov photons from an electron Compton scattered by a 2.2 MeV γ are emitted in a very short time period of less than a few nano-seconds. The first step in the neutron tagging process is therefore to search in time for clusters of hit PMTs. These clusters are chosen as candidate neutron captures, and during the second step a neural network is used to differentiate real neutron capture candidates from fake neutron capture candidates. For a detailed description of this algorithm and its development please see [24].

4.9.1 Step One: Initial Neutron Candidate Selection

To search for clusters of hits in time, each hit is first Time-of-Flight corrected based on the reconstructed primary event vertex to give a residual time. A 10 ns sliding window is then used to search for clusters of hits in residual time. If there are seven or more hits in the 10 ns window, the cluster is selected as a neutron candidate. The number of hits in the 10 ns sliding window is defined as N_{10}, and the residual time of the first hit is defined as t_0. If multiple candidates are found with t_0's within 20 ns of each other, only the candidate with the larger N_{10} is considered. This is done to avoid double counting the same neutron capture as multiple candidates. Additionally, if N_{10} is larger than 50 or the number of hits in a 200 ns window around the candidate (N_{200}) is larger than 200, the candidate is rejected as such a large number of hits is likely to be caused by a high energy particles such as a cosmic ray muon passing through the detector. The distributions of N_{10} for signal and background from simulation are shown in Fig. 4.7.

PMT after-pulsing, which occurs between 12 and 18 μs, creates a slight increase in hit rate in the detector as seen in Fig. 4.8, and is not modeled by `SKDETSIM`. The neutron search is therefore begun 18 μs after the primary trigger, in order to avoid after-pulsing. This reduces the coverage of neutron captures from 93% to 84%.

4.9.2 Additional Neutron Reconstructions

Once neutron candidates are selected, two additional reconstruction tools are used to attempt to estimate the location of the neutron capture. The first is a reconstruction tool that has been used for the solar neutrino analyses in SK, called `BONSAI`. `BONSAI` reconstruction uses the timing information of PMT hits in a 1.3 μs time window. It performs an iterative vertex search, with multiple search branches fanning

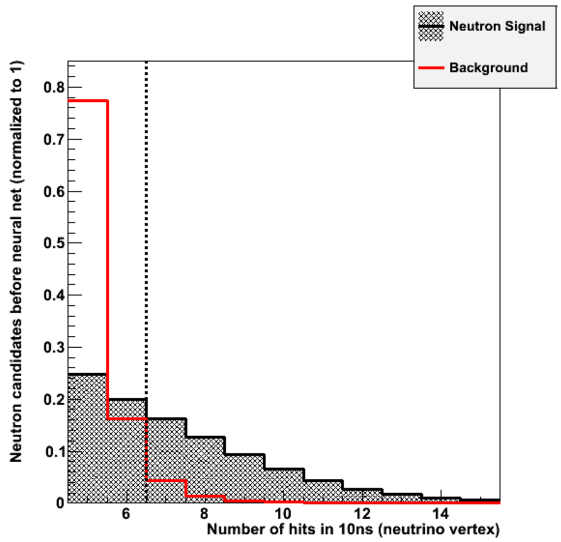

Figure 4.7: Values of N_{10} used to select initial 2.2 MeV candidates. Background increases exponentially as N_{10} threshold is reduced. [24]

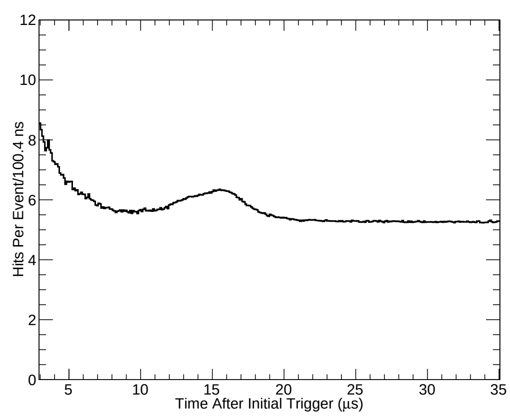

Figure 4.8: Hit rates over the course of an event, taken from the average of all SK4 events. Note the suppressed zero on the x-axis. The falling exponential on the left of the plot is due to decay electrons. The increase due to PMT after-pulsing in the 12 to 18 μs region can be clearly seen. After the PMT after-pulsing the hit rate is very flat and consistent for the rest of the event window.

out from a starting position. Branches are stopped and "pruned" when the goodness of fit for the particular branch drops below a certain level. In this application, the reconstructed primary event vertex is used as the starting point for `BONSAI`.

The second reconstruction tool is called Neut-Fit. Neut-Fit is a simple vertex fitter and uses the timing information of the hits within the 10 ns time window. A shrinking grid search method is used to minimize t_{rms}, defined as

$$t_{rms}(\vec{x}) = \sqrt{\frac{\sum_i^{N_{10}} (t_i - t_{mean})^2}{N_{10}}}, \tag{4.21}$$

where $t_{mean} = \sum_i^{N_{10}} t_i/N_{10}$, and t_i is the hit time after ToF subtraction to vertex $\vec{x}$. The search grid is constricted as the search goes on until the space between points on the grid is 0.5 cm. Neut-Fit is applied twice, first with a constraint that the Neut-Fit vertex must be within 2 m of the primary event vertex. Hits are then TOF corrected to this neutron vertex, and these residual times are used for the calculation of neural net variables described below. Second, Neut-Fit is applied with no constraint beyond the vertex being in the SK tank. This second Neut-Fit vertex is used for variables in the neural net which compare this vertex to the BONSAI and APFit vertices.

4.9.3 Step 2: Final Selection with Neural Network

Following the initial candidate selection, a neural network is used to separate the neutron capture signal from background. Neural networks are a machine learning based tool used in various applications and are especially well suited to pattern recognition problems. They are commonly used as a tool for signal-background classification in particle physics. For this analysis, the ROOT class TMLP is used to implement a feed-forward Multi-Layer Perceptron [25].

A Multi-Layer Perceptron consists of an input layer, output layer, and at least

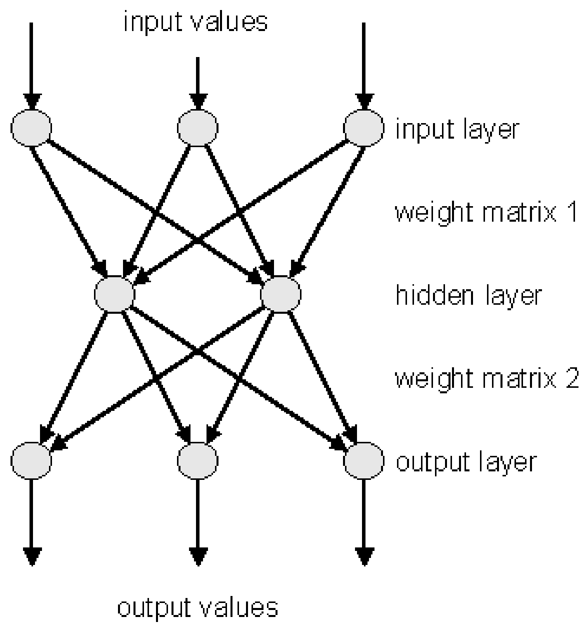

Figure 4.9: Representative structure of a neural network. The circles are neurons, and the lines are synapses. Taken from [26].

one “hidden” layer. Each layer consists of a number of nodes called “neurons”, which are connected to the layers before and after by weighted links called “synapses”. This general structure is shown in Fig. 4.9. At each neuron, the outputs of the previous later, which can be described by the vector $\vec{u}$, are combined into a linear combination $\lambda(\vec{u})$. At hidden layers, the linear combination is fed to an activation function $f(\lambda(\vec{u}))$, which gives the output of the neuron and is passed along to the next layer. In the application to neutron tagging, the sigmoid function is used:

$$f(\lambda(\vec{u})) = \frac{1}{1+e^{\lambda(\vec{u})}}. \tag{4.22}$$

This function can be though as a cut with “gray area”. If $\lambda(\vec{u}) \ll -1$ or $\lambda(\vec{u}) \gg 1$, the sigmoid function returns 0 or 1, respectively. In the region around $\lambda(\vec{u}) = 0$, the sigmoid function transitions smoothly from 0 to 1, with the values of 0 and 1 assigned to the two categorize of events that need to be separated.

Neural networks are trained by feeding them examples for which the correct classification is already known. An optimization technique is then used to adjust the weights in the network to minimize error on the network output. The neutron tagging application uses the Broyden, Fletcher, Goldfar, Shanno (BFGS) method, and the network is trained on 250 years of atmospheric neutrino MC. In the simulation of primary events, uncorrelated PMT dark noise is the only source of background hits simulated by `SKDETSIM`. There are other low energy background sources in the detector, such as radioactive decays from the surrounding rock, radon contamination in the water, and radioactive contaminants in the tank structure, but these backgrounds have no effect on the reconstruction of higher energy particles, so it is unnecessary to properly simulate them for the study of atmospheric neutrinos. However, such low energy backgrounds could mimic the signal of a 2.2 MeV gamma from neutron capture, which produces only around 7 hits in the detector. It is therefore necessary to accurately include these low energy background in the simulation. To do this, about 1.9 million periodic trigger events with gates of 1 ms were recorded in 2009. For each MC event, PMT dark noise was simulated by `SKDETSIM` up to 18 μs. After 18 μs, the simulated dark noise is replaced by real hits from the periodic trigger events. The hits after 18 μs thus come from either simulated neutron captures, or hits from the periodic trigger events. The 900 ns channel dead-time of the SK-IV digitizer is modeled by removing any hit with a previous hit less than 900 ns before it. This hybrid MC technique is shown in Fig. 4.10. The 500 years of MC produced contains about 2.5 million FC events, so some of the periodic trigger events must be shared between two MC events. However, since the periodic trigger window is 1 ms while only 517 μs of periodic trigger hits are needed for each MC event, this sharing is done with an overlap of only 34 μs between MC events which take their background hits from the same periodic trigger event.

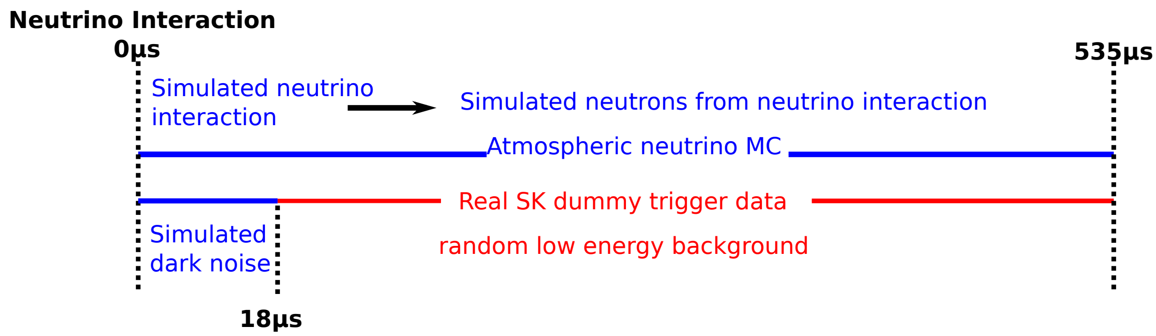

Figure 4.10: Construction of the MC simulation. After 18 μs, dummy trigger data is convoluted with simulated PMT hits from neutron capture events.

In the MC, each neutron candidate is assigned a MC truth as either a true or fake candidate based on the time from t_0 to the nearest true neutron capture. If this time is less than 100 ns, the candidate is labeled as true, if it is greater than 100 ns it is labeled as false. Fig. 4.11 shows the difference in time between each neutron candidate and the nearest true neutron capture in the MC. The flat tail is assumed to represent the background rate of fake candidates, while the excess on top of this flat rate near zero corresponds to true neutron candidates. By extrapolating the stable background rate to continue under the region around zero where the true neutron candidates appear, it is estimated that about 0.4% of neutrons labeled in MC truth as true candidates are in fact fake, while 0.07% of true neutron candidates are labeled in MC truth as fake. Based on MC truth, the simulation indicates an efficiency of 32.7% for the candidate selection with a background rate of 4.4 fake candidates per event.

The neutron tagging neural net has a structure of 16:14:7:1, meaning that there are 16 input variables, two hidden layers with 14 and 7 neurons, respectively, and one output variable. The decision of whether a neutron candidate shall be tagged as a neutron or not is based on a cut on the neural net output. The sixteen input variable are shown in Fig. 4.13, and can be broken into five categories:

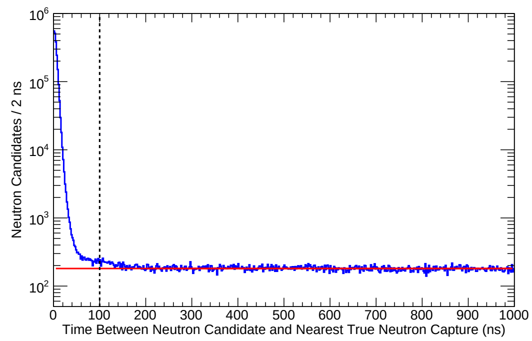

Figure 4.11: Difference in time between neutron candidates and nearest true neutron capture in MC. The flat tail is assumed to be the background candidate event rate, which the spike above the background rate near 0 is due to true neutron candidates. The dotted black line represents the cut dividing true neutron candidates from fake neutron candidates.

- Variables related to the number and locations of hits:
  - $\boldsymbol{N_{10}}$: The variable N_{10} is the maximum number of hits in a 10 ns sliding window around the 2.2 MeV γ-ray candidate.
  - $\boldsymbol{\theta_{mean}}$: The direction of the Compton scattered electron is reconstructed as the vector sum of the directions from the primary neutrino vertex to each hit in the 10 ns window. Opening angles to each hit PMT are then calculated from this direction. The variable θ_{mean} is the average opening angle to the hit PMTs.
  - $\boldsymbol{\phi_{rms}}$: The variable ϕ_{rms} is computed by calculating the azimuthal angle of each hit with respect to the reconstructed direction of the Compton scattered electron. The azimuthal angle between consecutive hits in azimuth are then calculated. The variable ϕ_{rms} is the RMS of these angular differences.
  - $\boldsymbol{N_c}$: The variable N_c is the number of hits in "clusters." Clusters are defined based on the opening angles between hits, viewed from the recon-

structed primary event vertex. Clusters are built starting with a single hit. Hits are then added to the cluster iteratively according to the following rule: if a hit is within 14.1° of any hit in a cluster, it is added to the cluster. The number of clustered hits, N_c is defined as the total number of hits in clusters of 3 or more hits.

– $\boldsymbol{N_{low}}$: The variable N_{low} is the number of "low probability" PMT hits. The probability to detect a photon from a γ-ray for each PMT is defined as follows:

$$A_i = \frac{f(\Theta_i)}{R_i^2} e^{-R_i/L}, \tag{4.23}$$

$$A_{Total} = \sum_i A_i, \tag{4.24}$$

$$P_i = \frac{A_i}{A_{Total}} \tag{4.25}$$

where $f(\Theta_i)$ encodes the angular dependence of the PMT detection efficiency, R_i is the distance from the primary interaction vertex to PMT i, and L is the light attenuation length of the water. In order to define a low probability PMT, a threshold is defined, which depends on the vertex location in the detector as shown in Fig. 4.12. The probability value of each PMT is summed starting from the highest value. The running probability sum is compared with a threshold. When the sum exceeds the threshold, the last PMT added and the remaining PMTs are regarded as low probability PMTs. The threshold is vertex position dependent since the probability can become large if the vertex is close to the wall. In such a case, most of the PMTs are identified as low probability PMTs. The threshold values are set to avoid this situation. N_{low} is then the number of hits in low probability PMTs.

- $\boldsymbol{N_{300}}$: The variable N_{300} is the number of hits in a 300 ns window around the candidate.

- Variables related to the timing of hits:

  - $\boldsymbol{t_{rms}}$: The variable t_{rms} is the root-mean-square of the residual time of the hits in the 10 ns time window.
  - $\boldsymbol{t^3_{rms}}$: The variable t^3_{rms} is the minimum root-mean-square of the residual time of three consecutive hits in the 10 ns time window.
  - $\boldsymbol{t^6_{rms}}$: The variable t^6_{rms} is the same as t^3_{rms}, except for six consecutive hits.

- Variables related to the `BONSAI` fit:

  - $\boldsymbol{E_{Bonsai}}$: The variable E_{Bonsai} is the energy of the candidate reconstructed by Bonsai.
  - $\boldsymbol{d^{wall}_{Bonsai}}$: The variable d^{wall}_{Bonsai} is the distance from the reconstructed Bosai vertex $\vec{x}_{Bonsai}$ to the nearest wall.

- Variables related to Neut-fit:

  - $\boldsymbol{d^{wall}_{Neut-fit}}$: The variable $d^{wall}_{Neut-fit}$ is the distance from the reconstructed Neut-fit vertex $\vec{x}_{Neut-fit}$ to the nearest wall.
  - $\boldsymbol{\Delta N_{10}}$: The variable ΔN_{10} is the difference between N_{10} calculated based on the Neut-fit vertex, and N_{10} calculated based on the primary vertex.
  - $\boldsymbol{\Delta t_{rms}}$: The variable Δt_{rms} is the difference between t_{rms} calculated based on the primary neutrino vertex, and t_{rms} calculated based on the Neut-fit vertex. Note that when t_{rms} is recalculated using the Neut-Fit vertex,

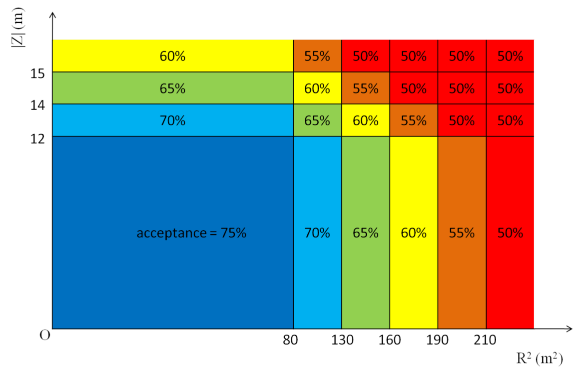

Figure 4.12: The varying acceptance requirements for the N_{low} cut, shown as a function of tank coordinates. [24]

additional hits can be moved into the 10 ns window, which can have the effect of increasing t_{rms}. This means that sometimes Δt_{rms} can be negative.

- Variable related to fit agreement:
  - $|\vec{x}_{Bonsai} - \vec{x}_{Neut-fit}|$: The distance between the Bonsai vertex and the Neut-fit vertex.
  - $|\vec{x}_{primary} - \vec{x}_{Neut-fit}|$: The distance between the Neut-fit vertex and the primary vertex.

The neural net output for both signal and background are shown in Fig. 4.14. The cut value on the neural net output is chosen (rather arbitrarily) to be 0.832; candidates with a neural net output greater than this value are tagged as neutron. Based on MC, this results in a tagging efficiency of 21.7% with a background rate of 0.018 fake neutron tags per primary event, and 97.1% of neutron tags correspond to real neutron captures.

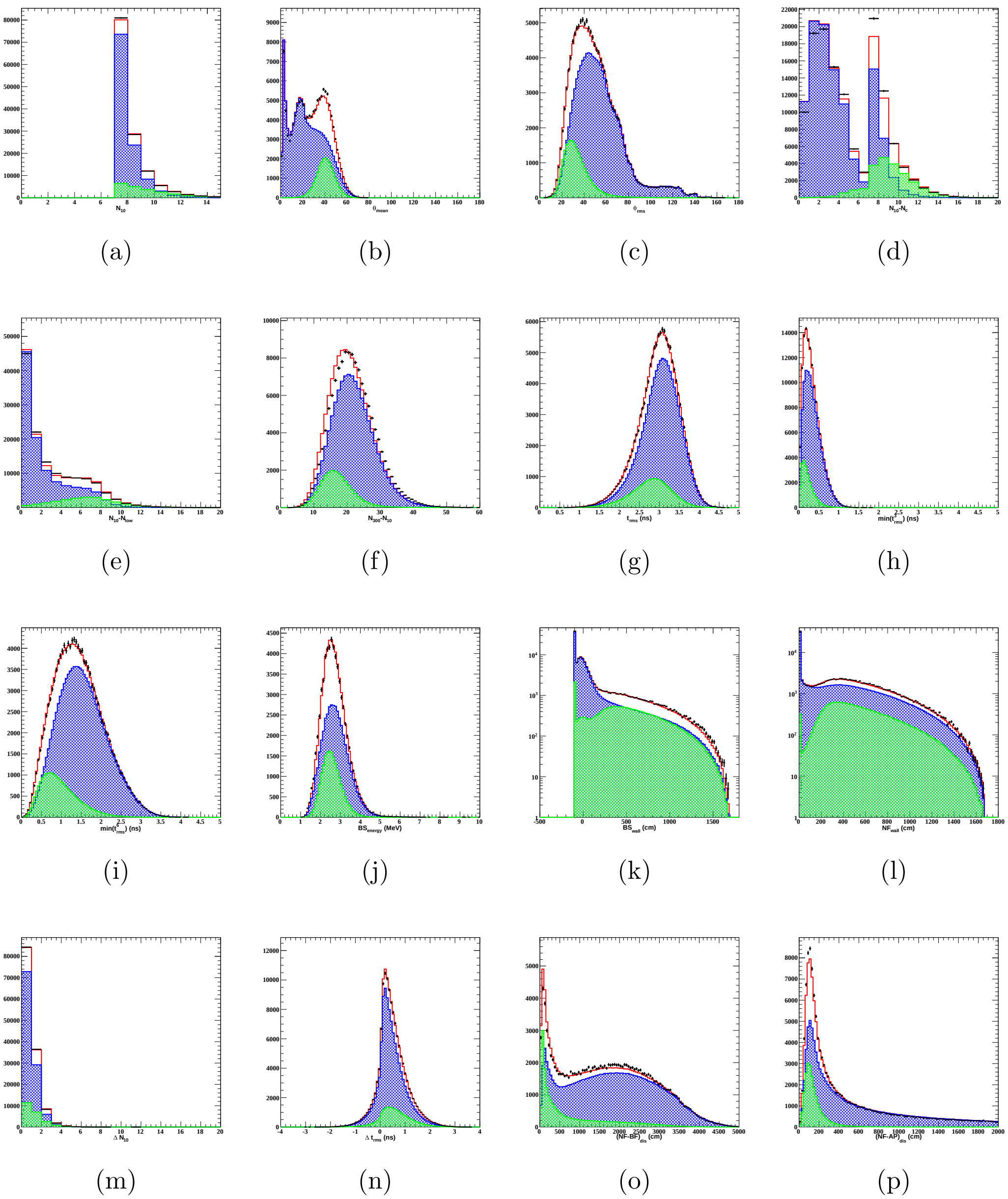

Figure 4.13: Neural network input variables. Signal MC candidates are shown in green, background candidates in blue, and total MC in red. Data is shown in black dots.

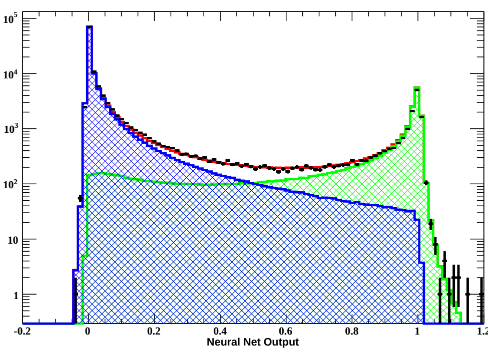

Figure 4.14: Neural network output for signal (green), background (blue), total MC (red) and data (black).

Chapter 5

Atmospheric Neutrino Analysis

Atmospheric neutrinos provide both a rich data set to be studied for understanding neutrino oscillations, and a background to searches for rare processes, such as nucleon decay or dark matter searches. In this chapter, I will discuss the theory and current experimental status of neutrino oscillation and atmospheric neutrino production. I will also present a search for signs of Earth matter effects in atmospheric neutrino oscillations.

5.1 Neutrino Mixing

5.1.1 In Vacuum

Neutrinos mixing is a result of neutrino eigenstates of the weak interaction being different from neutrino mass eigenstates. The flavor eigenstates ν_α are related to the mass eigenstates ν_i by:

$$|\nu_\alpha\rangle = \sum_i^3 U^*_{\alpha,i}|\nu_i\rangle, \tag{5.1}$$

where U is the 3x3 Pontecorvo-Maki-Nakagawa-Sakata (PMNS) matrix [27, 28]

$$\mathbf{U} = \begin{pmatrix} 1 & 0 & 0 \\ 0 & c_{23} & s_{23} \\ 0 & -s_{23} & c_{23} \end{pmatrix} \begin{pmatrix} c_{13} & 0 & s_{13}e^{-i\delta_{CP}} \\ 0 & 1 & 0 \\ -s_{13}e^{i\delta_{CP}} & 0 & c_{13} \end{pmatrix} \times \begin{pmatrix} c_{12} & s_{12} & 0 \\ -s_{12} & c_{12} & 0 \\ 0 & 0 & 1 \end{pmatrix}. \tag{5.2}$$

Here $c_{ij} = \cos\theta_{ij}, s_{ij} = \sin_{\theta_{ij}}$. Propagation of these states according to their vacuum Hamiltonian leads to the standard oscillation formula for relativistic neutrinos in vacuum [13, 29]

$$P(\nu_\alpha \to \nu_\beta) = \delta_{\alpha\beta} - 4\sum_{i>j} \Re(U^*_{\alpha i}U_{\beta i}U_{\alpha j}U^*_{\beta j}) \sin^2\Delta_{ij} \pm 2\sum_{i>j} \Im(U^*_{\alpha i}U_{\beta i}U_{\alpha j}U^*_{\beta j}) \sin 2\Delta_{ij}, \tag{5.3}$$

where

$$\Delta_{ij} = \frac{1.27\Delta m^2_{ij}(\mathrm{eV}^2)L(\mathrm{km})}{E(\mathrm{GeV})},$$

$\Delta m^2_{ij} = m^2_i - m^2_j$ and the sign before the second summation is positive for neutrinos and negative for anti-neutrinos. Neutrino mixing in vacuum is thus fully described by six parameters: the three mixing angles $\theta_{13}, \theta_{12}, \theta_{23}$, the two mass splittings $\Delta m^2_{21}, \Delta m^2_{32}$, and the CP-violating phase δ_{CP}. The sign of θ_{23} is often referred to as the hierarchy, with "normal" implying $\theta_{23} > 0$ and "inverted" implying $\theta_{23} < 0$.

5.1.2 Experimental Status of Parameters

The measurement of neutrino mixing parameters has mainly proceeded from experiments using four types of neutrino sources: atmospheric neutrinos, long-baseline neutrino beams, reactor neutrinos, and solar neutrinos. While other neutrino sources such as geo-neutrinos, astrophysical neutrinos, and neutrinos from short-baseline neutrino beams have been observed and involve very interesting physics, the measurement of the three mixing angle and two mass splitting is based on the four sources mentioned above.

- Atmospheric neutrino experiments are sensitive mainly to θ_{23} and $|\Delta m^2_{32}|$, through the disappearance of upward going muon neutrinos. Super-Kamiokande [30, 31], MINOS [32] and IceCube [33] have performed oscillation analyses and measured $\sin^2\theta_{23} \approx 0.5$ and $|\Delta m^2_{32}|$ between 2×10^{-3} eV^2 and 3×10^{-3} eV^2. The constraints on $\sin^2\theta_{23}$ and $|\Delta m^2_{32}|$ from atmospheric neutrinos are shown along with constraints from long baseline experiments in Fig. 5.1. Atmospheric neutrino oscillations and their (mild) sensitivity to other parameters will be discussed in more detail in Section 5.3.

- Long-baseline neutrino beam experiments, with baselines from 100 km to 1000 km, are sensitive to θ_{23} and $|\Delta m^2_{32}|$ through muon neutrino disappearance, and to θ_{13} through electron neutrino appearance. These muon neutrino beams result from the decay-in-flight of charged pions produced from smashing a proton beam on a target. K2K [34], MINOS [35], T2K [36], and NOνA [37] have all made muon neutrino disappearance measurements of θ_{23} and $|\Delta m^2_{32}|$, which are in good agreement with each other and atmospheric neutrino measurements (see Fig. 5.1). T2K [36] and NOνA [38] also have both observed electron neutrino appearance in their muon neutrino beams, and T2K has used this appearance to make a measurement of $\sin^2\theta_{13} = 0.042^{+0.013}_{-0.021}(fornormalhierarchy)$ which is in agreement with the higher precision measurements of reactor neutrino experiments. OPERA [39], meanwhile, has observed the appearance of electron neutrinos to which muon neutrinos predominately oscillate at a significance of greater than 5σ.

- Reactor neutrino experiments examine the number and spectrum of electron anti-neutrinos produced by nearby nuclear reactors. There are two types of reactor neutrino experiments: those which detect neutrinos predominately from a nearby reactor (or group of reactors) at baselines of about 100 m, and KamLAND, which detected neutrinos from multiple reactors at baselines of about 100 km.

  – The first group of reactor experiments are sensitive to θ_{13} and $|\Delta m^2_{32}|$ through the disappearance of electron anti-neutrinos. Daya Bay [40], RENO [41], and Double Chooz [42] have all made high precision measurements of θ_{13}. Daya Bay's measurement is the most precise, finding a value of $\sin^2\theta_{13} = 0.0214 \pm 0.0013$[40]. Measurements from RENO and Double Chooz are in agreement with Daya Bay, with slightly larger error bars [41, 42]. Measurements of $|\Delta m^2_{32}|$ by RENO and Daya Bay are in agreement with the values found by atmospheric and long baseline experiments.

  – KamLAND [43] has measured electron anti-neutrinos from reactors around Japan, at an effective baseline of 180 km (flux-weighted average). KamLAND is sensitive to Δm^2_{12} and θ_{12} through electron anti-neutrino disappearance, and has measured these parameters to be $\Delta m^2_{21} = 7.58^{+0.21}_{-0.20} \times 10^{-5}$ eV^2 and $\sin^2\theta_{12} = 0.36^{+0.05}_{-0.04}$[43]. The value of $\sin^2\theta_{12}$ is in good agreement with solar neutrino experiments, while there is a mild tension between the value of Δm^2_{12} measured by KamLAND and that measured by solar neutrino experiments.

- Solar neutrino experiments are sensitive to Δm^2_{21} and θ_{12} through measuring a deficit of solar electron neutrinos. SK [44] and SNO [45] have both made measurements of Δm^2_{12} and θ_{12}, and their results are generally consistent with the results from KamLAND, though with a slight tension in the value of Δm^2_{12}. A comparison of the solar neutrino experiments and KamLAND constraints is shown in Fig. 5.2. Note that solar experiments are sensitive to both the magnitude *and sign* of Δm^2_{21}. This sensitivity comes from matter effects in the Sun, which break the degeneracy in the sign of the mass splitting (see Section 5.1.3). In fact, at the about 5-10 MeV energies of solar neutrinos and around 100 g/cm^3 density of the center of the Sun, ν_e is nearly the same as the second energy eigenstate. As electron neutrinos produced by nuclear reactions inside the Sun move outward, the density around them changes very slowly. Therefore, their quantum state evolves adiabatically, meaning that when neutrinos reach the vacuum of space they are very nearly in the ν_2 mass eigenstate. After traveling to the earth, solar neutrino experiments are thus roughly measuring the flavor makeup of this mass eigenstate.

While there has been significant progress in the measurement of neutrino oscillation parameters, there are still a few remaining questions to be answered:

- **What is the mass hierarchy?** The sign of Δm^2_{32} remains unknown. As can be seen in Eq. (5.3), Δm^2_{32} enters into the vacuum oscillation probabilities only in the terms $\sin^2 \Delta_{32}$ and $\sin 2\Delta_{32}$, which are symmetric over a sign flip of Δm^2_{32}. The question of it's sign is often termed the mass hierarchy, with "normal" denoting $m_3 >> m_2 > m_1$, and so $\Delta m^2_{32} > 0$, and "inverted" denoting $m_2 > m_1 >> m_3$, and so $\Delta m^2_{32} < 0$. [1] Some mild sensitivity to hierarchy can appear in vacuum oscillations due to the interference between Δm^2_{32} and Δm^2_{31} terms, but most experiments acquire sensitivity to hierarchy predominately through matter effects. While hints supporting the normal hierarchy have begun to appear around the 1 to 2 σ level in SK atmospheric and T2K and NOνA LBL results, this question will likely require the next generation of neutrino experiments to be completely resolved. The sensitivity of atmospheric neutrinos to the mass hierarchy will be discussed in Section 5.3.

- **What is the value of δ_{CP}?** A non-zero value of $\sin \delta_{CP}$ would be of great interest, as it would be the first experimental evidence of leptonic CP violation, which could help explain the baryon asymmetry of the Universe. Similar to the mass hierarchy situation, a mild preference for non-zero δ_{CP} has begun to emerge from SK atmospheric and T2K and NOνA LBL data, but the final resolution of this question is likely to require next generation experiments.

- **What is the octant of θ_{23}? Is θ_{23} mixing maximal?** The octant of θ_{23} refers to whether $\theta_{23} < \frac{\pi}{4}$ (first octant) or $\theta_{23} > \frac{\pi}{4}$ (second octant). A value of exactly $\theta_{23} = \frac{\pi}{4}$ is called maximal mixing, and would result in the ν_3 mass eigenstate being equal parts ν_μ and ν_τ[2]. T2K, NOνA, and SK are all currently consistent with maximal mixing.

Other as yet unanswered questions in neutrino physics include (but are not limited to):

[1]It is sometimes stated that the term "mass hierarchy" should include a third choice in addition to the two in the text: degenerate, where $m_1 \approx m_2 \approx m_3 \gg |m_3 - m_2|$. The binary choice in the text is then referred to as the "mass ordering". In this thesis, the term mass hierarchy will be used for the binary choice.

[2]This would also be true for the ν_1 and ν_2 mass eigenstates if $\delta_{cp} = 0$.

- **Are neutrinos Dirac or Majorana?** Besides neutrinos, all fermions in the standard model are Dirac particles, meaning that they are distinct from their antiparticle. Neutrinos could Majorana fermions, meaning that they are their own antiparticle[3]. Majorana neutrinos can be searched for by studying the endpoint of the double beta decay electron energy spectrum. A bump at the endpoint of the spectrum would be an indication of neutrinoless double beta decay ($0\nu\beta\beta$) which would mean that neutrinos are Majorana.

- **What is the absolute mass scale of neutrinos?** Although the neutrino mass splittings are well measured, and indicate that at least two of the neutrino mass states must have non-zero mass, the absolute neutrino mass scale is not yet completely pinned down. Study of the H^3 β-decay spectrum has thus far yielded results consistent with $m_\nu = 0$, with and upper limit of $m_\nu < 2.05$ eV at 95% confidence [46], with next generation experiments aiming to reach sensitivities of $m_\nu \sim 0.2$ eV. Cosmological fits to the CMB, supernovae data, and Baryon Acoustic Oscillations data give an upper limit $\sum_j m_j < 0.23$ eV [1].

- **Is there a sterile neutrino?** Measurement of the invisible Z decay width at LEP has shown that there are only 3 neutrino species with mass under half the Z mass which couple to the Z (and can thus participate in the decay $Z \rightarrow \nu\nu$). There could, however, be additional potentially heavy "sterile" neutrinos which do not interact under the weak interaction. Sterile neutrinos which mix with active neutrinos with a mass splitting around 1 eV could explain anomalies

[3] In this thesis, I will often discuss, and even rely on, different behaviors of neutrinos and antineutrinos. Naively, these arguments would appear to be void in the case of a Majorana neutrino. However, all of these arguments in fact rely simply on chirality, left-handed for a neutrino, and right-handed for an anti-neutrino. In the case of a Majorana neutrino, "neutrino" can be thought of as shorthand for "left-handed neutrino", and "antineutrino" as shorthand for "right-handed neutrino".

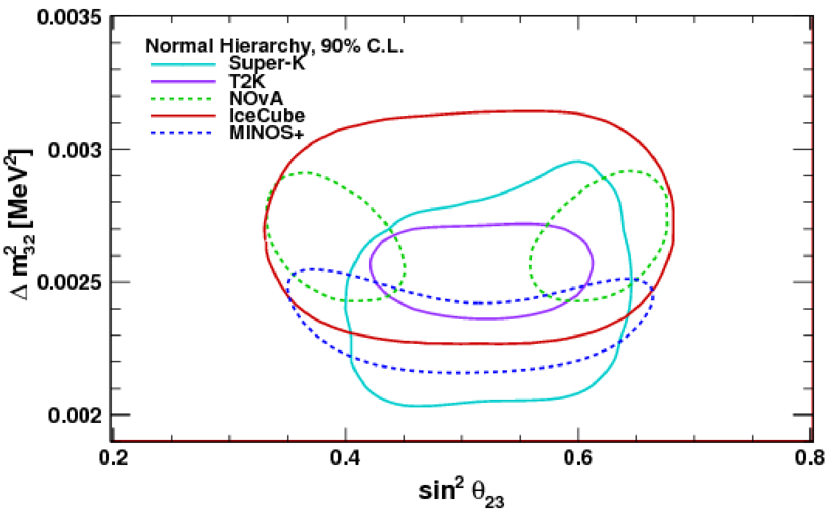

Figure 5.1: 90% C.L. constraints on $\sin^2\theta_{23}$ and Δm^2_{32} from atmospheric and LBL experiments. Taken from [30].

seen in the short-baseline neutrino experiments LSND [47] and MiniBooNE [48]. These anomalies continue to be investigated, and more data will be required to confirm, or rule out, the existence of sterile neutrinos.

5.1.3 In Matter

When neutrinos travel through matter, the effective Hamiltonian is modified from its vacuum form due to the difference in the forward scattering amplitudes of ν_e and $\nu_{\mu,\tau}$ (presented here in the mass eigenstate basis):

$$H_{\text{matter}} = \begin{pmatrix} \frac{m_1^2}{2E} & 0 & 0 \\ 0 & \frac{m_2^2}{2E} & 0 \\ 0 & 0 & \frac{m_3^2}{2E} \end{pmatrix} + U^\dagger \begin{pmatrix} a & 0 & 0 \\ 0 & 0 & 0 \\ 0 & 0 & 0 \end{pmatrix} U, \tag{5.4}$$

where $a = \pm\sqrt{2}G_F N_e$, G_F is the Fermi constant, N_e is the electron density, U is the PMNS matrix, and the plus sign is for neutrinos while the minus sign is for

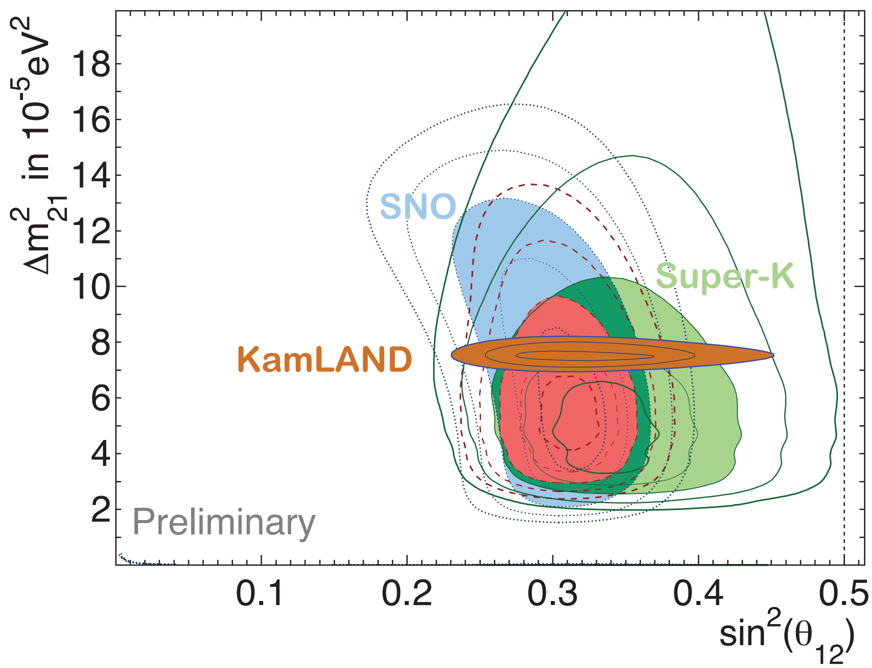

Figure 5.2: Comparison of solar and KamLAND allowed regions. Filled regions give the 3σ confidence levels. The red is a combined fit of SNO and Super-K solar results.

antineutrinos. Following [49], the matrix X, whose row vectors are the propagated mass eigenvectors, can be written as:

$$\mathbf{X} = \sum_k \left[\prod_{j \neq k} \frac{2E\mathbf{H}_{\text{matter}} - M_j^2 \mathbf{I}}{M_k^2 - M_j^2} \right] \exp\left(-i \frac{M_k^2 L}{2E} \right), \tag{5.5}$$

where the $M_i^2/2E$ are the eigenvalues of the constant-density matter Hamiltonian H_{matter}, and $\mathbf{I}$ is the identity matrix. The oscillation probability can then be written as:

$$P(\nu_\alpha \to \nu_\beta) = |(\mathbf{U}\mathbf{X}\mathbf{U}^\dagger)_{\alpha\beta}|^2. \tag{5.6}$$

The eigenvalues were found in [49] (with sign error corrected[4].) to be:

$$M_i^2 = -\frac{2}{3}(\alpha^2 - 3\beta)^{1/2} \cos\left[\frac{1}{3}\arccos\left(\frac{2\alpha^3 - 9\alpha\beta + 27\gamma}{2(\alpha^2 - 3\beta)^{3/2}}\right)\right] + m_1^2 - \alpha/3, \tag{5.7}$$

where

$$\alpha = -2aE + \Delta m_{21}^2 + \Delta m_{31}^2, \tag{5.8}$$

$$\beta = \Delta m_{21}^2 \Delta m_{31}^2 - 2aE[\Delta m_{21}^2(1 - |U_{e2}|^2) + \Delta m_{31}^2(1 - |U_{e3}|^2)], \tag{5.9}$$

$$\gamma = -2aE\Delta m_{21}^2 \Delta m_{31}^2 |U_{e2}|^2. \tag{5.10}$$

The argument $\frac{1}{3}\arccos\left(\frac{2\alpha^3 - 9\alpha\beta + 27\gamma}{2(\alpha^2 - 3\beta)^{3/2}}\right)$ can take an infinite number of distinct values in steps of $2\pi/3$. This means that $\cos\left[\frac{1}{3}\arccos\left(\frac{2\alpha^3 - 9\alpha\beta + 27\gamma}{2(\alpha^2 - 3\beta)^{3/2}}\right)\right]$ can take three different values (one for each value of the argument between $-\pi$ and π. This three values correspond to the three distinct values of M_i^2.

While the above Eqs. (5.5) to (5.7) give an exact solution for the oscillation probability in matter, they are quite opaque. An easier to understand approximation can be found by approximating the matrix $\tilde{U}$ which diagonalizes the matter Hamiltonian (in flavor basis):

$$H_{matter}^{flav} = \tilde{U} \begin{pmatrix} \frac{\lambda_1}{2E} & 0 & 0 \\ 0 & \frac{\lambda_2}{2E} & 0 \\ 0 & 0 & \frac{\lambda_3}{2E} \end{pmatrix} \tilde{U}^\dagger = U \begin{pmatrix} \frac{m_1^2}{2E} & 0 & 0 \\ 0 & \frac{m_2^2}{2E} & 0 \\ 0 & 0 & \frac{m_3^2}{2E} \end{pmatrix} U^\dagger + \begin{pmatrix} a & 0 & 0 \\ 0 & 0 & 0 \\ 0 & 0 & 0 \end{pmatrix}. \tag{5.11}$$

Effective mixing angles $\tilde{\theta}_{23}, \tilde{\theta}_{13}$, and $\tilde{\theta}_{12}$ can then be found from $\tilde{U}$, and effective mass splittings from $\Delta\tilde{m}_{ij}^2 = \lambda_i - \lambda_j$. These effective mixing angles and splittings can

[4]This sign error manifests in the sign of the $2aE$ terms in Eqs (5.8) to (5.10). It is the result of the sign of the matter potential being flipped in Eq. (5) of [49]. This error was corrected by Bethe in [50]

then replace the vacuum mixing angles and splittings in Eq. (5.3) to give oscillation probabilities in matter.

In [51], an analytic approximation is found using the Jacobi method. The resulting effective mixing angles leave θ_{23} and δ unaffected, and give

$$\sin^2 2\tilde{\theta}_{12} \approx \frac{\sin^2 2\theta_{12}}{\sin^2 2\theta_{12} + (\cos 2\theta_{12} \mp aE/\xi_{12})^2}, \tag{5.12}$$

$$\sin^2 \tilde{\theta}_{12} \approx \frac{1}{2} - \frac{\cos 2\theta_{12} \mp aE/\xi_{12}}{2\sqrt{\sin^2 2\theta_{12} + (\cos 2\theta_{12} \mp aE/\xi_{12})^2}}, \tag{5.13}$$

$$\sin^2 2\tilde{\theta}_{13} \approx \frac{\sin^2 2\theta_{13}}{\sin^2 2\theta_{13} + (\cos 2\theta_{13} \mp aE/\xi_{13})^2}, \tag{5.14}$$

$$\sin^2 \tilde{\theta}_{13} \approx \frac{1}{2} - \frac{\cos 2\theta_{13} \mp aE/\xi_{13}}{2\sqrt{\sin^2 2\theta_{13} + (\cos 2\theta_{13} \mp aE/\xi_{13})^2}}, \tag{5.15}$$

where $\xi_{12} = \Delta m^2_{21}/c^2_{13}$ and $\xi_{13} = \Delta m^2_{31} - \Delta m^2_{21} s^2_{12}$, the minus sign is for neutrinos, and the plus sign is for antineutrinos.

The effective mixing angles in matter are shown in Fig. 5.3, where dome interesting behaviors can be observed. First, as a sanity check, when $aE/\xi_{ij} \to 0$, $\sin^2 2\tilde{\theta}_{ij} \to \sin^2 2\theta_{ij}$. At the other extreme, when $|aE/\xi_{ij}| \gg 1$, $\sin^2 \tilde{\theta}_{ij} \to 0$ or 1, depending on the sign of ξ_{ij} and whether neutrino or antineutrinos are being considered. In between these two extremes, when $|aE/\xi_{ij}| \sim \cos 2\theta_{ij}$, a resonance can occur where $\sin^2 2\theta_{ij} \approx 1$. Note that this resonance will occur for either neutrino or antineutrinos, depending on the sign of ξ_{ij}. This will be discussed in relation to the effect of mass hierarchy on amtospheric neutrinos in Section 5.3.

5.2 Atmospheric Neutrino Flux

In this thesis, the main source of neutrinos discussed will be atmospheric neutrinos. When primary cosmic rays, which consist mostly of protons and helium nuclei, collide with nuclei in the Earth's atmosphere, hadronic showers are produced. These

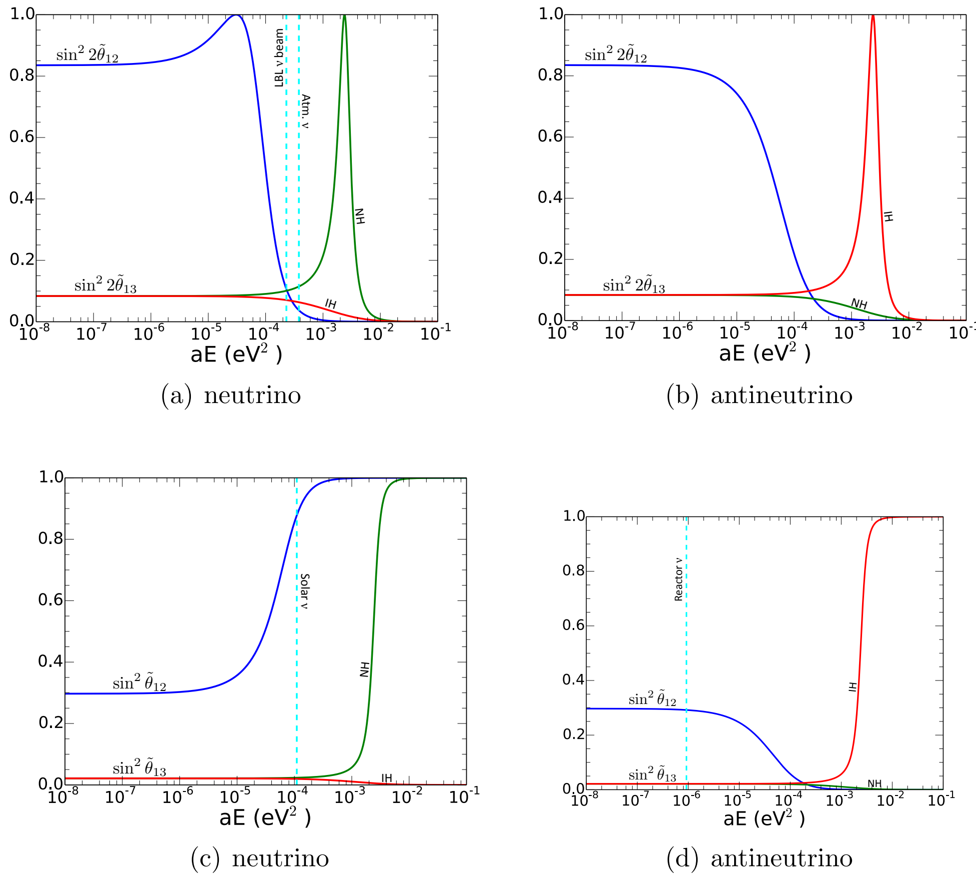

Figure 5.3: Effective mixing angles in matter for neutrinos (left), and antineutrinos (right). Regresentative values of aE are also shown for atmospheric neutrinos in the Earth's mantle ($E_\nu \sim 1$ GeV, $\rho \sim 5$ gm/cm^3), long baseline neutrino beams in the Earth's crust($E_\nu \sim 1$ GeV, $\rho \sim 3$ gm/cm^3), reactor antineutrinos in the Earth's crust ($E_\nu \sim 4$ MeV, $\rho \sim 3$ gm/cm^3), and solar neutrinos in the Sun's core ($E_\nu \sim 10$ MeV, $\rho \sim 150$ gm/cm^3)

hadronic showers consist predominantly of pions, along with some kaons. The decay of charged pions leads to atmospheric neutrinos via

$$\pi^\pm \rightarrow \mu^\pm + \nu_\mu(\bar{\nu}_\mu) \tag{5.16}$$

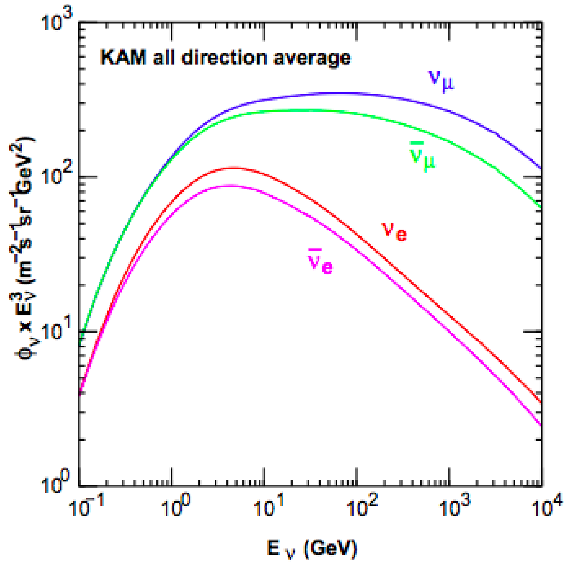

Figure 5.4: Atmospheric neutrino flux as a function of neutrino energy, at Kamioka. [52]

with the muon then decaying to produce additional atmospheric neutrinos through

$$\mu^\pm \to e^\pm + \bar{\nu}_\mu(\nu_\mu) + \nu_e(\bar{\nu}_e). \tag{5.17}$$

From these two processes, we can make a few approximations concerning the atmospheric neutrino flux at energies around 1 GeV and lower.

$$\frac{\phi(\nu_\mu) + \phi(\bar{\nu}_\mu)}{\phi(\nu_e) + \phi(\bar{\nu}_e)} \sim 2 \tag{5.18}$$

$$\frac{\phi(\nu_\mu)}{\phi(\bar{\nu}_\mu)} \sim 1 \tag{5.19}$$

$$\frac{\phi(\nu_e)}{\phi(\bar{\nu}_e)} \sim \frac{\phi(\mu^+)}{\phi(\mu^-)}. \tag{5.20}$$

The atmospheric neutrino flux at Kamioka as a function of neutrino energy is shown in Fig. 5.4.

5.3 Atmospheric Neutrino Oscillations

Atmospheric neutrinos cover a wide range of energies, baselines and matter densities. Neutrino energy ranges from hundreds of MeV to hundreds of TeV, baseline ranges from tens of km (for a neutrino from directly overhead) to over 10,000 km (for a neutrino from the other side of the earth), and matter densities range from basically vacuum (for neutrinos from above) to 13 g/cm^3 for neutrinos passing through the core of the Earth. Oscillograms of atmospheric neutrino oscillations are shown in Fig. 5.5.

A few regions of interest are visible in these oscillograms. First, note that for neutrinos coming from above the horizon ($\cos\theta_z > 0$), $\sin^2\Delta_{21} \ll 1, \sin^2\Delta_{31} \approx \sin^2\Delta_{32}$ and so we have the approximations:

$$\text{(For } \cos\theta_z > 0)$$

$$P(\nu_e \to \nu_e) \cong 1 - \sin^2 2\theta_{13} \sin^2\left(\frac{1.27\Delta m^2_{31}L}{E}\right) \tag{5.21}$$

$$P(\nu_\mu \to \nu_\mu) \cong 1 - 4\cos^2\theta_{13}\sin^2\theta_{23}(1-\cos^2\theta_{13}\sin^2\theta_{23})\sin^2\left(\frac{1.27\Delta m^2_{31}L}{E}\right) \tag{5.22}$$

$$P(\nu_\mu \leftrightarrow \nu_e) \cong \sin^2\theta_{23}\sin^2 2\theta_{31}\sin^2\left(\frac{1.27\Delta m^2_{13}L}{E}\right). \tag{5.23}$$

Since θ_{13} is small, we can also make the approximations that $\sin^2\theta_{13} \approx 0$ and $\cos^2\theta_{13} \approx 1$, giving:

$$\text{(For } \cos\theta_z > 0)$$

$$P(\nu_e \to \nu_e) \cong 1 \tag{5.24}$$

$$P(\nu_\mu \to \nu_\mu) \cong 1 - \sin^2 2\theta_{23}\sin^2\left(\frac{1.27\Delta m^2_{31}L}{E}\right) \tag{5.25}$$

$$P(\nu_\mu \leftrightarrow \nu_e) \cong 0, \tag{5.26}$$

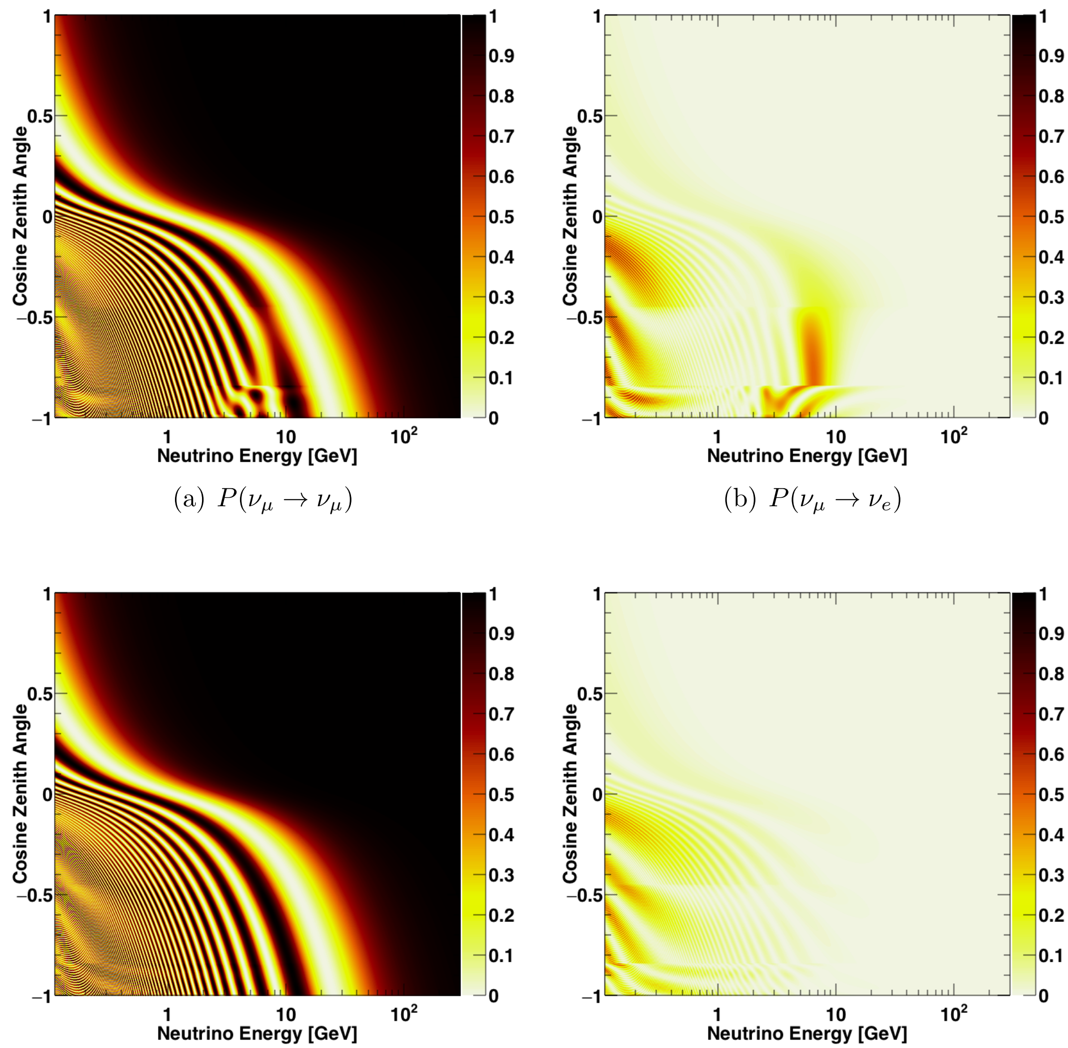

(a) $P(\nu_\mu \to \nu_\mu)$ (b) $P(\nu_\mu \to \nu_e)$

(c) $P(\bar{\nu}_\mu \to \bar{\nu}_\mu)$ (d) $P(\bar{\nu}_\mu \to \bar{\nu}_e)$

Figure 5.5: Oscillation probabilities for neutrinos (upper panels) and antineutrinos (lower panels) as a function of energy and zenith angle assuming a normal mass hierarchy. Matter effects in the Earth produce the distortions in the neutrino figures between 2 and 10 GeV, which are not present in the antineutrino figures. For an inverted hierarchy the matter effects appear in the antineutrino figures. Here the oscillation parameters are taken to be $\Delta m^2_{32} = 2.5\times10^{-3}\text{eV}^2$, $\sin^2\theta_{23} = 0.5$, $\sin^2\theta_{13} = 0.0219$, and $\delta_{CP} = 0$.

indicating no oscillation of ν_e, and oscillation of ν_μ only to ν_τ, with the maximum oscillation probability controlled by the value of θ_{23}. However, for $\cos\theta_z > 0.25$ with $E_\nu > 1$ GeV, or $\cos\theta_z > 0$ with $E_\nu > 10$ GeV, we can make the additional approximation that $\sin^2\Delta_{31} \approx \sin^2\Delta_{32} \ll 1$, and so there is no oscillation of neutrinos observed. Coupled with the reduced correlation between lepton and neutrino directions at energies below 1 GeV (often this is described as a lack of "pointing"), this means that downward going atmospheric neutrinos generally provide information on the normalization of the neutrino flux, not precise information on the values of the neutrino mixing parameters.

Next, we can consider neutrinos from below the horizon ($\cos\theta_z < 1$). For neutrinos below about 400 MeV, both Δ_{21} and Δ_{31} oscillations contribute, as can be seen in Fig. 5.5. However, because of the lack of pointing at these energies, these effects are averaged out, and are thus very difficult to observe in atmospheric neutrino data. For energies above about 400 MeV but below about 6 GeV, Δ_{21} oscillations are mostly suppressed due to matter effects. In this regime, matter effects combined with small θ_{13} lead to $\nu_e \approx \tilde{\nu}_2$ for neutrinos, and $\nu_e \approx \tilde{\nu}_1$ for antineutrinos. This can be understood be realizing that in this regime $aE \gg \delta m^2_{21}, aE \ll \delta m^2_{31}$, so that the matter effect part of the Hamiltonian dominates the δm^2_{21} part of the Hamiltonian, but is not yet comparable to the δm^2_{31} part. This effectively uncouples the electron neutrino flavor and one of the neutrino mass states from the oscillation, and leads to neutrino oscillation being approximately a two flavor situation in this regime. In this regime then, the approximate oscillation probabilities are:

$$\text{(For } \cos\theta_z < 0, 400 \text{ MeV-600 MeV)}$$

$$P(\nu_e \to \nu_e) \cong 1 \tag{5.27}$$

$$P(\nu_\mu \to \nu_\mu) \cong 1 - \sin^2 2\theta_{23} \sin^2 \left(\frac{1.27 \Delta m^2_{31} L}{E} \right) \tag{5.28}$$

$$P(\nu_\mu \leftrightarrow \nu_e) \cong 0, \tag{5.29}$$

At around 6 to 10 GeV, for neutrinos in the normal hiearchy and antineutrinos in the inverted hierarchy, $aE \approx \Delta m^2_{31}$, and we have $\sin^2 \tilde{\theta}_{13} \approx \cos^2 \tilde{\theta}_{13} \approx 0.5$. There is thus a resonance, where $\nu_\mu \leftrightarrow \nu_e$ oscillation is fairly significant, as seen in Fig. 5.5. It is important to note that this resonance will occur for either neutrinos (in the case of the normal hierarchy) or antineutrinos (in the case of the inverted hierarchy), but not both. Thus a determination of the neutrino hierarchy can be made by differentiating between a resonance in neutrinos and antineutrinos.

Above 10 GeV, ν_e becomes nearly exactly the highest energy eigenstate for neutrinos, and lowest energy eigenstate for antineutrinos, as the matter potential becomes much larger than either mass splitting. The electron neutrino flavor is again uncoupled from neutrino mixing, and the oscillation becomes a two flavor situation in this regime, leading to the same approximate oscillation probabilities as Eq. (5.29):

$$\text{(For } \cos\theta_z < 0, > 10 \text{ GeV)}$$

$$P(\nu_e \to \nu_e) \cong 1 \tag{5.30}$$

$$P(\nu_\mu \to \nu_\mu) \cong 1 - \sin^2 2\theta_{23} \sin^2 \left(\frac{1.27 \Delta m^2_{31} L}{E} \right) \tag{5.31}$$

$$P(\nu_\mu \leftrightarrow \nu_e) \cong 0. \tag{5.32}$$

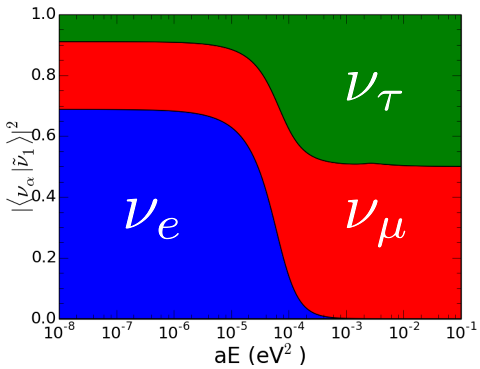

(a) $\tilde{\nu}_1$

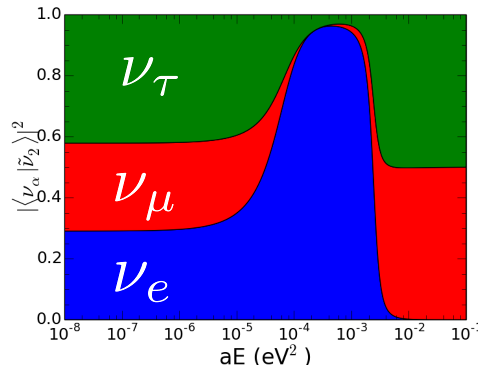

(b) $\tilde{\nu}_2$

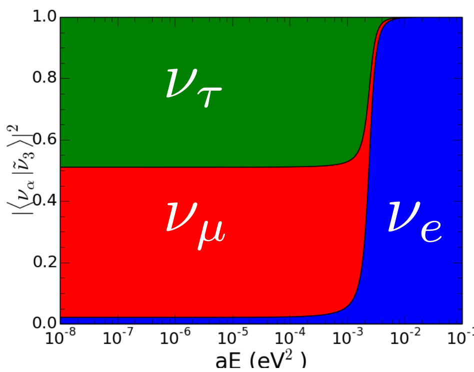

(c) $\tilde{\nu}_3$

Figure 5.6: Flavor composition of neutrino Hamiltonian eigenstates as a function of matter potential. This is for neutrinos in the normal hierarchy.

This progression of oscillation behavior can be understood through Fig. 5.6, which demonstrates the progression from three-flavor, to two-flavor, back to three-flavor, and finally to two-flavor mixing, as energy increases.

The above approximations illustrate the sensitivities of SK atmospheric neutrino analyses to different oscillation parameters. The dominant sensitivity is to θ_{23} and Δm^2_{31} through ν_μ disappearance. There is additional secondary sensitivity to θ_{13} and the mass hierarchy through the resonance in $\nu_e \leftrightarrow \nu_\mu$ oscillations.

5.4 Atmospheric Neutrino Simulation

In order to compare data to theoretical expectations, 500 year atmospheric neutrino monte-carlo samples are produced for each SK period. Atmospheric neutrino simulation begins with the unoscillated atmospheric neutrino flux. We use the atmospheric neutrino flux calculated by Honda et al. [52]. This flux is calculated by simulation of the primary cosmic ray flux interacting in the Earth's atmosphere. The primary cosmic ray flux is assumed to be isotropic, with a spectrum of the form

$$\phi(E_k) = K \times \left[E_k + b\exp(-c\sqrt{E_k})\right]^{-a}, \tag{5.33}$$

with the parameters K, b, c, a found by fitting to primary cosmic ray data. The cosmic rays are propagated through the Earth's atmosphere using the hadronic interaction models DPMJET-III and JAM above and below 32 GeV, respectively. These models are tuned to match the atmospheric muon fluxes measured at balloon altitudes. The Earth's magnetic field is accounted for by propagating the primary cosmic ray backwards in time through the Earth's magnetic field to ensure that it would pass the geomagnetic cutoff.

The interaction of the atmospheric neutrino flux with the water in the SK detector is simulated using the neutrino interaction simulation package NEUT. NEUT simulates both charged current (CC) and neutral current (NC) neutrino interactions, and simulates final state interactions within the nucleus before passing the resulting particles on to detector simulations. The CC cross section consists primarily of a few main components, which are shown along with the total CC cross section in Fig. 5.7: charged-current quasi-elastic, charged-current pion production, charged-current meson exchange current, and charged-current deep inelastic scattering.

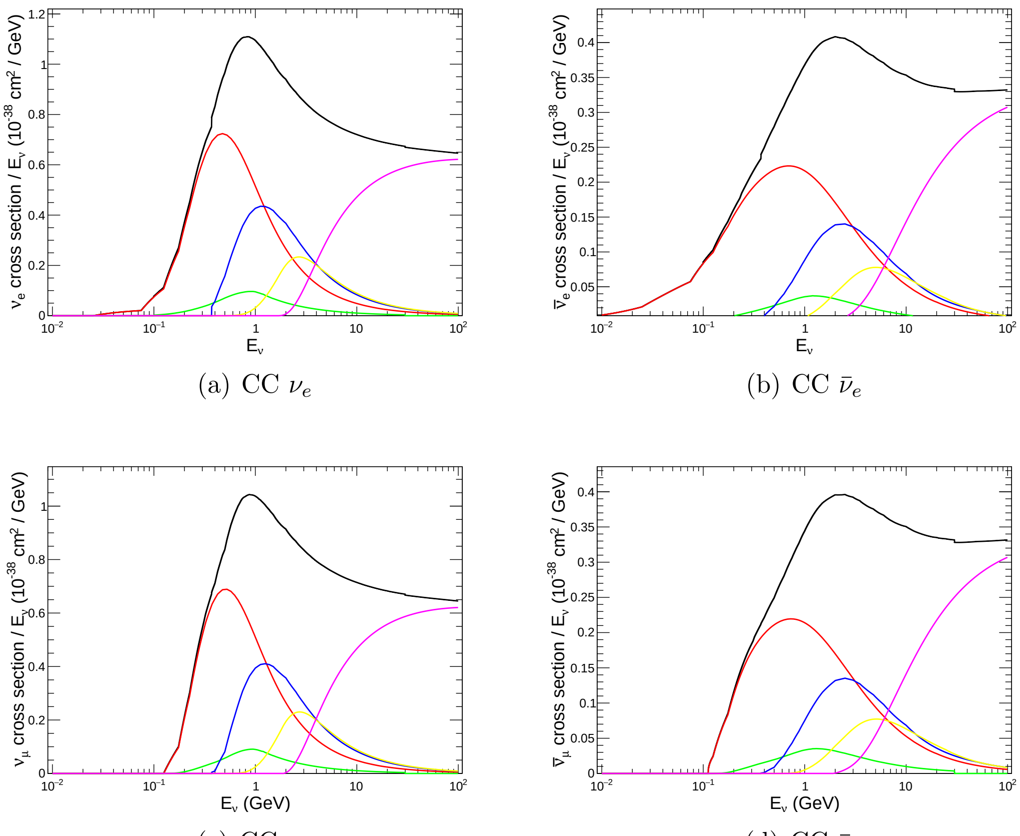

(a) CC ν_e (b) CC $\bar{\nu}_e$

(c) CC ν_μ (d) CC $\bar{\nu}_\mu$

Figure 5.7: Charged current neutrino cross sections used in NEUT (per nucleon). Black is total cross section, red is Quasi-Elastic, green is Meson Exchange Current, blue is Single Pion, yellow is Multi Pion, and purple is Deep Inelastic Scattering.

5.4.1 Charged-Current Quasi-Elastic

Charged-Current Quasi-Elastic (CCQE) scattering refers to the scattering of a neutrino off of a single nucleon (either free or in the nucleus) through the exchange of a $W^\pm$ boson, in a reaction such as:

$$\nu_e + n \rightarrow e^- + p. \tag{5.34}$$

When the nucleon is a bound nucleon from the Oxygen nucleus, a Fermi gas model is used for the distibution of nucleon momenta, with the Fermi level set at 225 MeV. CCQE is the dominant CC interaction mode below about 1 GeV.

5.4.2 Charged-Current Resonant Single Pion Production

Charged-Current Resonant Single Pion Production (CC1π) becomes the dominant CC interaction mode at around 1 GeV. The neutrino excites the nucleon to an excited state, which then quickly decays ($\tau \sim 10^{-24}$) to a pion and ground state nucleon. A common example involves excitation to a Δ resonance, such as:

$$\begin{aligned} \nu_e + p \rightarrow e^- + &\Delta^{++} \\ &\Delta^{++} \rightarrow p + \pi^+. \end{aligned} \tag{5.35}$$

The Rein and Sehgal model [53–55] is used to simulate these interactions, and the final state nucleon is required to have momentum greater than the Fermi level to account for Pauli blocking.

5.4.3 Charged-Current Deep Inelastic Scattering

At around 10 GeV, Charged-Current Deep Inelastic Scattering (CCDIS) becomes the dominant CC interaction mode. In a DIS interaction, the incoming neutrino resolves and scatters off an individual quark in the target nucleon, resulting in a hadronic final state:

$$\nu_e + n \rightarrow e^- + X, \tag{5.36}$$

where X represents the collection of resulting hadrons. Once it has fully turned on, the DIS cross section scales linearly with energy up to a few TeV, as $M_W^2 \gg q^2$.

5.4.4 Detector Simulation

Once the final state particles are produces by NEUT, they are passed to a dedicated GEANT3 based detector simulation software called SKDETSIM. SKDETSIM simulates the propagation of final state particles through the detector, production of Cherenkov light, and PMT and electronics response to light. Hadrons are simulated by the GEANT3 interface with the package CALOR [56], which uses FLUKA (GFLUKA) for hadrons above 10 GeV, HETC for hadrons below 10 GeV, and MICAP for neutrons below 20 MeV. The low energy cutoff for neutral hadrons is set to 10^{-5} eV so that neutrons continue to be simulated until they capture. Uncorrelated PMT dark noise hits are simulated out to 18 μs, after which real hits from periodic data triggers are used to account for background hits, as explained in Section 4.9.3. The output of SKDETSIM gives raw simulated hit patterns, which are run through the event selections and reconstructions described in Chapters 3 and 4 to produce an atmospheric neutrino MC which can be compared to the observed atmospheric neutrino data.

5.5 Matter Effects Analysis

SK measures atmospheric neutrino parameters using a binned likelihood fit comparing atmospheric neutrino data to MC. In this section I will describe the procedure of this fit, along with the results of a search for signs of Earth matter effects in atmospheric neutrino data using this fitting procedure.

5.5.1 SK Three-Flavor Fitting Procedure

Data and MC events that are selected by the FC, PC, and UPMU selections are further categorized into 19 analysis samples according to some of their reconstructed properties. Each analysis sample is then binned according to zenith angle and either visible energy, e-like, μ-like, or π^0-like momentum, resulting in 520 analysis bins. The specifics of the analysis samples and binning are shown in Table 5.1.

Both data and MC events are separated into the 520 analysis bins. MC events are reweighted to account for neutrino oscillations according to the values of the oscillation parameters being tested and the MC truth associated with the event with weights defined as

$$w_{\nu_\alpha} = \frac{\phi_{\nu_e} P_{\nu_e \to \nu_\alpha} + \phi_{\nu_\mu} P_{\nu_\mu \to \nu_\alpha}}{\phi_{\nu_\alpha}}, \tag{5.37}$$

where ν_α is true neutrino flavor, ϕ_{ν_α} gives the unoscillated neutrino flux for flavor α, which is a function of energy and direction, and $P_{\nu_\beta \to \nu_\gamma}$ gives the oscillation probability for a neutrino starting as flavor β to interact in the detector as flavor γ, which is a function of the energy and direction of the neutrino, as well as the values of the oscillation parameters being tested.

For the calculation of the the oscillation probability of a neutrino traversing the Earth, the Earth's atmosphere is modeled as vacuum, and the Earth as a sphere of radius 6371 km, with a spherical density profile which is a simplified version of the preliminary reference Earth model (PREM) [57], as shown in Table 5.2. For a neutrino with energy E produced at a height h above the surface of the Earth, the path from our detector to the neutrino production location is traced through N steps across the atmosphere and different regions of the Earth's interior (Figure 5.8). Note that because the Earth is modeled as spherically symmetric, this path is a function of only the production height and zenith angle; it is independent of azimuthal angle.

Sample	Energy bins	$\cos\theta_z$ bins
Fully Contained (FC) Sub-GeV		
e-like, Single-ring		
0 decay-e	5 $e^{\pm}$ momentum	10 in $[-1, 1]$
1 decay-e	5 $e^{\pm}$ momentum	
μ-like, Single-ring		
0 decay-e	5 $\mu^{\pm}$ momentum	10 in $[-1, 1]$
1 decay-e	5 $\mu^{\pm}$ momentum	10 in $[-1, 1]$
2 decay-e	5 $\mu^{\pm}$ momentum	
π^0-like		
Single-ring	5 $e^{\pm}$ momentum	
Two-ring	5 π^0 momentum	
Fully Contained (FC) Multi-GeV		
Single-ring		
ν_e-like	4 $e^{\pm}$ momentum	10 in $[-1, 1]$
$\overline{\nu}_e$-like	4 $e^{\pm}$ momentum	10 in $[-1, 1]$
μ-like	2 $\mu^{\pm}$ momentum	10 in $[-1, 1]$
Multi-ring		
ν_e-like	3 visible energy	10 in $[-1, 1]$
$\overline{\nu}_e$-like	3 visible energy	10 in $[-1, 1]$
μ-like	4 visible energy	10 in $[-1, 1]$
Other	4 visible energy	10 in $[-1, 1]$
Partially Contained (PC)		
Stopping	2 visible energy	10 in $[-1, 1]$
Through-going	4 visible energy	10 in $[-1, 1]$
Upward-going Muons (Up-μ)		
Stopping	3 visible energy	10 in $[-1, 0]$
Through-going		
Non-showering		10 in $[-1, 0]$
Showering		10 in $[-1, 0]$

Table 5.1: The 19 analysis samples and their binnings. Sub-GeV multi-ring interactions are not used in the present analysis. [30]

Region	R_{min} (km)	R_{max} (km)	density (g/cm^3)
inner core	0	1220	13.0
outer core	1220	3480	11.3
mantle	3480	5791	5.0
crust	5701	6371	3.3

Table 5.2: Model of the Earth used in the analysis, a simplified version of the PREM.

The oscillation probability for a given neutrino is calculated by stepping along its path:

$$P_{\nu_\alpha \to \nu_\beta}(E, h, \cos\theta_{\mathrm{zenith}}) = |(\mathbf{U} \prod_i^N \mathbf{X}(L_i, \rho_i, E)\mathbf{U}^\dagger)_{\alpha\beta}|^2, \tag{5.38}$$

where L_i and ρ_i are the length and density of the i^{th} step along the neutrino's path, and $\mathbf{U}$ is the PMNS matrix defined in Eq. (5.2) and $\mathbf{X}$ is the propagation matrix defined in Eq. (5.5).

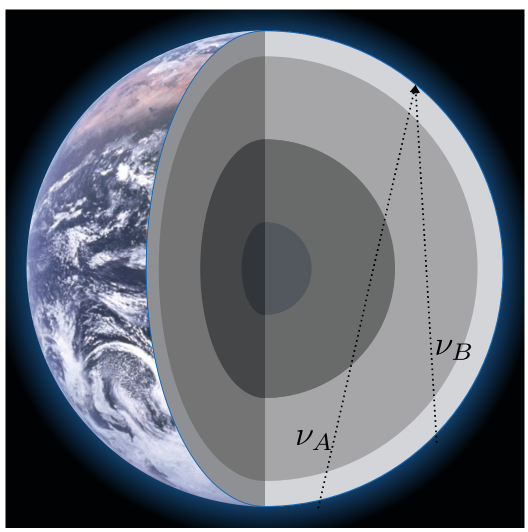

Figure 5.8: The propagation of two neutrinos through the simplified model of the Earth used in the analysis below. Both ν_A and ν_B are produced in the atmosphere. ν_A then experiences 6 oscillation steps (air $\to$ crust $\to$ mantle $\to$ outer core $\to$ mantle $\to$ crust), while ν_B experiences 4 oscillation steps (air $\to$ crust $\to$ mantle $\to$ crust).

The data is fit to the MC using a binned χ^2 method, and accounts for 155 systemtic uncertainties using the pull-method. The Poisson χ^2 is defined as:

$$\chi^2 = 2\sum_n \left(E_n - \mathcal{O}_n + \mathcal{O}_n \ln \frac{\mathcal{O}_n}{E_n} \right) + \sum_i \left(\frac{\epsilon_i}{\sigma_i} \right)^2, \tag{5.39}$$

with,

$$E_n = \sum_j E_{n,j}(1 + \sum_i f^i_{n,j}\epsilon_i), \tag{5.40}$$

$$\mathcal{O}_n = \sum_j \mathcal{O}_{n,j}. \tag{5.41}$$

Here $E_{n,j}$ is the MC expectation in the n^{th} analysis bin for the j^{th} SK period, $\mathcal{O}_{n,j}$ is the corresponding data in that bin and $f^i_{n,j}$ is a coefficient describing the fractional change in the bin's MC under a $1\sigma_i$ variation of the the i^{th} systematic uncertainty. The system is solved for the values of ϵ_i which minimize χ^2, thus giving the best agreement between Data and MC allowed by the systematic uncertainties. A grid of points in oscillation parameter space is tested, and the point with the minimum value of χ^2 is the best fit point. The amount that other points in oscillation parameter space are disfavored is defined by the $\Delta\chi^2$ which is the difference between the χ^2 measured at a particular point and that measured at the best fit point.

Since the SK atmospheric neutrino data has minimal sensitivity to Δm^2_{21}, θ_{12} and θ_{13} compared to other data sets and experiments, in this analysis the values of these parameters are fixed to $\Delta m^2_{21} = (7.5 \pm 0.18) \times 10^{-5}$ eV^2, $\sin^2\theta_{12} = 0.304 \pm 0.014$, and $\sin^2\theta_{13} = 0.0219 \pm 0.0012$, with their uncertainties included as systematic uncertainties. The current best fit values (with $1-\sigma$ ranges) of these parameters from the SK atmospheric fit are, for the normal hierarchy, $\sin^2\theta_{23} = 0.588^{+0.031}_{-0.067}$, $|\Delta m^2_{32}| = 2.50^{+0.13}_{-0.20}$, $\delta_{CP} = 4.19^{+1.37}_{-1.59}$, and for the inverted hierarchy, $\sin^2\theta_{23} = 0.575^{+0.035}_{-0.0685}$, $|\Delta m^2_{31}| = 2.50^{+0.08}_{-0.37}$, $\delta_{CP} = 4.19^{+1.49}_{-1.63}$. The normal hierarchy is favored over the inverted hierarchy by a $\Delta\chi^2$ of 3.89 [30].

5.5.2 Seeking Earth Matter Effects

As discussed in Section 5.3, the sensitivity of atmospheric neutrinos to the mass hierarchy comes from the observation of a $\nu_\mu \leftrightarrow \nu_e$ resonance due to Earth matter effects in either neutrinos or antineutrinos. Therefore, observation of Earth matter effects on atmospheric neutrinos is an important step on the quest to determine the neutrino mass hierarchy. While matter effects have been observed in the Sun [58, 59], and Earth matter effects have been observed on Solar neutrinos through the day-night asymmetry [60], there has thus far been no experimental observation of Earth matter effects in atmospheric neutrinos [5].

The fit described in Section 5.5.1 can be modified to search for Earth matter effects by introducing an additional free parameter α which scales the matter potential a in Eq. (5.4). The parameter α can be understood as continuously turning matter effects on or off, with $\alpha = 0$ corresponding to vacuum oscillations, $\alpha = 1$ corresponding to the standard matter effects, and $\alpha = 2$ corresponding to matter effects with a matter potential twice as strong as expected. The fitting procedure proceeds identically to that described in Section 5.5.1, except that in the calculation of oscillation probabilities a is replaced by αa in Sections 5.1.3 to 5.1.3 in order to account for the effect of α.

Figure 5.9 compares vacuum oscillation probabilities to those with matter effects included. As can be seen, matter effects lead to a resonance in $\nu_\mu \to \nu_e$ oscillations for neutrinos passing through the Earth's mantle at around 5 to 10 GeV, which is the dominant way in which atmospheric neutrinos are sensitive to matter effects. There

[5]The only previous experimental statement about Earth matter effects on atmospheric neutrinos is Ice Cube's report at Neutrino 2014 that their atmospheric neutrino data favors standard matter over vacuum oscillations by 1 unit of $\Delta\chi^2$.

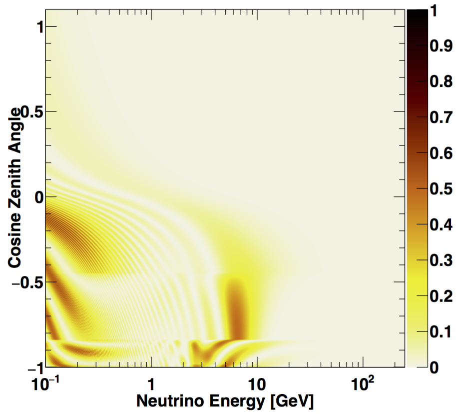

(a) Matter $\nu_\mu \rightarrow \nu_e$

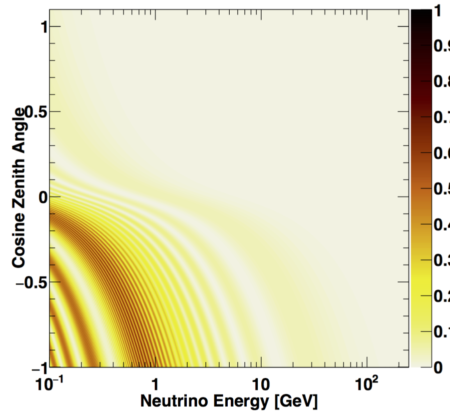

(b) Vacuum $\nu_\mu \rightarrow \nu_e$

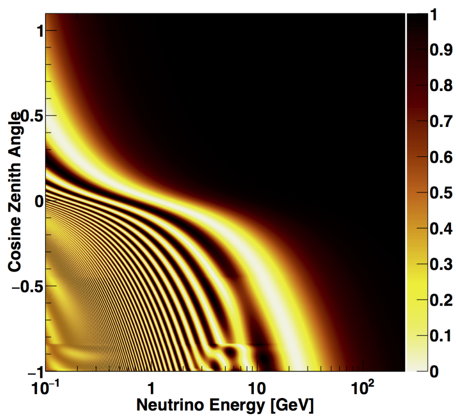

(c) Matter $\nu_\mu \rightarrow \nu_\mu$

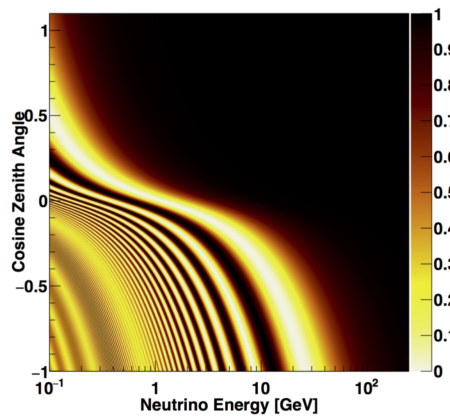

(d) Vacuum $\nu_\mu \rightarrow \nu_\mu$

Figure 5.9: Oscilligrams for neutrinos assuming normal hierarchy comparing matter oscillations to vacuum oscillations.

is additional sensitivity through suppression of $\nu_\mu \rightarrow \nu_e$ oscillations at energies above and just below the resonance region.

The result of the fit is shown in Fig. 5.10 along with the expected sensitivity [30]. The best fit point occurs at $\alpha = 1.1$, and $\alpha = 1$ agrees with the data nearly as well as the best fit point. Vacuum oscillations are disfavored with a $\Delta\chi^2$ of 5.2, with an expected sensitivity of $\Delta\chi^2$=7.8. The preference of each data sample is shown in Fig. 5.11. The preference for standard matter effects is strongest in the "Multi-GeV

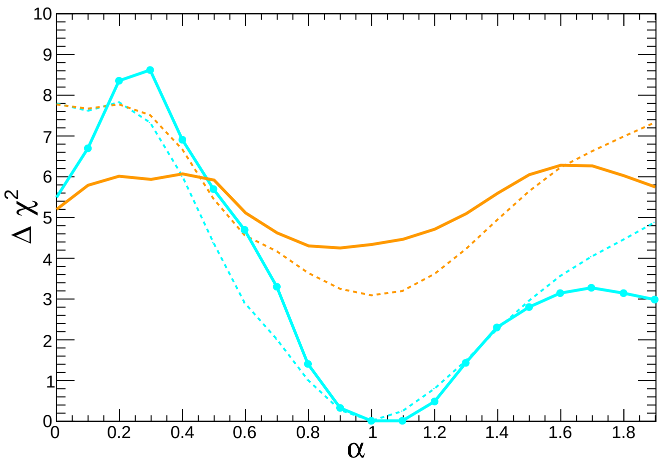

Figure 5.10: Fit result of Matter Effects analysis in solid lines, along with expected sensitivity (assuming normal hierarchy) in dashed lines. Orange is for the inverted hierarchy fit and cyan is the normal hierarchy fit.

e-like, neutrino-like" sample. The data and MC expectation at best fit vacuum and standard matter points for this sample are shown in Fig. 5.12. The preference comes from an excess of upward going events in the 2.5 GeV-10 GeV region, as expected from the matter effect resonance.

While Wilks' theorem can be used to estimate the significance of the exclusion of vacuum oscillations as $\sqrt{5.2} = 2.3\sigma$, the fact that α is bounded at the point of interest ($\alpha = 0$) as well as the treatment of systematic errors means the application of Wilks' theorem is imperfect. The find a better estimate for the significance of the exclusion, 10,000 toy MC were produced assuming that the best fit vacuum point was the truth. For each toy MC productions, systematics were fluctuated to find an adjusted MC expectation for each bin, and the number of events in each bin was then chosen as a Poisson process. This toy MC "data" was then fit, and the $\Delta\chi^2_{vac}$ value was compared to the measured value of $\Delta\chi^2_{vac} = 5.2$. Eighty-nine percent of toy MC productions resulted in a $\Delta\chi^2_{vac}$ smaller than the value measured in the data. This indicates that our data excludes vacuum oscillations at a significance of 1.6σ, slightly

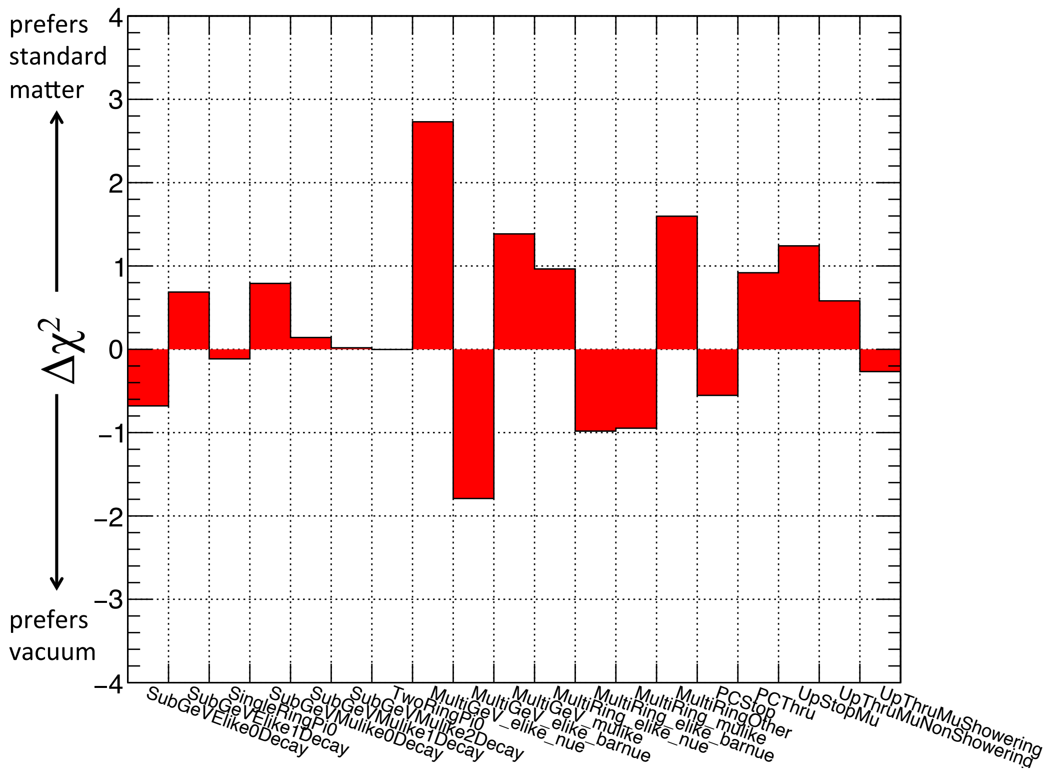

Figure 5.11: Preference in units of $\chi^2_{vac} - \chi^2_{matter}$ of each data sample.

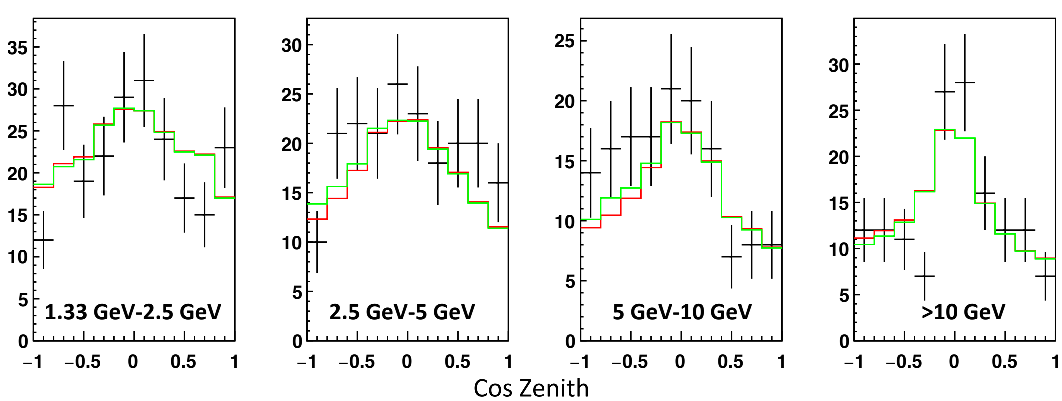

Figure 5.12: "Multi-GeV e-like, neutrino-like" data and MC expectation. The black are data with statistical error bars. The green shows the MC expectation for the best fit standard matter point. The red shows the MC expectation for the best fit vacuum point.

lower than what is implied by Wilks' theorem. Based on the same toy MC study, the expected sensitivity to exclude vacuum oscillations is 1.8σ, which the fit result is well in line with.

Since long baseline experiments can put more stringent constraints on θ_{23} and Δm^2_{32} than SK atmospheric neutrino data alone, I also studied how the matter effect analysis changes if θ_{23} and Δm^2_{32} are constrained [6]. These two parameters were chosen to be constrained as (with 1σ uncertainties) $\Delta m^2_{32} = (2.55 \pm 0.04) \times 10^{-3}$ eV^2, and $\sin^2\theta_{23} = 0.5 \pm 0.0453$. Constrained χ^2 values were calculated from unconstrained χ^2 values by adding Gaussian penalty terms:

$$\begin{aligned} \chi^2_{\text{constrained}}(\Delta m^2_{32}, \theta_{23}, \delta_{CP}, \alpha) &= \chi^2_{\text{unconstrained}}(\Delta m^2_{32}, \theta_{23}, \delta_{CP}, \alpha) \\ &+ \left(\frac{\Delta m^2_{32} - \Delta m'^2_{32}}{\sigma_{\Delta m}}\right)^2 + \left(\frac{\sin^2\theta_{23} - \sin^2\theta'_{23}}{\sigma_{\theta_{23}}}\right)^2 \end{aligned} \tag{5.42}$$

where

$$\begin{aligned} \Delta m'^2_{32} &= 2.55 \times 10^{-3} \text{ eV}^2 \\ \sigma_{\Delta m} &= 0.04 \times 10^{-3} \text{ eV}^2 \\ \sin^2\theta'_{23} &= 0.5 \\ \sigma_{\theta_{23}} &= 0.0453. \end{aligned} \tag{5.43}$$

The result of applying these constraints is shown in Fig. 5.13. The constraints result in a mild decrease in the preference for standard matter compared to vacuum oscillations. This occurs because the standard matter fit slightly disfavors maximal mixing, while the vacuum oscillation best fit is nearly maximal mixing.

[6] This studied was initiated in response to a request from a referee during the review of [30] for publication.

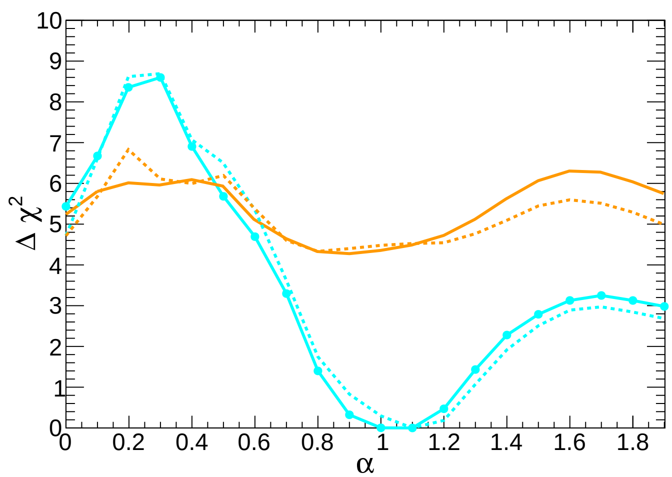

Figure 5.13: Result with constraint on θ_{23} and Δm^2_{32}. Orange is for inverted hierarchy, cyan for normal hierarchy. Solid lines are for the unconstrained result (identical to Fig. 5.10) while dotted lines are for the constrained result.

Chapter 6

Boosted Dark Matter

As will be discussed in Section 6.1, there is ample evidence for the existence of dark matter. In fact, its abundance has been well determined by observation of fluctuations in the Cosmic Microwave Background (CMB) to account for about 25% of the energy density of the universe [1, 2]. However, beyond its existence and abundance, little else is known about the properties of dark matter. In this chapter I will discuss a recently proposed alternative to the popular Weakly Interacting Massive Particle (WIMP) paradigm, called boosted dark matter. I will report the results of a search for boosted dark matter using SK-IV data.

6.1 Dark Matter Evidence

The most conclusive direct evidence for the existence of Dark Matter comes from three sources spanning about 70 years: Fritz Zwicky's observation of the "Coma Cluster" in the 1930's, Vera Rubin's measurements of galaxy rotation curves in the 1970's and 1980's, and the observation of the "Bullet Cluster" by both optical and x-ray telescopes in the 2000's.

Apparent Velocities of Nebulae in the Coma Cluster	
8500 km/s	6900 km/s
7900 km/s	6700 km/s
7600 km/s	6600 km/s
7000 km/s	5100 km/s

Table 6.1: Velocities of nebulae in the Coma Cluster reported by Fritz Zwicky. The lowest velocity nebula (5100 km/s) was commented to possibly be a field nebula, and not actually belong to the Coma Cluster. However, the likelihood of this was claimed to be low (about 1/16) and even removing that data point does not change Zwicky's conclusions [5].

6.1.1 The Coma Cluster

In 1933, Fritz Zwicky reported the measured apparent velocities of eight nebulae in the Coma Cluster, shown in Table 6.1 [5]. From the dispersion of apparent velocities, Zwicky noted that the different nebulae were moving relative to one another at around 1500 km/s to 2000 km/s. He compared this to the expectation based on the virial theorem, which for a gravitational system implies:

$$\langle T \rangle = -\frac{1}{2} \langle U \rangle , \tag{6.1}$$

where $\langle T \rangle$ and $\langle U \rangle$ are the time averages of the total kinetic and potential energies of the system. By observing the amount of light coming from the Coma Cluster, he estimated its mass to be about 1.6×10^{45} g. Applying the virial theorem, he found that the nebulae in the Coma Cluster should be moving at about 80 km/s relative to one another if all the mass in the Coma Cluster was due to visible matter. Because of this discrepancy, he proposed that perhaps "dark matter is present in much greater amount than luminous matter." [5]

6.1.2 Galaxy Rotation Curves

In the 1970's and 1980's Vera Rubin and collaborators measured the rotation curves of spiral galaxies. They found that even at the faintest edges of the galaxies, rotational velocities remained constant (Fig. 6.1). If the visible disc accounted for the majority of the masses of the galaxies, the rotational velocities would be expected to decrease with distance from the galactic nucleus. They concluded that non-luminous matter must be contributing significant mass past the extent of the luminous discs of these galaxies [61]. Fig. 6.2 shows an example galaxy rotation curve, along with contributions from the visible disc, gas, and dark halo. The data clearly agrees well with expectation when all three contributions are included, and exclusion of the dark halo contribution leaves the data very difficult to explain.

6.1.3 The Bullet Cluster

In the early 2000's a rather incredible galaxy cluster was discovered. Nicknamed the Bullet Cluster, cluster 1E 0657-558 is actually a merger between two galaxy clusters, with the collision happening almost perfectly in the observational plane. Clowe et. al. combined x-ray images from the Chandra X-ray Observatory with optical images from the Hubble Space Telescope, 6.5 m Magellan telescopes, and the ESO telescopes to observe the plasma, stellar component, and gravitational wells of the two colliding galaxies (Fig. 6.3) [64]. They observed that the stellar components appeared to pass right through one another, while the plasma lagged behind the stellar components and exhibited a clear bow-shock due to the collision. Both of these observation were as expected, as the plasma of the two clusters interact during the collision, while the relatively sparse stellar components pass right by each other. They also used Chandra x-ray data and the amount of light coming from the stellar compo-

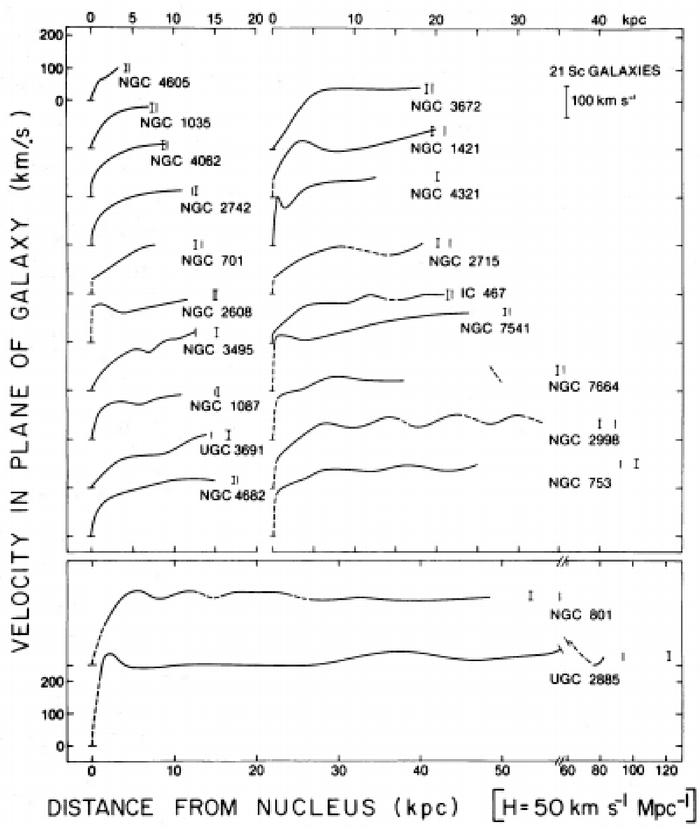

Figure 6.1: Rotation curves of 21 spiral galaxies presented in [61]. Taken from [61].

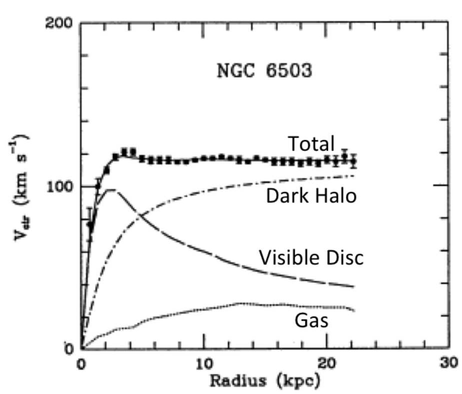

Figure 6.2: An example galaxy rotation curve. Note that the expectation from the combined visible disc, gas, and dark halo fits the observed data very well, while attempting to explain the data with only the disc and gas would be extremely questionable. Taken from [62], originally from [63]

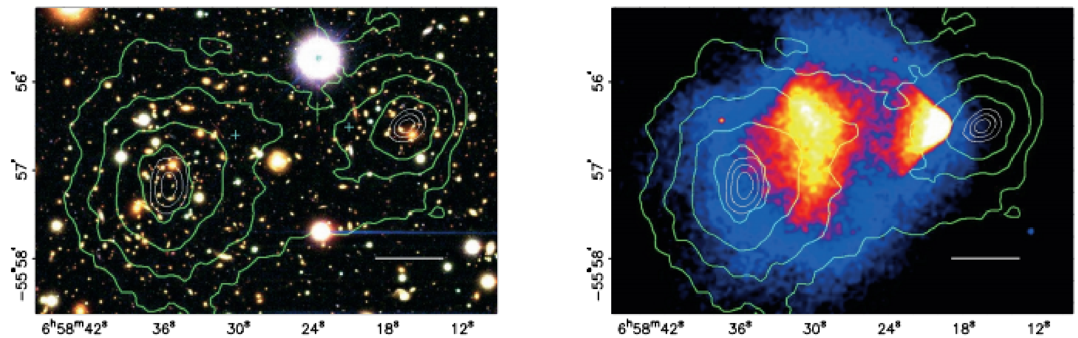

Figure 6.3: The Bullet cluster (1E 0657-558). On the left is the optical image of the cluster, while the right shows the plasma of the cluster, mapped from X-rays. The green contours shows the gravitational potential, computed using weak gravitational lensing. Note how the gravitational lensing and stellar components of the galaxies coincide, with the two colliding clusters appearing to have passed right through one another with minimal interaction. The plasma, meanwhile, is offset from the gravitational and stellar portions of the clusters, with the plasma of the right cluster exhibiting a clear bow-shock due to the collision. Taken from [64].

nents of the galaxies to estimate the amount of baryonic mass in each component, and confirmed that the plasma was the dominant contributor of baryonic mass. However, when they mapped the gravitational potential using weak gravitational lensing, they found that it coincided with the stellar components. This indicated that the majority of the mass of the clusters is non-interacting Dark Matter, and like the sparse stellar components, has been essentially unaware of any collision taking place.

6.2 Dark Matter Candidates

Over the years, a number of potential Dark Matter candidates have been proposed. Here I present a few of the most popular candidates, along with their current experimental status.

6.2.1 Massive Compact Halo Objects

Massive Compact Halo Objects (MACHOs) are large massive objects which do not give off any light. Examples of MACHOs include neutron stars, black holes, brown dwarfs, and planets which are not associated with any star. If numerous enough, these objects could account for dark matter, since estimates of mass made by measuring light coming from a source do not account for them. Such objects would be made of standard model matter, and require no new type of particle to explain dark matter.

The MACHO, EROS, and OGLE collaborations all searched for MACHOs by looking for micorlensing events in the Large and Small Magellanic Clouds. When a MACHO passes in front of a star, gravitational microlensing causes the intensity of the star to appear to increase, as the light from the star is focused by the gravitational potential of the object passing in front of it. The EROS and OGLE collaboration both found no significant signal, and reported upper limits which set the fraction of Galactic dark matter mass coming from reasonably sized MACHOs below 10% [65, 66]. The MACHO collaboration found 13-17 signal events, with an expected background of 2-4 events, and reported a best fit signal region of MACHOs with a typical mass of 0.4 $M_{\odot}$ making up about 20% of the dark matter in the Galaxy, with a 95% confidence region ranging from 8% to 50% of the dark matter in the Galaxy [67]. The results of all three experiments are shown in Fig. 6.4. Taken together, these results indicate that while MACHOs may account for some of the dark matter, they cannot explain it all; some other form of dark matter is required.

6.2.2 Weakly Interacting Massive Particles

The Weakly Interacting Massive Particle (WIMP) is currently the most popular dark matter candidate. WIMP theories propose a generic massive particle not

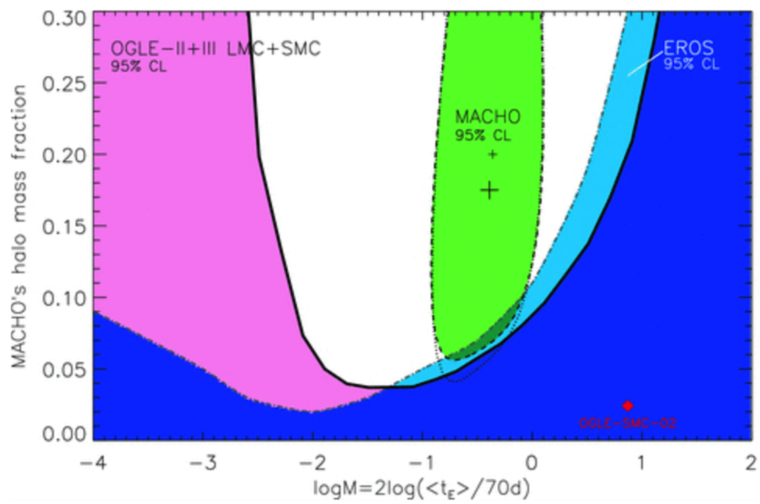

Figure 6.4: Results from OGLE, EROS and MACHO. The solid line is the exclusion limit from OGLE, the dashed-dotted line is the exclusion for EROS, while the dashed and dotted lines show the allowed region from two slightly different analyses of the MACHO data. The colored regions are the regions allowed by each experiment, and the two crosses represent the best fit points of the two different analyses of the MACHO data. The units on the $x-$axis are base-10 logarithm of the typical MACHO mass (in units of Solar Mass). Taken from [66].

included in the standard model which interacts with standard model particles only through the weak interaction and gravity. Perhaps one of the most appealing aspects of simple WIMP theories has been the so called "WIMP Miracle": if there were a fairly massive particle which coupled to the photon bath with an interaction strength characteristic of the weak interaction, the comoving abundance of that particle would freeze out at right around the observed abundance of dark matter in the universe.

Unfortunately, although the WIMP Miracle provides an elegant theoretical basis for the WIMP as dark matter, experimental attempts to detect WIMPs have thus far yielded no discovery [68–70] [1]. WIMP direct detection experiments search for the

[1] While the DAMA/LIBRA collaboration has reported a highly statistically significant potential signal in the form of a seasonal modulation in event rate, issues remain with interpreting this signal as dark matter. The DAMA/LIBRA result makes no attempt to separate neutron recoils from electronic recoils, so the possibility that the modulation is in fact an as yet unexplained seasonal modulation of the background remains. Combined with the fact that the DAMA/LIBRA signal region is, under relatively standard assumptions, now excluded by orders of magnitude by other

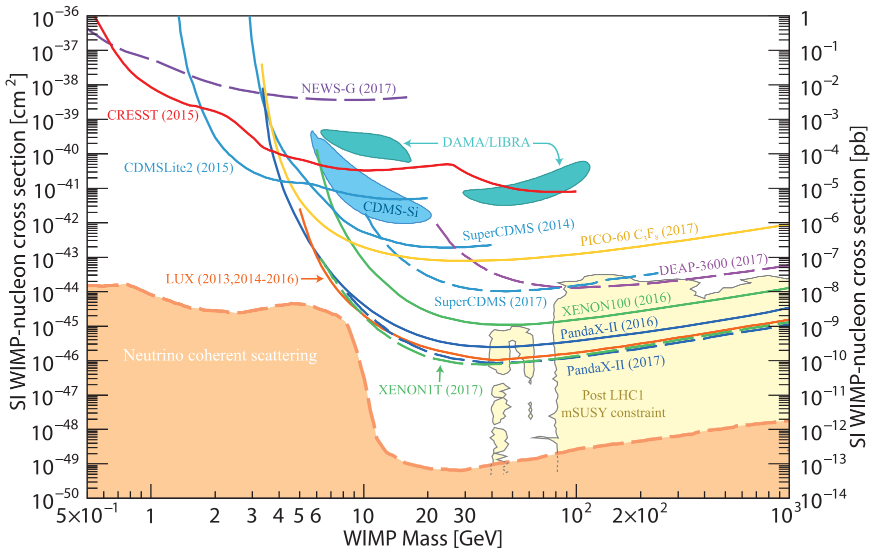

Figure 6.5: Spin independent cross section limits from direct detection experiments. The green and blue shaded regions represent the proposed signal regions of the CDMS-Si (since excluded by SuperCDMS) and DAMA/LIBRA experiments. The yellow region shows a scan of parameter space of CMSSM, NUHM1, NUHM2, and pMSSM10 (4 typical SUSY models) with constraints from ATLAS Run 1. The orange region shows the region where background from neutrino coherent scattering is no longer negligible. Taken from [13].

recoil of a target nucleon due to the interaction of a passing dark matter particle. Figure 6.5 shows the current status of direct detection spin independent cross section limits, which have now pushed orders of magnitude below weak interaction cross sections. These limits have begun to approach the so-called "neutrino floor," at which point solar neutrinos interacting with the target nuclei will become a significant source of background.

WIMPs have also been searched for by indirect detection. In these searches, one looks for the standard model particles (generally neutrinos, gammas or positrons) resulting from the annihilation or decay of WIMPs in regions of high dark matter

direct detection experiments, this result cannot yet be definitively affirmed as detection of dark matter. Recently, multiple experiments using the same detector technology as DAMA/LIBRA have begun taking data in different parts of the world (including, importantly, the Southern Hemisphere), which should conclusively either confirm or reject the DAMA/LIBRA result.

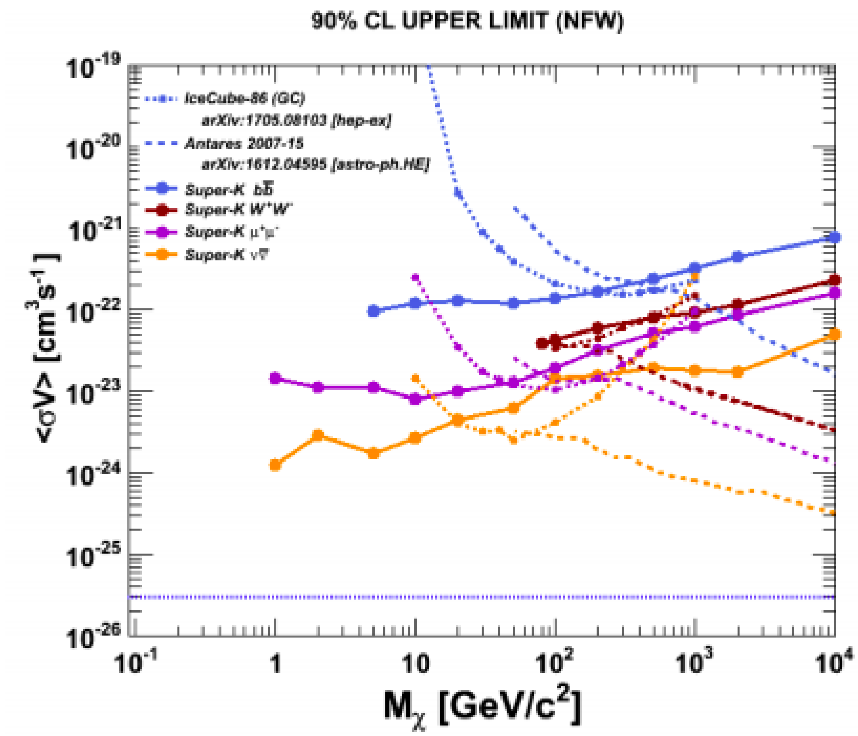

Figure 6.6: WIMP annihilation cross section limits from SK, Ice Cube, and Antares. The flat dashed blue line represents the approximate annihilation cross section required for the WIMP miracle.

density, such as the Galactic Center, Sun, or Earth. By looking at neutrinos, SK, Ice Cube, and Antares have all reported limits on the WIMP annihilation cross section that are approaching, but still one to two orders of magnitude above, the annihilation cross section required for the WIMP miracle (Fig. 6.6) [71–73].

Finally, WIMPs can be searched for at particle accelerators, which could create WIMPs if they exist. Both ATLAS and CMS have searched for WIMPs and set exclusion limits, shown in Fig. 6.7 [74, 75]. These experiments tend to set the best limits for low mass WIMPS, below the detector threshold of direct detection experiments.

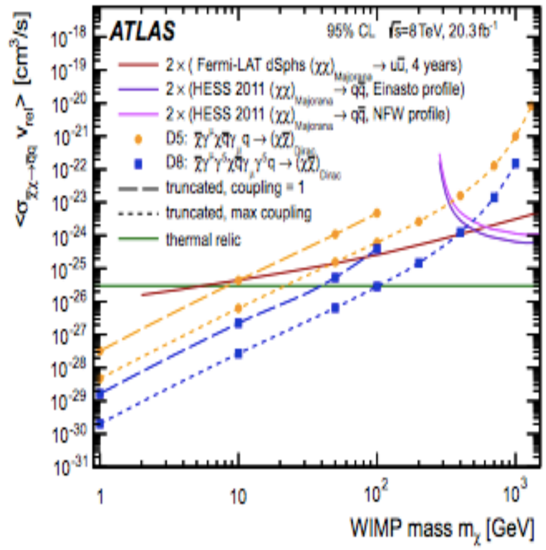

(a) ATLAS

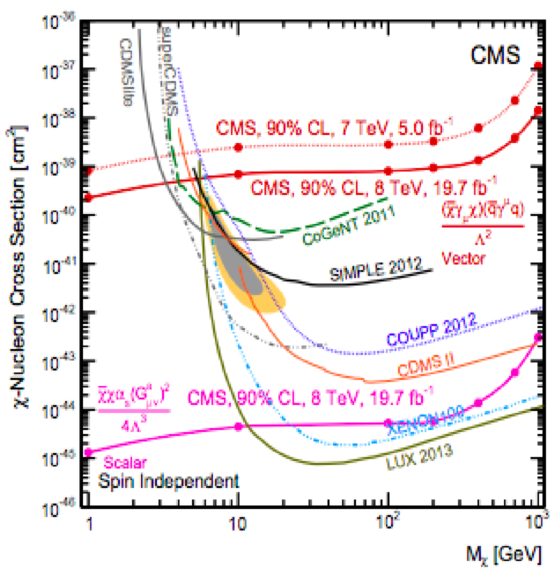

(b) CMS

Figure 6.7: At left, ATLAS limit for WIMP annihilation cross section, taken from [74]. At right, spin independent WIMP-nucleon cross section limit from CMS, taken from [75].

6.2.3 Relic Neutrinos

The Cosmic Neutrino Background (CνB) is the neutrino analog to the Cosmic Microwave Background (CMB); a cosmic soup of very low temperature neutrinos permeating the universe. While CνB neutrinos have never been directly observed, measurements of the primordial abundances of light elements, CMB anisotropies, and large scale cosmological structures all provide indirect evidence which lead to significant confidence in the existence of the CνB [13].

CνB neutrinos seem to be a prime dark matter candidate, as they require no new physics, and are strongly believed to exist. However, a relatively simple calculation shows that CνB neutrinos can only account for a small portion of the dark matter content of the universe. First, the temperature of the CνB can be found from the temperature of the CMB to be 1.95 K. This is slightly less than the 2.73 K temperature of the CMB because light neutrinos (with masses less than 1 MeV) decoupled from the primordial soup just before electron-positron annihilation occurred. Therefore, the CMB is slightly "heated" compared to the CνB. The exact relationship between the CνB and CMB temperatures can be found by invoking conservation of entropy and comparing the number of relativistic degrees of freedom before and after electron-positron annihilation, to find that $T_\nu = (4/11)^{1/3} T_\gamma$. For more detail, see for example Chapter 22 of [13]. For light neutrinos, the number density of each neutrino flavor can be found to be about 112 cm^{-3}. This leads to the total energy density of the CνB being:

$$\Omega_\nu h^2 = \frac{\sum m_{\nu,i}}{94\text{eV}}, \tag{6.2}$$

where $\sum m_{\nu,i}$ sums the masses of the three neutrino mass states, and h^2 is the reduced Hubble Constants, defined as $h = H_0/(100\text{km s}^{-1}\text{Mpc}^{-1}$, where H_0 is the current expansion rate of the universe. Upper limits on the sum of the neutrino masses have been set at about 7 eV by measurement of the tritium beta decay spectrum by the Troitsk and Mainz experiments, resulting in $\Omega_\nu h^2 < 0.074$ [46, 76]. Cosmological and CMB data meanwhile, have indirectly set limits of $\sum m_\nu < 0.23$ eV, leading to the more stringent limit $\Omega_\nu h^2 < 0.002$ [1]. The CνB can thus not account for the observed dark matter content of the universe, which from the CMB is $\Omega_\nu h^2 = 0.12$ [1, 2].

6.2.4 Sterile Neutrinos

Although the arguments presented in Section 6.2.3 limit the *active* neutrino contribution to dark matter, keV scale sterile neutrinos remain a viable Dark Matter candidate. A fourth (at least) neutrino mass state can be proposed, along with a right handed sterile flavor state, which does not couple via the weak interaction. The fourth mass state can be written as a superposition of sterile and active flavor states:

$$\nu_4 = \cos\theta_s \nu_s + \sin\theta_s \nu_a, \tag{6.3}$$

with a sterile mixing angle θ_s. Dark matter sterile neutrinos can be searched for by looking for X-rays from the decay [77]

$$\begin{gathered} \nu_4 \to \gamma\nu_i, \\ i = 1, 2, 3. \end{gathered} \tag{6.4}$$

X-ray observations of the diffuse cosmic background and galactic clusters provide a limit on dark matter sterile neutrinos which ranges from $\sin^2 2\theta_s < 10^{-14}$ at $m_4 = 100$ keV to $\sin^2 2\theta_s < 10^{-6}$ at $m_4 = 2$ keV. There has been a faint unexplained X-ray line at around 3.55 keV observed from the Perseus and Andromeda Galaxy clusters, which could be interpreted as coming from the decay of dark matter sterile neutrinos with $m_4 = 7.1$ keV and $\sin^2 2\theta_s \sim 7 \times 10^{-11}$ [78, 79]. However, this line is quite faint, and other potential explanations do exist. At this point keV sterile neutrinos remain a potential dark matter candidate.

6.2.5 Axions

Axions were first proposed as part of a solution to the "strong CP problem", which addresses the question of why the QCD CP-violating phase appears to be so close to zero. In order to explain the apparent CP conservation of nature, the CP violating phase θ could be promoted to a field, and a new global symmetry $U(1)_{PQ}$ (Peccei-Quinn symmetry) proposed [80]. The spontaneous symmetry breaking of this $U(1)_{PQ}$ would result in a new particle, called the axion [81, 82].

"Standard axions" were quickly ruled out when the axion was first proposed, but "invisble axions" which couple very minimally to standard model matter remain possible, and are a reasonable dark matter candidate. Various experiments have searched for axions, generally taking advantage of the property that axions can convert into photons (and vice-versa) in the presence of strong magnetic or electric fields [83]. Experiments searching for "light passing through walls" [84], axions from the sun [85], and axions as part of the galactic Dark Matter halo [86] have set limits on the axion mass and coupling strength, though much available parameter space remains.

6.3 Boosted Dark Matter

Since the evidence for the existence of dark matter is quite robust, while the particular identity of dark matter remains unresolved, various new possibilities must continually be considered. One possibility is that some dark matter is in fact not cold, but is highly relativistic and has been produced at late times. This form is denoted "boosted" dark matter [87–93]. Boosted dark matter could exist as a subdominant dark matter component, with a dominant cold dark matter component accounting for most of the dark matter energy density of the universe. In this way, boosted dark matter can remain consistent with the well established cosmological theory of ΛCDM, which consists of long lived dark matter that was non-relativistic ("cold") at freeze-out and a cosmological constant Λ, corresponding to dark energy. The subdominant boosted dark matter can be the same particle as the dominant cold dark matter, or it can be a different, lighter particle. Boosted dark matter can be produced from the dominant cold dark matter through a variety of processes, including annihilation [94–96], semi-annihilation [94, 97–100], number-changing 3→2 self-annihilation [101–104], and decay [91, 105]. Boosted dark matter can then be observed through its scattering off electrons or nuclei in large volume terrestrial detectors [106, 107]. Current direct detection limits can be evaded in multi-component models by having only the boosted dark matter species couple directly to Standard Model particles [87, 91–93] or in boosted dark matter single-component models by invoking a spin dependent dark matter-nucleon cross section [93].

Reference [87] presents a baseline boosted dark matter model. This model introduces two dark fermions ψ_A and ψ_B and a massive dark photon γ', with an assumed mass ordering $m_A > m_B > m_{\gamma'}$. The particle ψ_A is proposed to be the dominant cold dark matter in the universe, and does not couple directly to Standard Model particles. The particle ψ_B is the boosted dark matter, and couples to Standard Model particles through the exchange of the dark photon γ', as in Fig. 6.8. The coupling between γ' and ψ_B is set by a coupling constant g' which is proposed to be large but perturbative, while the coupling between γ' and e^- is scaled from $\gamma - e^-$ coupling by the constant ε. The relic abundance of ψ_A is determined by an assisted freeze

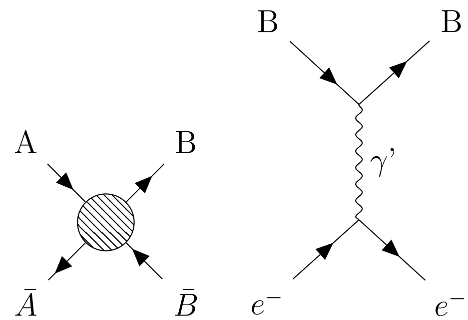

(a) Annihilation $A\bar{A} \to B\bar{B}$ (b) Scatter of electron by boosted dark matter particle B

Figure 6.8: Fenyman diagrams of boosted dark matter creation by annihilation of dominant heavy dark matter particles, and scatter of electron by boosted dark matter through exchange of a dark photon.

out scenario, and the thermal cross section is set to $\langle \sigma_{A\bar{A}\to B\bar{B}v} \rangle = 5 \times 10^{-26}$ cm^3/s in order to achieve the observed relic density $\Omega_A \approx 0.2$ [87]. The flux of boosted dark matter from the galactic center is

$$\frac{d\Phi}{d\Omega dE_B} = \frac{1}{2}\frac{r_{\text{sun}}}{4\pi}\left(\frac{\rho_{\text{local}}}{m_A}\right)^2 \mathcal{J}\langle \sigma_{A\bar{A}\to B\bar{B}}v \rangle \delta(E_B - m_A), \tag{6.5}$$

where r_{sun} is the distance of the Sun from the galactic center (about 8.33 kpc), ρ_{local} is the local dark matter density, $\mathcal{J}$ is the "$\mathcal{J}$-factor" along the direction considered (see Section 6.5).

This model can be described by five free parameters: the mass of the dominant dark matter species m_A, the mass of the boosted dark matter m_B, the mass of the dark photon $m_{\gamma'}$, and the coupling constants g' and $\varepsilon\alpha$ (α being $\gamma - e^-$ couping constant). Since the boosted dark matter is coming from annihilation of ψ_A, the energy of the boosted dark matter is equal to m_A. The maximum energy of the recoil

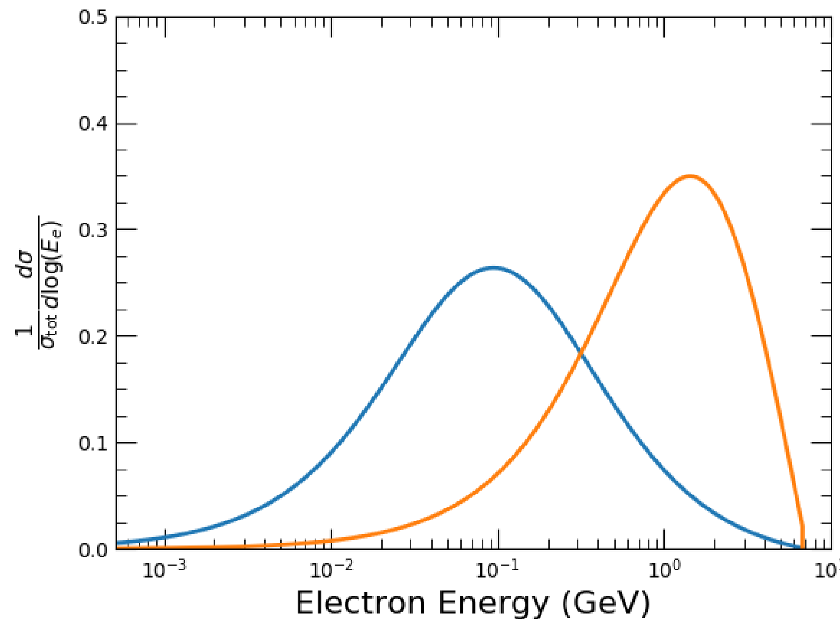

Figure 6.9: Recoil electron spectrum for simple model. The blue is for $m_{\gamma'} = 10$ MeV, while the red is for $m_{\gamma'} = 50$ MeV. Both use values of $m_A = 20$ GeV and $m_B = 200$ MeV.

electron scattered by the boosted dark matter is then set by kinematics:

$$E_e^{\rm max} = m_e \frac{(m_A + m_e)^2 + m_A^2 - m_B^2}{(m_A + m_e)^2 - m_A^2 + m_B^2}. \tag{6.6}$$

The shape of the recoil electron spectrum is largely set by the mass of the dark photon, with lower values of the dark photon mass leading to a spectrum more peaked towards smaller electron recoil energies, as shown in Fig. 6.9. The values of the coupling constants g' and $\varepsilon\alpha$ act simply as a scaling factors of the $\psi_B - e^-$ cross section.

6.4 Searching for Boosted Dark Matter

I performed a search for boosted dark matter coupling to electrons in Super-Kamiokande, with the scattered electron energies ranging from 100 MeV to 1 TeV. Since boosted dark matter is expected to originate in regions of high dark matter density, this search looks for a signal coming from the Galactic Center or the Sun[2]. Cones are drawn around the signal source, and the number of events passing a set of analysis cuts in each cone is counted. The search is deliberately kept as simple and model-independent as possible. This way, the results can be applied to any model predicting an excess of particles from the Galactic Center or Sun that would elastically scatter electrons to energies above 100 MeV.

6.5 Galactic Halo Models

The boosted dark matter described here comes from an interaction of the heavy non-interacting dark matter. Therefore its directional distribution around the galactic center is dependent on the density profile of the dark matter halo. A general form for the density profile (assumed to be spherically symmetric) from cold dark matter simulations is [108]

$$\rho(r) = \frac{\rho_0}{(r/r_s)^\gamma [1 + (r/r_s)^\alpha]^(\beta - \gamma)/\alpha}. \tag{6.7}$$

Parameters of Equation 6.7 for the NFW [109], Moore [110], and Kravtsov [111] halo models are shown in Table 6.2.

[2]Some boosted dark matter models predict a significant capture rate of cold dark matter in the Sun. This can be achieved either through a spin dependent dark matter-nucleus cross section [89] or through the combination of a relatively strong dark matter self interaction and coupling between cold dark matter and Standard Model particles through boosted dark matter loops [92]

	α	β	γ	r_s	ρ_0	$\rho(R_{sc})$
Moore	1.5	3	1.5	28	0.0527	0.27
NFW	1	3	1	20	0.259	0.3
Kravtsov	2	3	0.4	10	0.703	0.37

Table 6.2: Halo parameters for NFW, Moore, and Kravtsov models. The scale radius r_s is in units of [kpc] while the two densities ρ_0 and $\rho(R_{sc})$ are in units of [GeV/cm^3]. R_{sc} is the solar circle radius, 8.5 kpc [108].

The rate of boosted dark matter events coming from the annihilation or decay of dark matter from a particular direction in the sky is proportional to the so called "$\mathcal{J}$-factor". It is the line of sight integral of dark matter density for decay, or density squared for annihilation. The $\mathcal{J}$-factor is a function of the angle between the event direction and the direction to the galactic center:

$$\mathcal{J}_{ann}(\theta_{\rm GC}) = \frac{1}{R_N \rho_N^2} \int_0^{l_{\rm max}} \rho^2 \left(\sqrt{R_{sc}^2 - 2lR_{sc}\cos\theta_{\rm GC} + l^2} \right) dl, \tag{6.8}$$

$$\mathcal{J}_{decay}(\theta_{\rm GC}) = \frac{1}{R_N \rho_N} \int_0^{l_{\rm max}} \rho \left(\sqrt{R_{sc}^2 - 2lR_{sc}\cos\theta_{\rm GC} + l^2} \right) dl, \tag{6.9}$$

where θ_{GC} is the angle to the Galactic Center and R_{sc} is the solar circle radius (8.5 kpc). The upper limit of integration $l_{\rm max}$ is defined by the adopted halo size $R_{\rm MW}$:

$$l_{\rm max} = \sqrt{R_{\rm MW}^2 - R_{sc}^2 \sin^2\theta_{GC}} + R_{sc}^2 \cos\theta_{GC}. \tag{6.10}$$

While the halo size $R_{\rm MW}$ appears to be an additional important parameter, ρ drops off sharply past 20-30 kpc, as shown in Fig. 6.10(a). The calculation of $\mathcal{J}$ is thus insensitive to the choosen value of $R_{\rm MW}$ as long as it is above this range. The prefactors $\frac{1}{R_N \rho_N^2}$ and $\frac{1}{R_N \rho_N}$ in Eqs. (6.8) and (6.9) are arbitrary scaling factors used to make $\mathcal{J}$ dimensionless. Fig. 6.10 shows the dark matter halo density $\mathcal{J}$-factors for

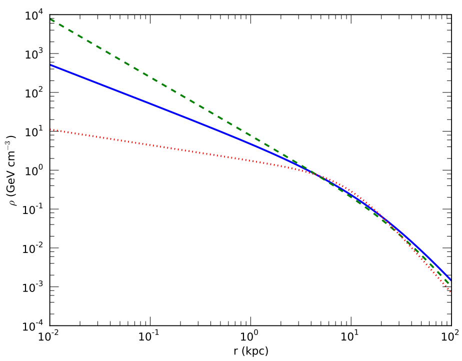

(a)

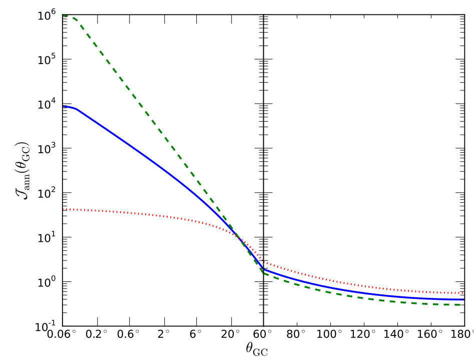

(b)

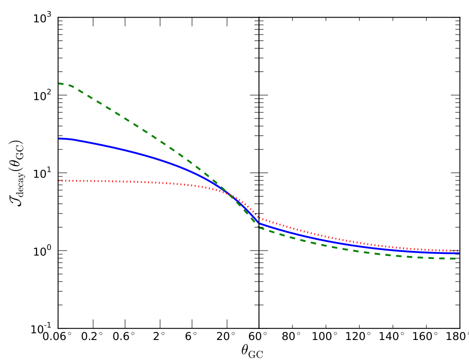

(c)

Figure 6.10: Moore (dashed green), NFW (solid blue) and Kravstov (dotted red) dark matter halo models. 6.10(a) shows the dark matter density as a function of distance from the galactic center. 6.10(b) and 6.10(c) show the $\mathcal{J}$-factors for annihilating and decaying dark matter as a function of angle from the galactic center. Note that the x-axis is logarithmic on the left and linear on the right of 6.10(b) and 6.10(c).

the Moore, NFW, and Kravstov models. The $\mathcal{J}$-factors in Figs. 6.10(b) and 6.10(c) are calculated with $R_{\rm MW} = 40$ kpc and the standard scaling choice of $R_N = R_{sc} = 8.5$ kpc, $\rho_N = 0.3$ GeV/cm^3. The $\mathcal{J}$-factor is taken to be flat at the innermost $0.1°$ to avoid divergence of $\mathcal{J}$ due to cuspy profiles, which may be an artifact of simulation [108].

6.6 Signal Monte Carlo

A signal monte carlo (MC) sample of 200,000 simulated electromagnetic shower events was produced. The MC was split into 4 energy ranges: 30 MeV-1 GeV, 1 GeV-10 GeV, 10 GeV-100 GeV, and 100 GeV to 1 TeV. Fifty thousand events were produced in each energy range, with a flat linear energy spectrum in each range. Event positions inside the detector were randomly selected from a uniform distribution extending to within 1 m of the wall of the ID. This was done in order to account for migration of events near the boundary of the fiducial volume, which is 2 meters inside the wall of the ID. The direction of the electromagnetic showers was chosen assuming the NFW halo model and dark matter annihilation. For each event, a random direction in equatorial coordinates was chosen so that the probability of an event's source being placed at an angle θ_{GC} from the galactic center is proportional to $\mathcal{J}_{\mathrm{ann}}(\theta_{\mathrm{GC}})\sin\theta_{\mathrm{GC}}$. The $\sin\theta_{\mathrm{GC}}$ factor is a geometrical effect. While there is expected to be some model dependent smearing between the boosted dark matter direction and the scattered electron direction, the scattering is expected to be strongly peaked in the forward direction [87]. Due to the minimal impact and model dependence of directional smearing, this effect is ignored in the production of the signal MC. In order to transform from equatorial coordinates to the horizontal coordinates of the detector, a random time is chosen for each event. These times are randomly distributed at times during SK good data runs used in the analysis. Even though the simulation is created assuming the NFW halo model and dark matter annihilation, other combinations of halo models and production mechanism can be studied by reweighting each event by the ratio of the new combination's $\mathcal{J}$-factor to the NFW annihilation $\mathcal{J}$-factor:

$$w_{\mathrm{Model\ X}} = \frac{\mathcal{J}_{\mathrm{Model\ X}}(\theta_{\mathrm{GC}})}{\mathcal{J}_{\mathrm{NFW\ ann}}(\theta_{\mathrm{GC}})} \tag{6.11}$$

Similarly, the model dependent smearing between the boosted dark matter and scattered electron directions can similarly be added into the simulation by event reweighting.

6.7 Event Selection

A cut-based selection is applied to select electron elastic-scatter-like events. The selection begins with the FCFV sample, which consists of all events which pass the Fully-Contained event reduction, plus four additional cuts: `wall`>200 cm, which defines the fiducial volume, `nhitac`<16, `evis`>30 MeV, and if the event is 1-ring elike, the final cut `amome`>100 MeV (the variable `amome` is the reconstructed momentum of the ring under the assumption that the particle is an electron). From this FCFV sample, four analysis cuts are applied:

1. 1-ring (if `evis`<100 GeV)
2. e-like
3. 0 decay electrons
4. 0 tagged neutrons

The first two cuts search for a single relativistic electron, while the final two cuts remove events with a signature of a nuclear interaction. Decay electrons in e-like events are the result of the $\pi^{\pm} \rightarrow \mu^{\pm} \rightarrow e^{\pm}$ decay chain with the $\pi^{\pm}$ coming from a neutrino-nucleus interaction. Tagged neutrons are those that have escaped the nucleus following a neutrino-nucleus interaction, or are knocked out of a nucleus by particles propagating after the interaction. These neutrons thermalize, and capture on hydrogen. Neutron captures are particularly numerous following neutrino deep inelastic scattering. Neither decay electrons nor neutron captures should occur following the elastic scatter of an electron by a boosted dark matter particle. The 1-ring cut is not applied for events with visible energy above 100 GeV, as the ring counting algorithm, which is tuned for lower energy events, becomes unreliable at such high energies. We choose to restrict this analysis to SK-IV data only in order to take advantage of neutron tagging to remove atmospheric neutrino background.

Because the atmospheric neutrino background to this search is strongly energy dependent, events are separated into three samples based on visible energy with ranges 100 MeV<$\mathrm{E_{vis}}$ <1.33 GeV, 1.33 GeV<$\mathrm{E_{vis}}$ <20 GeV , and $\mathrm{E_{vis}}$ >20 GeV. The number of data events is shown for each sample in Table 6.3, along with the simulated atmospheric neutrino Monte-Carlo (MC) expectation. The signal efficiency at representative energies based on signal electron MC is also shown. The importance of the decay electron and neutron tagging cuts is particularly evident in the highest energy sample ($E_{vis} > 20$ GeV), where they reduce the background by about a factor of 10 with minimal effect on signal efficiency.

The angular and energy resolutions for events passing all selection and analysis cuts are shown in Figures 6.11 and 6.12. As can be seen in Figure 6.11, the angular resolution for these events is better than 3° for all energy ranges. The bias in the high energy range (Figure 6.12(c)) is due to the detector becoming saturated for very high energy events.

The efficiency of the selection and analysis cuts is shown in Figure 6.13. Efficiency is defined as the number of events passing a set of cuts divided by the number of events simulated in the fiducial volume. This is not exactly equivalent to the fraction of cut-passing events produced in the fiducial volume, since events can migrate into, or out of, the fiducial volume. The total efficiency of the analysis rises sharply around 100 MeV and stays above 90% until around 5-10 GeV. It remains above 80% until around

	100 MeV< E_{vis} < 1.33 GeV			1.33 GeV < E_{vis} < 20 GeV		
	Data	ν-MC	ϵ_{sig}(0.5 GeV)	Data	ν-MC	ϵ_{sig}(5 GeV)
FCFV	15206	14858.1	97.7%	4908	5109.7	93.8%
& single ring	11367	10997.4	95.8%	2868	3161.8	93.3%
& e-like	5655	5571.5	94.7%	1514	1644.2	93.0%
& 0 decay-e	5049	5013.8	94.7%	1065	1207.2	93.0%
& 0 neutrons	4042	3992.9	93.0%	658	772.6	91.3%
	E_{vis} > 20 GeV					
	Data	ν-MC	ϵ_{sig}(50 GeV)			
FCFV	118	107.5	84.9%			
& single ring	71	68.2	82.2%			
& e-like	71	68.1	82.2%			
& 0 decay-e	13	15.7	82.2%			
& 0 neutrons	3	7.4	81.1%			

Table 6.3: Number of events over the entire sky passing each cut in 2628.1 days of SK4 data, simulated ν-MC background expectation, and signal efficiency at representative energy after each cut.

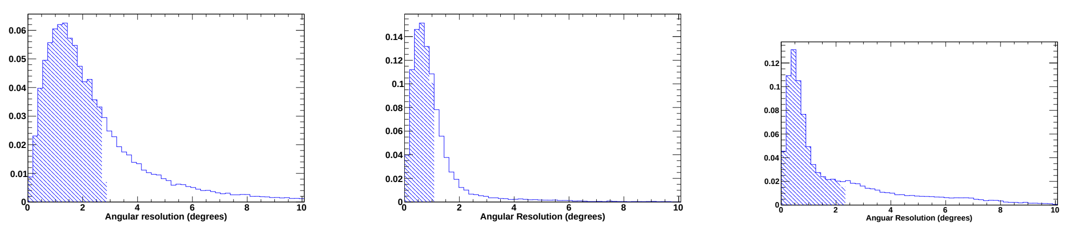

(a) E_e=30MeV-1GeV, σ=2.8° (b) E_e=1GeV-10GeV,σ=1.1° (c) E_e=10GeV-100GeV,σ=2.3°

Figure 6.11: Angular resolution for events passing all selection and analysis cuts, from signal MC in 3 energy ranges.

50 GeV. The main cause of the reduction of efficiency with increasing energy is the loss of containment at high energies; many higher energy electromagnetic showers are able to penetrate from the FV into the OD, and so do not pass fully-contained cuts.

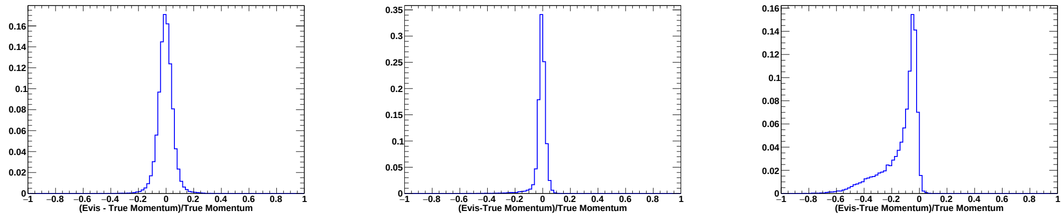

(a) E_e=30MeV-1GeV (b) E_e=1GeV-10GeV (c) E_e=10GeV-100GeV

Figure 6.12: Energy resolution for events passing all selection and analysis cuts, from signal MC in 3 energy ranges.

6.8 Ring Counting

The ring counting algorithms in APFIT have never been tuned for high energy events. As it turns out, APFIT finds phantom rings in many high energy electromagnetic showers as in Figure 6.14. The efficiency of the 1-ring cut for this analysis drops off very sharply around 10 GeV if no adjustment is made, as shown in Figure 6.15.

These phantom rings are caused by fluctuations in the light patterns of high energy events. Due to the large amount of light from high energy events, these statistical fluctuations can trick APFIT into thinking it sees a low energy ring in addition to the main ring. To fix this pathology, a test variable is constructed to merge rings which could reasonably be caused by statistical fluctuations:

$$\alpha^2_{i_{\text{ring}}} = \frac{1}{N_{\text{PMT},\theta<70^\circ}} \sum_{j_{\text{PMT}\theta<70^\circ}} \frac{Q\text{Dev}^2_{i_{\text{ring}},j_{\text{PMT}}}}{Q\text{Dev}_{i_{\text{MER}},j_{\text{PMT}}}}, \tag{6.12}$$

where $N_{\text{PMT}\theta<70^\circ}$ is the number of PMT's within 70° of the direction of the ring, i_{MER} is the index of the most energetic ring, and $Q\text{Dev}_{i,j}$ is the devided charge of the j$^{\text{th}}$

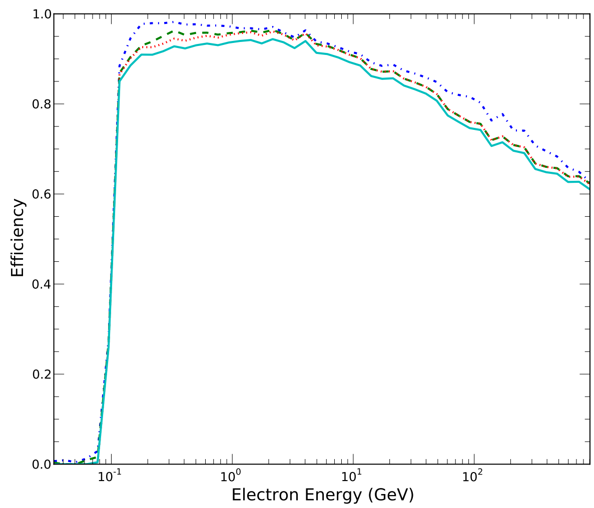

Figure 6.13: Efficiency of the selection and analysis cuts as a function of energy. Beginning with the FCFV reduction (dashed-dotted blue), the addition of the 1-ring (dashed green), e-like (dotted red) and finally 0 decay electrons and 0 tagged neutrons cuts to arrive at the final efficiency (solid cyan) are shown. Note that the efficiency of the 0 decay electrons cut is $> 99.99\%$, so that the drop from the dotted red line to solid cyan line is due solely to the background rate of the neutron tagging algorithm.

PMT assigned to the $\mathrm{i^{th}}$ ring, defined as:

$$QDev_{i,j} = Q_j^{\mathrm{measured}} \frac{Q_{i,j}^{\mathrm{expected}}}{\sum\limits_k Q_{k,j}^{\mathrm{expected}}}, \tag{6.13}$$

where $Q_{i,j}^{\mathrm{expected}}$ is the charge expected in the $\mathrm{j^{th}}$ PMT due to the $\mathrm{i^{th}}$ ring and Q_j^{measured} is the charge measured in the $\mathrm{j^{th}}$ PMT. The variable $QDev_{i,j}$ is stored in the common block array APPEDEV in APFIT. In order to fill APPEDEV with usable values, sprngsep(2,1,1,3) is run. For rings which are not the most energetic ring, α is calculated, and the ring is merged into the most energetic ring if $\alpha < 0.6$. Figure 6.16 shows the distribution of values of α for real and fake rings in the signal electromagnetic shower and background atmospheric neutrino MC. Since, the 1-ring cut efficiency is

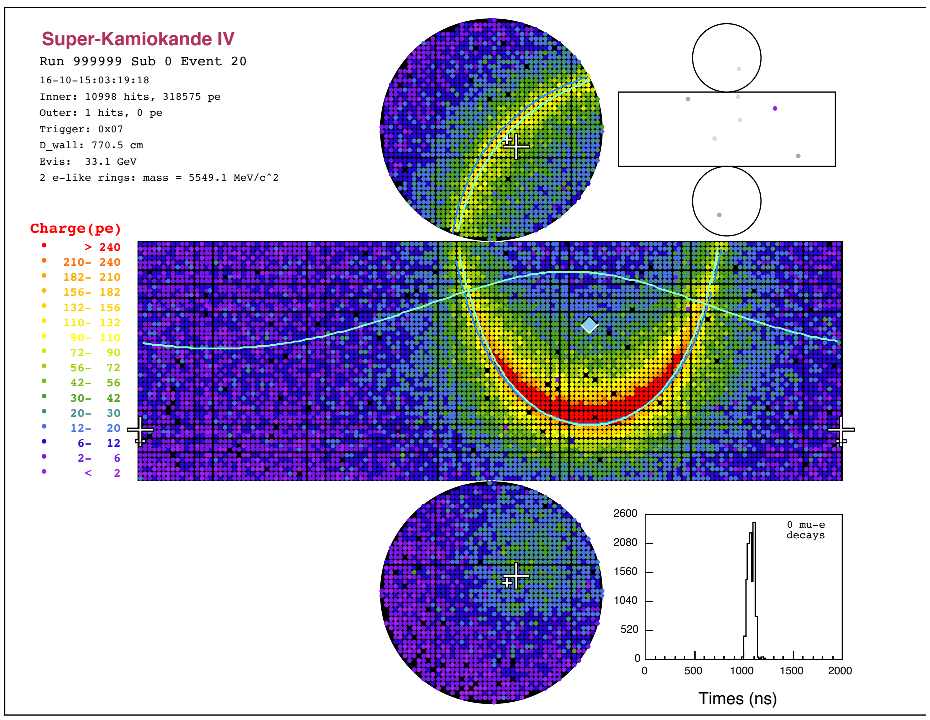

Figure 6.14: Example of a phantom ring found by APFIT. This is a single electron at 36 GeV. APFIT correctly finds the ring corresponding to the electron, but also finds an additional phantom ring. When the ring counting adjustment described in the section is applied, the phantom ring is removed.

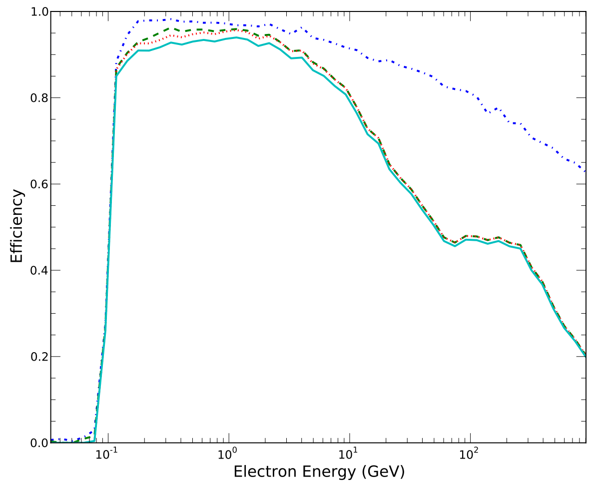

Figure 6.15: Effeciency of the selection and analysis cuts as a function of energy, with no ring counting adjustment. Color scheme is the same as in Figure 6.13. Note the sharp drop in the efficiency of the 1-ring cut (dashed green).

only problematic at high energies, this merging technique is only applied to events with E_{vis} >1.33 GeV. Even with merging, the efficiency of the 1-ring cut begins to deteriorate at around 100 GeV, so the cut is removed for events above 100 GeV. Since the atmospheric neutrino background drops sharply with energy, this has a minimal effect on the background. These adjustments to ring counting improve the final efficiency from that seen in Fig. 6.15 to that seen in Fig. 6.13, with minimal increase of the atmospheric neutrino background.

6.9 ID-OD Crosstalk

When ID PMTs are hit by very large amounts of light (100's to 1000's of pe), ID-OD crosstalk can occur leading to fake hits in the OD in the areas of high ID light activity. For the standard atmospheric neutrino FCFV sample this is a minimal issue, since there is not enough light in events with energies of a few GeV to cause

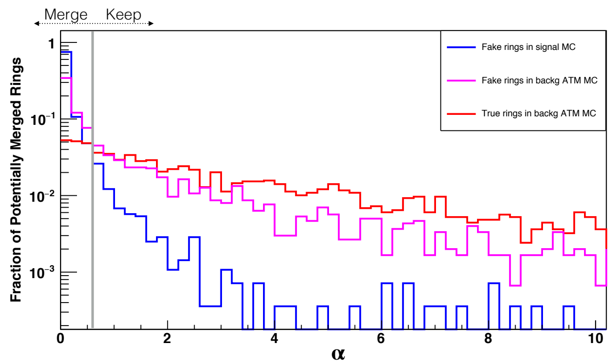

Figure 6.16: Test variable for merging rings in high energy events. If $\alpha > 0.6$, the ring is merged into the most energetic ring.

crosstalk problems. However, for higher energy events approaching 100 GeV, ID-OD crosstalk can lead to fake OD triggers and events failing FC selection even though their physics activity is contained within the ID. Consider as an example the event in Fig. 6.17 which failed the final `nhitac` cut of the official FC selection. It is clear that this is not a normal PC event. There is no exit point in the ID, and the OD activity is in the same location as the ID activity, as opposed to in the location a particle traveling in the direction of the ID ring would be expected to exit the ID.

Fortunately, OD crosstalk hits are fairly easy to recognize, as they usually have very small PMT pulses. Figure 6.18 shows the distribution of the size of OD hits for three energy samples, in data and MC. In the data, there is a dramatic spike of low p.e. OD hits in the highest energy sample, due to ID-OD crosstalk. The small size of the ID-OD crosstalk hits is likely due to the bipolarity of crosstalk induced signals; the positive and negative portions of crosstalk induced signals nearly cancel one another out once integrated. Fig. 6.19 shows the same event as Fig. 6.17, with OD hits of less than 0.2 p.e. removed. Note that the OD is now quiet.

In order to compensate for this ID-OD crosstalk, I ran an adjusted version of FC reduction for the Boosted Dark Matter analysis. Anywhere in the FC reduction that

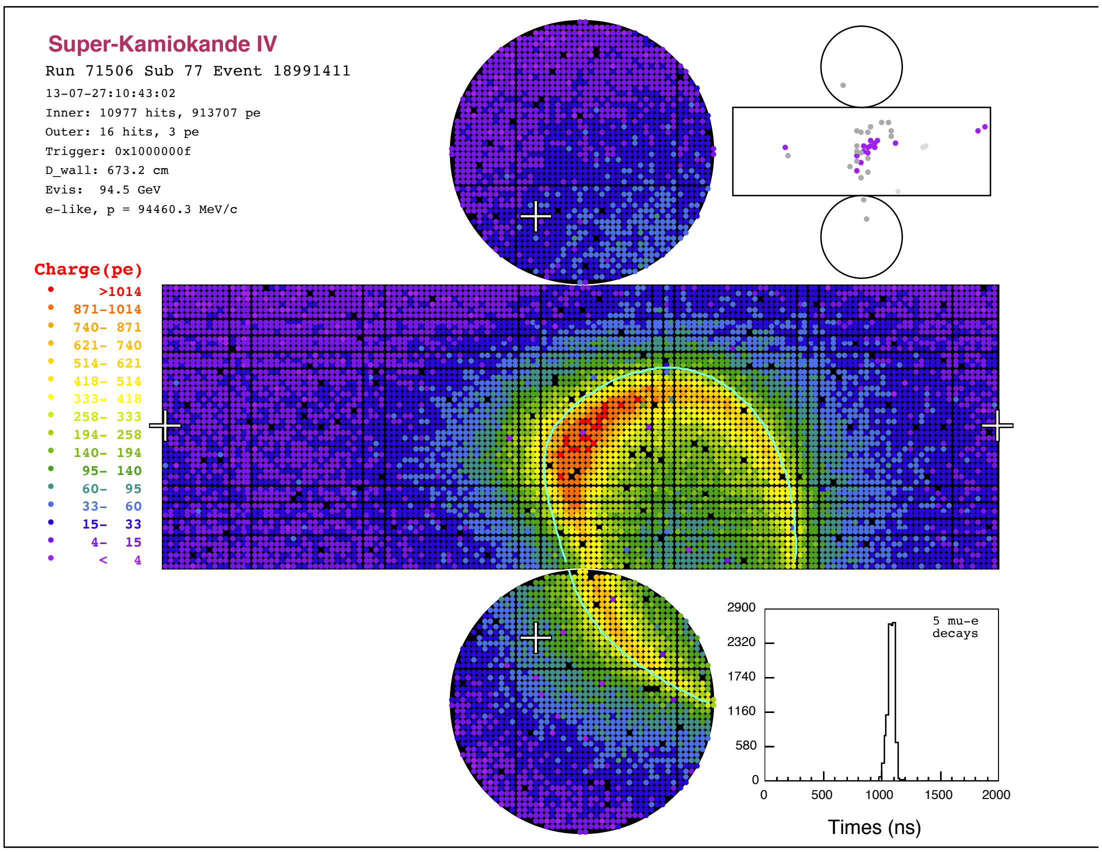

Figure 6.17: A 94.5 GeV single ring e-like event, from SK-IV FCFV data. This event has an OD trigger from the OD activity which closely follows the patter of high ID PMT activity.

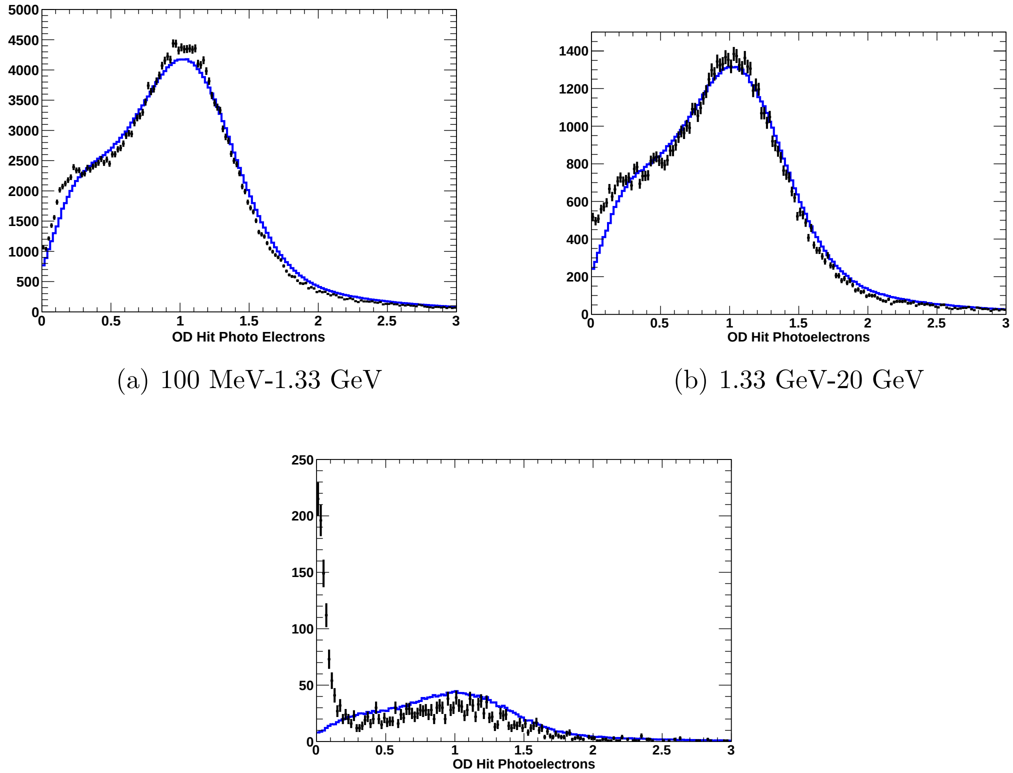

(a) 100 MeV-1.33 GeV

(b) 1.33 GeV-20 GeV

(c) $>$ 20 GeV

Figure 6.18: Number of p.e. in each OD hit. Black is SK-IV FCFV Data, blue is SK-IV FCFV atm MC. Note that Data-MC is relatively good for the 100 MeV-1.33 GeV and 1.33 GeV-20 GeV samples, but there is a dramatic spike at low p.e. in the $>$ 20 GeV sample. These additional low p.e. hits are due to ID-OD crosstalk.

OD hits were counted, I applied a threshold so that only OD hits of greater than 0.2 p.e. were included. Since some true OD hits will be removed by this threshold (see Fig. 6.18), I lowered the cut values based on OD hit counts by about 5%. I also calculated a modified version of nhitac that counted only OD hits greater than 0.2 pe. As a result 14 new FCFV events were found (3 new events pass the modified FC selection, and 11 events which passed the official FC selection but failed the final nhitac cut pass the modified nhitac cut). All events which passed the official FC reduction still passed the modified FC reduction. All new FCFV events included

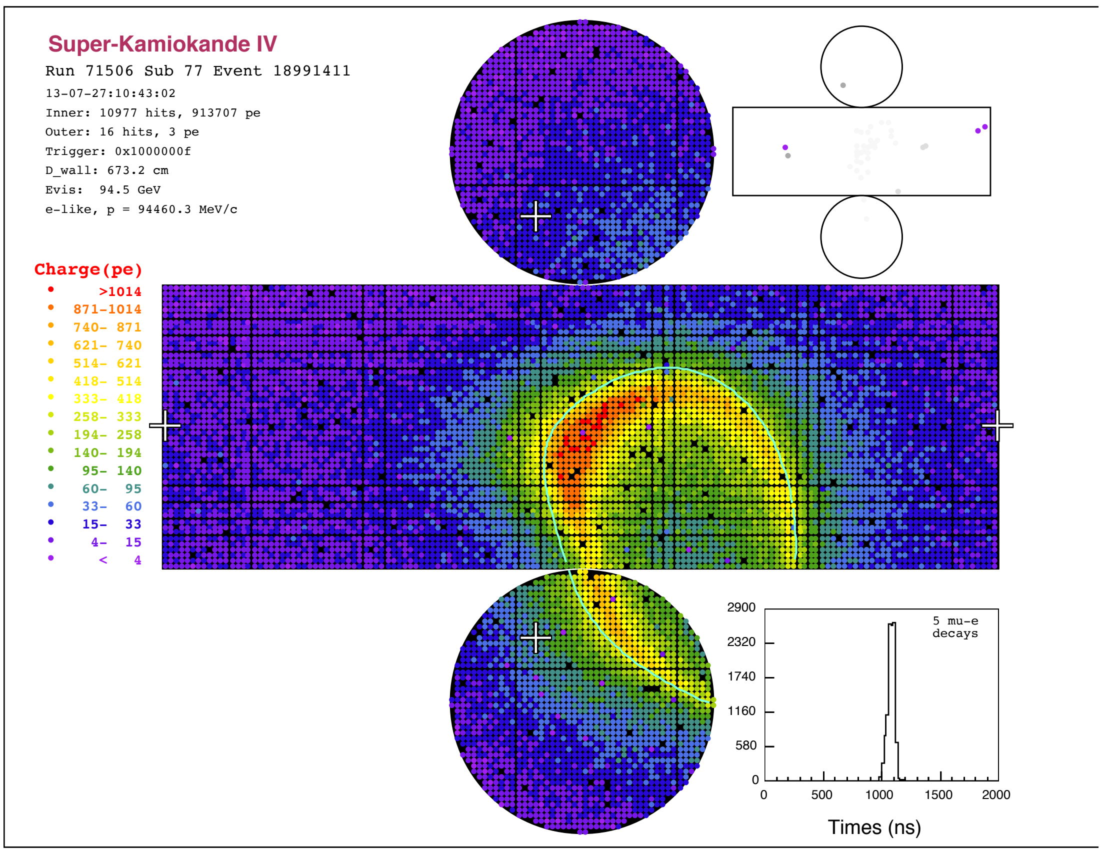

Figure 6.19: The same event as in Fig. 6.17, with OD hits of less than 0.2 p.e. removed. Note that the OD activity is now minimal. (Hits below 0.2 p.e. a visible in very light grey).

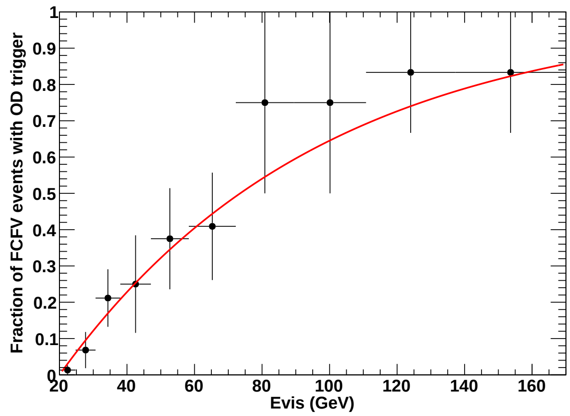

Figure 6.20: Fraction of events with OD trigger (and thus no neutron tagging available) as a function of visible energy. Fit is of form frac=$1 - \exp(-A(\text{evis} - 20GeV))$.

an OD trigger, which means that neutron tagging could not be performed on these events (see Section 2.5.2). Fig. 6.20 shows the approximate fraction of events on which neutron tagging can be performed, as a function of visible energy. The fraction is computed directly from data. Events for which neutron tagging is unavailable are considered signal if they pass the first three analysis cuts. This inability to perform neutron tagging on the highest energy events results in an increase in the expected background from 5.9 to 7.4 events over the entire sky for the $>$ 20 GeV sample. Of the 14 new FCFV events found, none passed all analysis cuts.

6.10 Selecting Opening Angles

Optimal cone angles were selected to maximize the Figure-of-Merit $\varepsilon/\sqrt{b}$, where ε is efficiency and b is background. For each combination of halo model and production method, the signal MC was reweighted assuming the direction of the scattered electron was the same as the direction of the boosted dark matter. The Figure-of-Merit is shown in Fig. 6.21. The optimal half-opening angle of the search cone was found to

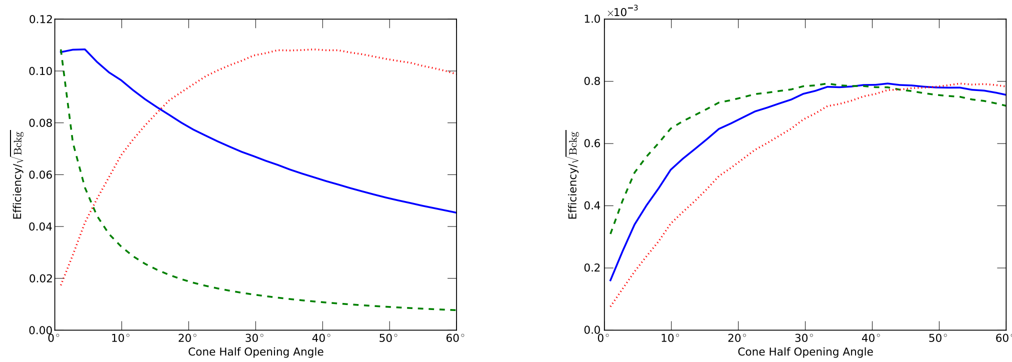

(a) Annihilation (b) Decay

Figure 6.21: Cone opening angle optimization for boosted dark matter from annihilation and decay. In both 6.21(a) and 6.21(b) the solid blue is the NFW halo model, dotted red is the Kravtsov halo model, and dashed green is the Moore halo model. Note since the scaling is arbitrary, the efficiencies have been scaled by different amounts for each model so that they can all be seen on the same plot.

range from less than 5° to around 40°, depending on halo model and boosted dark matter production method. We therefore used eight search cones around the Galactic Center, ranging from 5° to 40° in steps of 5°. When the Sun is the signal source the situation is much simpler, since it is effectively a point source. A single search cone of 5° around the Sun was this used for the solar search.

6.11 Background Estimation

A data-driven Away-From-Source (AFS) method was used to estimate background due to atmospheric neutrinos for the two lower energy samples. In order to avoid contamination from a potential signal, the AFS region is defined as everything outside an 80° cone for the Galactic Center search, and everything outside of the 5° search cone for the solar search. The AFS regions are defined, like the search cones, in celestial coordinates for the Galactic Center search, and solar coordinates for the

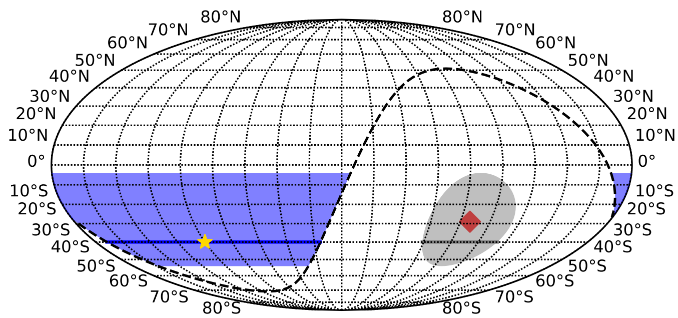

Figure 6.22: "Away From Source" (AFS) region shown in blue, and search cone shown in gray for a search cone of 25° half-opening angle around the galactic center. The red diamond it at the location of the galactic center. The dotted black line represents the 80° cone outside of which the AFS region is defined. For an event at the location of the yellow start, the weight for background estimation is the ratio of the gray arc to the blue arc.

Sun search. For a particular search cone, each data event in the AFS region can be assigned two values based on its direction in horizontal coordinates $\hat{d}$:

- T_{AFS} is the fraction of time $\hat{d}$ spends within the AFS region.
- T_{cone} is the fraction of time $\hat{d}$ spends within the search cone.

The event is then weighted by the ratio T_{cone}/T_{AFS}. The sum of these weights gives an estimate of the background in the search cone, while the square-root of the sum of the squares of the weights gives the uncertainty on this estimate. The background estimate "Away From Source" (AFS) region and search cone are shown for a 25° degree cone around the Galactic Center in Fig. 6.22.

The GC remains at the same declination at all times, and a single rotation of the Earth over the course of a day rotates horizontal coordinates in declination. The ratio

T_{cone}/T_{AFS} can therefore be calculated analytically for the GC search. It is it equal to the ratio of right ascensions spanned by the search cone to right ascensions spanned by the AFS region at a particular declination, which is visualized in Fig. 6.22. The details of this calculation can be found in Appendix A.

A similar technique could be applied to the search around the Sun. However the declination of the sun changes with time, and so the math becomes more complicated. Instead, a slightly different approach was taken. For an event in the AFS region, the correct weight to use for background estimation is the ratio of time that the horizontal coordinate direction of the event spends within the 5° search cone around the sun to the time it spends outside the search cone. These weights are calculated as follows:

- Directions in horizontal coordinates are divided into a grid of 1000 bins in azimuth by 600 bins in cosine zenith.

- The weight for events in each bin is computed by stepping through a year in steps of 1 second and counting up the amount of time each bin is within 5° of the sun.

The fraction of time spent within 5° of the sun as a function of cosine zenith and azimuth is shown in Fig. 6.23

For applications to the galactic center, and to the Sun, it is implicitly assumed that the detector has been run uniformly in time. This assumption could introduce error in the background estimates if instead the detector has run much more at certain times of the day or year than at others. Therefore, 500 years of atmospheric neutrino MC was used to test the validity of the AFS method. The time of each MC event was chosen from the times of real data events. The AFS method was applied to the MC, and the background estimate made by this method was compared to the number of events found in the search cone in the MC. If these numbers were found

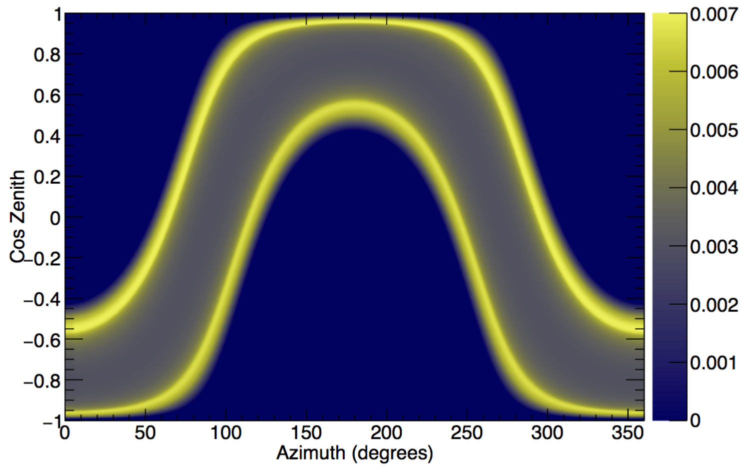

Figure 6.23: The fraction of time spent with 5° of the sun, as a function of cosine zenith and azimuth.

to be very different, it would indicate non-uniformity of the time when the detector has been run is leading to a bias in the AFS background estimate. As can be seen in Fig. 6.24, the difference is both statistically consistent with zero, and much smaller than the uncertainty in the AFS background estimates when applied to real data. Therefore, any potential bias in the AFS method introduced by non-uniform running of the detector can be ignored.

For the above 20 GeV event sample, there would be too few events in the AFS region for the above technique to work well. Instead, the MC estimate for the expected number of atmospheric neutrino events in the search cone was taken as the background estimate. The MC was livetime normalized and oscillated according to 3-flavor oscillations with oscillation parameters: $\Delta m^2_{23} = 2.5 \times 10^{-3}$ GeV^2, $\Delta m^2_{12} = 7.65 \times 10^{-5}$ GeV^2, $\sin^2\theta_{23} = 0.5875, \sin^2\theta_{13} = 0.0219, \sin^2\theta_{12} = 0.309, and \delta_{cp} = 4.19$. The systematic uncertainty on this estimate is found by summing in quadrature the effects of 1-σ shifts of all 75 official SK-IV systematics. The uncertainty of oscillation parameters were also included as systematics. Of these, only 18 cause more than a

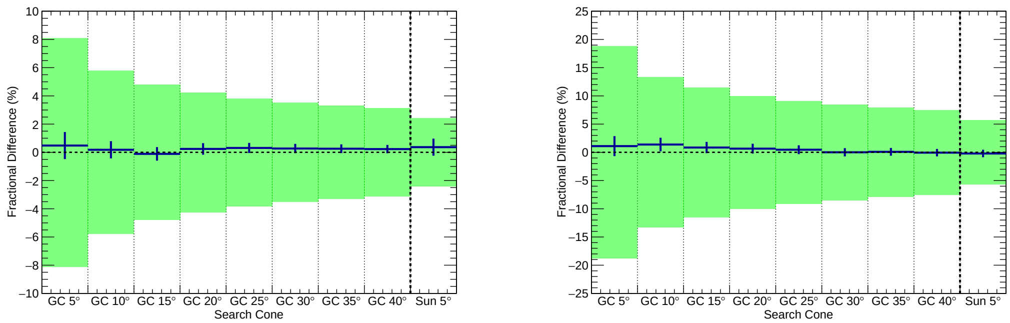

(a) Low Energy

(b) Mid Energy

Figure 6.24: Verification of AFS method. The blue histogram shows the fractional difference between the AFS background estimate when applied to MC and the actual number of events in the search cone in MC. The green shows the AFS background estimate uncertainty when applied to data.

1% shift in our background estimate at 1-σ. Uncertainties causing more than a 5% shift at 1-σ are shown in Table 6.4. The systematic uncertainty of the above 20 GeV sample is dominated by the systematic uncertainty of the neutron tagging cut. This accounts for the uncertainty in the efficiency of our neutron tagging algorithm, as well as the uncertainty in the production and transport of neutrons in the detector. It was estimated from a data-MC comparison of the fraction of events passing the first three selection cuts and having zero tagged neutrons, as a function of visible energy. Above about 10 GeV of visible energy, there are very low statistics for the data, and so a data-MC comparison is difficult to make. Therefore, above 3 GeV the data and MC were fit to logarithmic functions $A + B \log \frac{\mathrm{E_{vis}}}{\mathrm{GeV}}$, as shown in Fig. 6.25(a). The systematic uncetainty was then taken as the difference between the data fit and the MC fit in the region above 7.6 GeV of visible energy. The total uncertainty for the above 20 GeV event sample is 29.8%.

The background estimates for the samples below 20 GeV are compared to MC background estimates in Fig. 6.26. The systematic uncertainties on the MC background estimates for these samples were computed in the same way as for the above 20 GeV sample, resulting in uncertainties of 18.4% and 17.7%, respectively. As can be seen in Fig. 6.26, the two background estimation techniques agree with one another to within systematic uncertainties, and the systematic uncertainties on the AFS technique are much smaller than those on the MC based estimate.

Systematic	1-σ shift
Neutron Tagging Cut	23%
Normalization (Flux, Data reduction, FV)	11%
Energy Calibration	6%
Garczyk and Socyzk 1π axial coupling	5%

Table 6.4: Largest systematic uncertainty contributions for High Energy sample.

6.12 Analysis and Results

The results of the search are shown in Table 6.5 [112]. The observed data are consistent with expected background for both the Galactic Center and Sun searches. In the highest energy sample, the search is essentially background free, and no candidates were found in any of the search cones. Skymaps of the locations of every event passing the analysis cuts are provided for each energy sample in Figs. 6.27 and 6.28.

For each cone and energy sample, confidence intervals for the observed boosted dark matter event rate were computed using a Poisson χ^2 statistic that incorporates the systematic uncertainty on the background estimate through the pull method [13, 113]:

$$\chi^2(s) = \min_{\delta} \left[2 \left(E - \mathcal{O} + \mathcal{O} \ln \frac{\mathcal{O}}{E} \right) + \delta^2 \right], \tag{6.14}$$

where $E = b(1 + \delta\sigma) + s$, b is the estimated background with systematic uncertainty σ, s is the signal excess being tested, δ is the systematic pull that is minimized over,

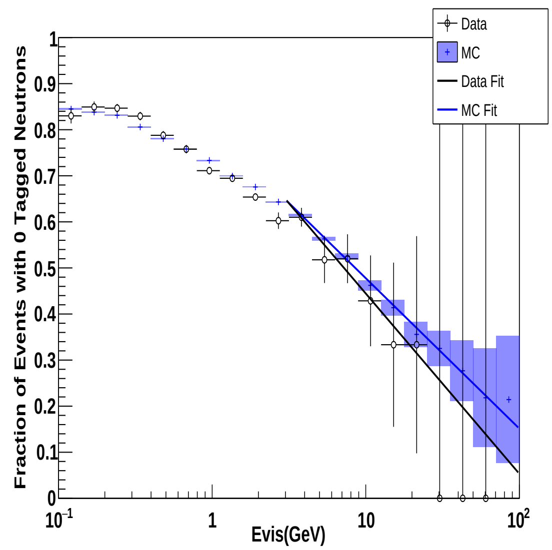

(a)

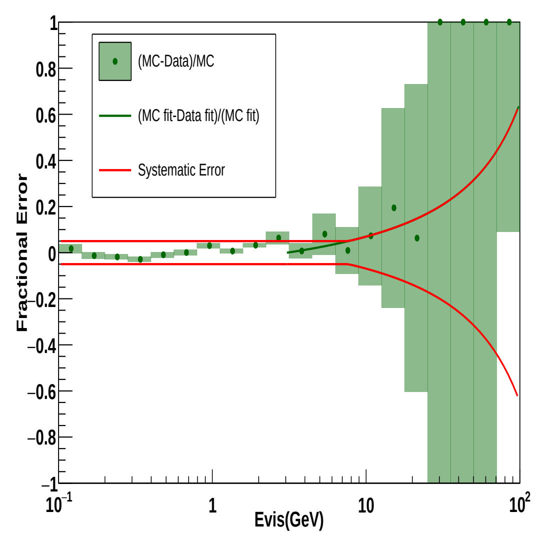

(b)

Figure 6.25: Neutron tagging cut systematic error estimation. 6.25(a) shows the fractional number of events passing the neutron tagging cut after passing all previous cuts for both Data and MC, along with logarithmic fits. The filled rectangles around the MC show statistical uncertainty in the MC. 6.25(b) shows the resulting systematic uncertainty, set to 5% below 7.6 GeV, and the difference in the two fits from 6.25(a) above 7.6 GeV.

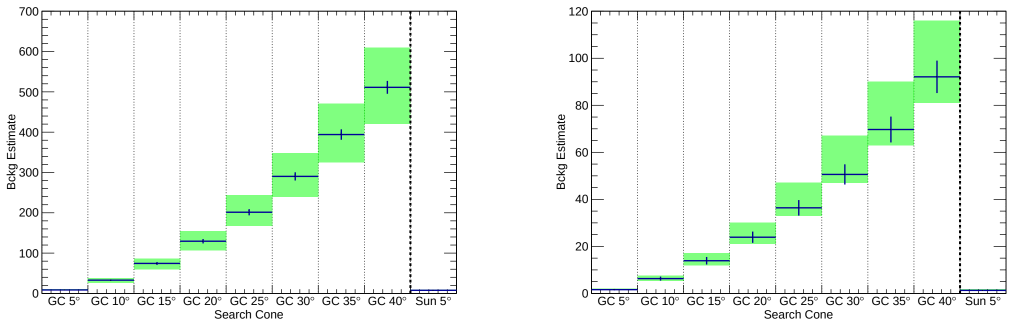

(a) Low Energy (b) Mid Energy

Figure 6.26: Comparison of AFS background estimates to MC background estimates for Low Energy and Mid Energy samples. The two background estimation techniques agree to within systematic uncertainties, and the AFS technique has much smaller systematic uncertainties.

and $\mathcal{O}$ is the observed number of events. The test statistic $\Delta\chi^2$ was calculated by subtracting the global minimum χ^2. The confidence levels to allow values of s were obtained by comparing the measured value of $\Delta\chi^2$ at a particular value of s to the $\Delta\chi^2$ distribution of a large number of toy MC produced assuming that level of signal. Since the $s = 0$ hypothesis is allowed at 90% confidence for all search cones and energy samples, the upper ends of the 90% confidence intervals are interpreted as 90% upper limits, and presented in Table 6.5.

To demonstrate the application of this result to a specific model, limits were calculated on the baseline boosted dark matter model described in Section 6.3, with the Galactic Center as the signal source. Limits were calculated for two scenarios of ψ_B production, one where ψ_B is produced through annihilation of ψ_A with $\bar{\psi}_A$, and another where ψ_B is produced through the decay of ψ_A. In the annihilation scenario, the thermal annihilation cross section is set to $\langle\sigma_{A\bar{A}\rightarrow B\bar{B}}v\rangle = 5\times10^{-26}$ cm^3/s in order to achieve the observed relic density $\Omega_A \approx 0.2$ through an assisted freeze out scenario [87, 95]. The energy of ψ_B is equal to m_A in this scenario. In the decay scenario, the

Search Cone	100 MeV< E_{vis} < 1.33 GeV Expected Bckg	Data	Sig Rate Limit $(\text{kT-y})^{-1}$	1.33 GeV < E_{vis} < 20 GeV Expected Bckg	Data	Sig Rate Limit $(\text{kT-y})^{-1}$
GC 5°	8.4 ± 0.7	5	0.017	1.6 ± 0.3	1	0.018
GC 10°	32.0 ± 1.9	24	0.023	6.3 ± 0.84	5	0.026
GC 15°	72.5 ± 3.5	69	0.078	13.6 ± 1.6	11	0.032
GC 20°	126.5 ± 5.4	125	0.123	23.3 ± 2.3	18	0.028
GC 25°	196.8 ± 7.6	202	0.201	35.4 ± 3.3	31	0.049
GC 30°	283.7 ± 10.1	285	0.214	49.3 ± 4.3	48	0.081
GC 35°	384.8 ± 12.8	375	0.187	68.1 ± 5.4	67	0.101
GC 40°	499.6 ± 15.9	494	0.249	90.2 ± 6.9	90	0.124
Sun 5°	7.59 ± 0.18	5	0.017	1.25 ± 0.07	1	0.015

Search Cone	$E_{vis} > 20$ GeV Expected Bckg	Data	Sig Rate Limit $(\text{kT-y})^{-1}$
GC 5°	0.016 ± 0.005	0	0.015
GC 10°	0.060 ± 0.018	0	0.015
GC 15°	0.14 ± 0.04	0	0.014
GC 20°	0.25 ± 0.07	0	0.014
GC 25°	0.37 ± 0.11	0	0.013
GC 30°	0.53 ± 0.16	0	0.012
GC 35°	0.70 ± 0.21	0	0.011
GC 40°	0.90 ± 0.27	0	0.011
Sun 5°	0.015 ± 0.004	0	0.015

Table 6.5: Estimated backgrounds,numbers of events in data, and signal event rate limits for each cone and each energy sample. The event rate limits are at the 90% confidence level.

decay lifetime of ψ_A, τ_{decay}, is taken to be a free parameter, and the energy of ψ_B is assumed to be $m_A/2$.

Limits were calculated separately for the Moore, NFW, and Kravtsov Galactic halo models, using the results from a different cone for each fit. For the annihilation scenario, the 5° cone was used for the Moore model, the 10° cone for the NFW model, and the 40° cone for the Kravtsov model. For the decay scenario, the 40° cone was

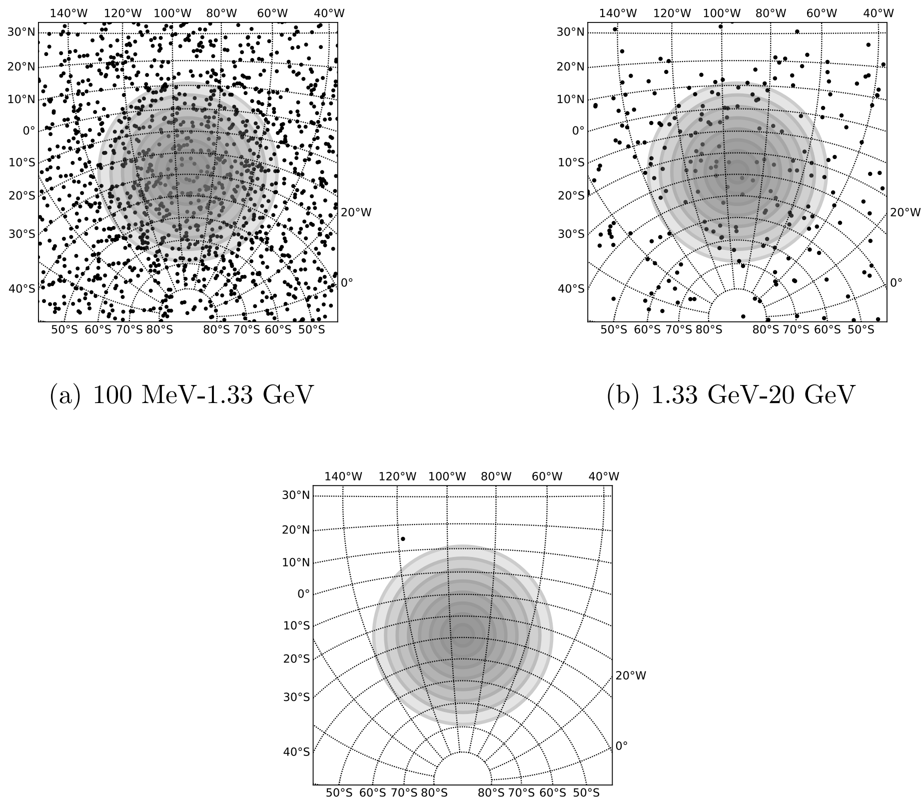

(a) 100 MeV-1.33 GeV

(b) 1.33 GeV-20 GeV

(c) > 20 GeV

Figure 6.27: Location of all events passing analysis cuts near the galactic center. The 8 grey circles show the 8 cones around the galactic center used in the analysis.

used for all three galactic halo models. These cones were selected using the cone optimization technique described earlier. For each halo model, signal MC events were reweighted based on the values of $m_A, m_B, m_{\gamma'}, \varepsilon$ and g' at the particular point in parameter space being tested. This reweighting accounts for the model-dependent recoil electron energy spectrum, as well as the model-dependent smearing between the boosted dark matter direction and the recoil electron direction. The effect of boosted dark matter scattering off both electrons and protons in the Earth is also accounted for, though this effect is negligible for the majority of the allowed parameter space.

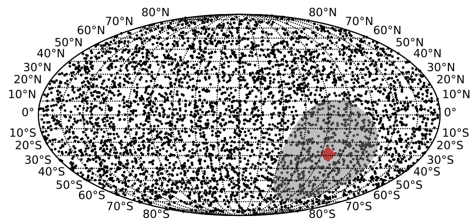

(a) 100 MeV-1.33 GeV

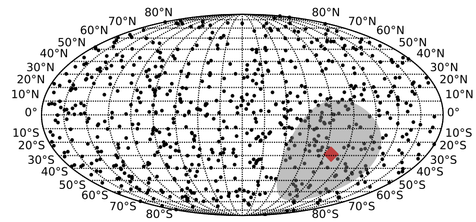

(b) 1.33 GeV-20 GeV

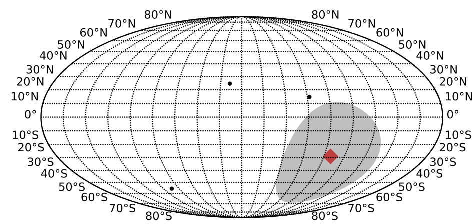

(c) > 20 GeV

Figure 6.28: Location of all events passing analysis cuts. The grey shows a 40° cone around the galactic center, which is shown by the red diamond

A binned χ^2 statistic was then computed similar to the one described above:

$$\chi^2 = \sum_i^3 \min_{\delta_i} \left[2 \left(E_i - \mathcal{O}_i + \mathcal{O}_i \ln \frac{\mathcal{O}_i}{E_i} \right) + \delta_i^2 \right], \tag{6.15}$$

with variables defined as before, summed over three bins corresponding to the three energy samples. The $\Delta\chi^2$ test statistic was then calculated by subtracting the global minimum χ^2. Confidence intervals were found by comparing the measured $\Delta\chi^2$ values with the distributions of $\Delta\chi^2$ values found by many toy Monte Carlo simulations produced at each point. Ninety-percent confidence intervals were computed in the ε

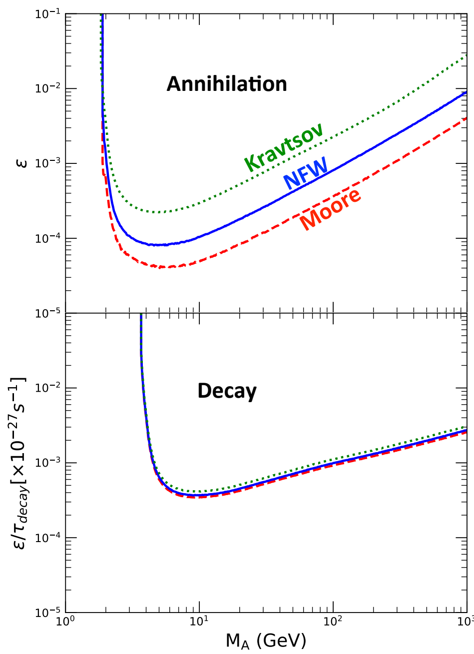

Figure 6.29: 90% Confidence Interval upper limits for m_B=200 MeV, m'_γ=20 MeV, and g'=0.5, for boosted dark matter produced by annihilation (top) and decay (bottom).

vs m_A plane for the annihilation scenario, and the ε/τ_{decay} vs m_A plane for the decay scenario, with m_B, m'_γ and g' set to representative values of m_B=200 MeV, m'_γ=20 MeV, and g'=0.5. Since the $\varepsilon = 0$ points, which correspond to no signal, are allowed at 90% confidence, the resulting confidence intervals are interpreted as upper limits. These limits are shown for the Moore, NFW, and Kravtsov halo models in Fig. 6.29.

Chapter 7

Conclusion

Pauli's neutrino and Zwicky's dark matter have led very different experimental lives. While the neutrino was experimentally observed about 20 years after its proposal, and its properties are now fairly well understood, dark matter remains one of the most mysterious aspects of the Universe. In this thesis, I have added to our confidence in our understanding of neutrinos by showing for the first time that atmospheric neutrino oscillations at Super-Kamiokande show evidence of Earth matter effects, in line with theoretical expectations. The observation of Earth matter effects in atmospheric neutrinos is an important step towards measuring neutrino mass hierarchy, since the sensitivity of atmospheric neutrinos to mass hierarchy is a result of Earth matter effects. I have also searched for a relatively newly proposed class of dark matter, called boosted dark matter, by looking for excess events which could be electrons elastically scattered by boosted dark matter coming from the Galactic Center or Sun. The lack of any excess reported herein represents the first experimental search for this class of boosted dark matter, and constrains boosted dark matter theories, helping to narrow down the list of dark matter candidates.

Expectations[1] about the future experimental stories of neutrinos and dark matter are also divergent. The next generation of neutrino experiments seems likely to largely resolve the major remaining mysteries of neutrinos in the next 10 to 20 years. Non-gravitational observation of dark matter, on the other hand, could happen in the next few years, or could still be a dream half a century from now.

A nice analogy for the two situations is two different parties with a piñata at each. At one party, we've found the piñata, and are now in the process of knocking it down to find out exactly what type of candy is inside. At the other party, we are wandering blindfolded around a room swinging a bat, because we are pretty certain there is a piñata somewhere in here. Thank goodness there will be candy when we finally find it!

[1] mine, at least

Appendix A

Calculation of Weights for Galactic Center Background

As stated in Section 6.11, for the GC background calculation, the weight of each event in the AFS region is equal to the ratio of right ascensions spanned by the search cone to right ascensions spanned by the AFS region at that declination, which is visualized in Fig. A.1(a).

This weight can be written in terms of the variables in Figure A.1(b) as $w = \frac{\alpha_{\mathrm{cone}}}{\pi - \alpha_{\mathrm{AFS}}}$. To compute α_{cone} and α_{AFS}, the points must be found where a cone of half opening angle θ centered on the direction to the galactic center, a plane at declination ϕ_{dec}, and the unit sphere intersect. (The directions are without loss of generality assumed to be unit vectors, thus the inclusion of the unit sphere requirement). In Fig. A.1(a), for the AFS region (GC search cone), these points are at the intersection of the blue (gray) cone, pink plane, and the circle drawn on the plane. The circle in Fig. A.1(b) is the intersection of the plane and the unit sphere, and so $r_{\mathrm{dec}} = \cos\phi_{\mathrm{dec}}$. Defining the x-axis as pointing toward the right ascension of the galactic center at declination 0, the z-axis as extending from the poles of the earth so that $+\hat{z}$

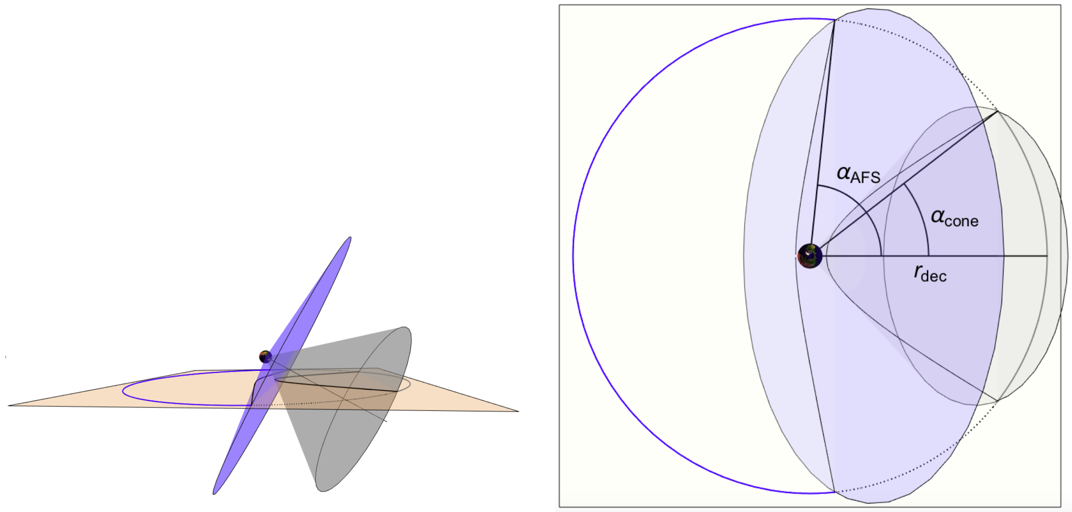

(a) (b)

Figure A.1: Visualization of the event weighting for background estimation. An event found in the AFS region at the declination respresented by the plane is weighted by the ratio of the gray arc to the blue arc. Figure A.1(b) shows Figure A.1(a) as seen from directly above.

correspondes with a declination of 90° and -$\hat{z}$ with a declination of -90°, and the y-axis accordingly to keep the coordinate system right handed, we can write the position of the two intersection points as:

$$\hat{v}_{\pm} = (x', \pm y', z') \tag{A.1}$$

and the Galactic Center direction as:

$$\hat{v}_{\mathrm{GC}} = (\cos(-29°), 0, \sin(-29°)) \tag{A.2}$$

Since $\hat{v}_{\pm}$ are on the plane at declination ϕ_{dec} we have:

$$z' = \sin \phi_{\mathrm{dec}} \tag{A.3}$$

Additionally, since $\hat{v}_\pm$ are on the cone of half opening angle θ around the Galactic Center we have

$$\frac{|\hat{v}_\pm - (\hat{v}_\pm \cdot \hat{v}_{\mathrm{GC}})\hat{v}_{\mathrm{gc}}|}{|(\hat{v}_\pm \cdot \hat{v}_{\mathrm{GC}})\hat{v}_{\mathrm{GC}}|} = \tan\theta \tag{A.4}$$

$$\hat{v}_\pm \cdot \hat{v}_{\mathrm{GC}} > 0 \tag{A.5}$$

Solving Equation A.4 under the condition of Equation A.5, we have:

$$\frac{\sqrt{(\hat{v}_\pm - (\hat{v}_\pm \cdot \hat{v}_{\mathrm{GC}})\hat{v}_{\mathrm{GC}}) \cdot (\hat{v}_\pm - (\hat{v}_\pm \cdot \hat{v}_{\mathrm{GC}})\hat{v}_{\mathrm{GC}})}}{\sqrt{((\hat{v}_\pm \cdot \hat{v}_{\mathrm{GC}})\hat{v}_{\mathrm{GC}}) \cdot ((\hat{v}_\pm \cdot \hat{v}_{\mathrm{GC}})\hat{v}_{\mathrm{GC}})}} = \tan\theta \tag{A.6}$$

$$\frac{\sqrt{\hat{v}_\pm \cdot \hat{v}_\pm + (\hat{v}_{\mathrm{GC}} \cdot \hat{v}_{\mathrm{GC}} - 2)(\hat{v}_\pm \cdot \hat{v}_{\mathrm{GC}})^2}}{\sqrt{(\hat{v}_\pm \cdot \hat{v}_{\mathrm{GC}})^2 \hat{v}_{\mathrm{GC}} \cdot \hat{v}_{\mathrm{GC}}}} = \tan\theta \tag{A.7}$$

$$\frac{\sqrt{1 - (\hat{v}_\pm \cdot \hat{v}_{\mathrm{GC}})^2}}{\hat{v}_\pm \cdot \hat{v}_{\mathrm{GC}}} = \tan\theta \tag{A.8}$$

$$1 - (\hat{v}_\pm \cdot \hat{v}_{\mathrm{GC}})^2 = \tan^2\theta (\hat{v}_\pm \cdot \hat{v}_{\mathrm{GC}})^2 \tag{A.9}$$

$$\hat{v}_\pm \cdot \hat{v}_{\mathrm{GC}} = \sqrt{\frac{1}{1+\tan^2\theta}} \tag{A.10}$$

$$x' \cos(-29^\circ) + \sin\phi_{dec} \sin(-29^\circ) = \sqrt{\frac{1}{1+\tan^2\theta}} \tag{A.11}$$

$$x' = \frac{-\sin\phi_{dec}\sin(-29^\circ) + \sqrt{\frac{1}{1+\tan^2\theta}}}{\cos(-29^\circ)} \tag{A.12}$$

where we have used the fact that $(\hat{v}_{\mathrm{GC}} \cdot \hat{v}_{\mathrm{GC}}) = (\hat{v}_\pm \cdot \hat{v}_\pm) = 1$. The angle α is then found as

$$\cos\alpha = \frac{x'}{r_{\mathrm{dec}}} = \frac{-\sin\phi_{dec}\sin(-29^\circ) + \sqrt{\frac{1}{1+\tan^2\theta}}}{\cos(-29^\circ)\cos\phi_{\mathrm{dec}}} \tag{A.13}$$

The weight for an event in the AFS region at declination ϕ_{dec} can thus be found as

$$w(\phi_{\text{dec}}) = \frac{\alpha_{\text{cone}}}{\pi - \alpha_{\text{AFS}}} \tag{A.14}$$

$$\cos\alpha_{\text{cone}} = \frac{-\sin\phi_{dec}\sin(-29^\circ) + \sqrt{\frac{1}{1+\tan^2\theta_{\text{cone}}}}}{\cos(-29^\circ)\cos\phi_{\text{dec}}} \tag{A.15}$$

$$\cos\alpha_{\text{AFS}} = \frac{-\sin\phi_{dec}\sin(-29^\circ) + \sqrt{\frac{1}{1+\tan^2\theta_{\text{AFS}}}}}{\cos(-29^\circ)\cos\phi_{\text{dec}}} \tag{A.16}$$

The background estimate and uncertainty on the estimate are then

$$B_{\text{est}} = \sum_i w(\phi_{\text{dec},i}) \tag{A.17}$$

$$\sigma B_{\text{est}} = \sqrt{\sum_i w^2(\phi_{\text{dec},i})}. \tag{A.18}$$

Bibliography

[1] P. A. R. Ade *et al.* (Planck), Astron. Astrophys. **594**, A13 (2016), arXiv:1502.01589 [astro-ph.CO] .

[2] G. Hinshaw *et al.* (WMAP), Astrophys. J. Suppl. **208**, 19 (2013), arXiv:1212.5226 [astro-ph.CO] .

[3] L. M. Brown, Phys. Today **31N9**, 23 (1978).

[4] E. Fermi, Z. Phys. **88**, 161 (1934).

[5] F. Zwicky, Helv. Phys. Acta **6**, 110 (1933), [Gen. Rel. Grav.41,207(2009)].

[6] F. Reines and C. L. Cowan, Phys. Rev. **92**, 830 (1953).

[7] C. L. Cowan, F. Reines, F. B. Harrison, H. W. Kruse, and A. D. McGuire, Science **124**, 103 (1956).

[8] F. Reines and C. L. Cowan, Nature **178**, 446 (1956).

[9] Y. Fukuda *et al.* (Super-Kamiokande), *Advanced computing and analysis techniques in physics research. Proceedings, 8th International Workshop, ACAT 2002, Moscow, Russia, June 24-28, 2002*, Nucl. Instrum. Meth. **A501**, 418 (2003).

[10] K. Abe *et al.*, Nucl. Instrum. Meth. **A737**, 253 (2014), arXiv:1307.0162 [physics.ins-det] .

[11] E. Kearns, T. Kajita, and Y. Totsuka, Sci. Am. **281N2**, 48 (1999), [Spektrum Wiss. Dossier2003N1,64(2003)].

[12] J. D. Jackson, *Classical Electrodynamics* (Wiley, 1998).

[13] C. Patrignani *et al.* (Particle Data Group), Chin. Phys. **C40**, 100001 (2016).

[14] P. Mijakowski, *Direct and Indirect Search for Dark Matter*, Ph.D. thesis, Warsaw, Inst. Nucl. Studies (2011).

[15] A. Suzuki, M. Mori, K. Kaneyuki, T. Tanimori, J. Takeuchi, H. Kyushima, and Y. Ohashi, Nucl. Instrum. Meth. **A329**, 299 (1993).

[16] S. Yamada *et al.* (Super-Kamiokande), *Real time. Proceedings, 16th Conference on Computing Applications in Nuclear and Plasma Sciences, RT2009, Beijing, P.R. China, May 10-15, 2009*, IEEE Trans. Nucl. Sci. **57**, 428 (2010).

[17] H. Nishino, K. Awai, Y. Hayato, S. Nakayama, K. Okumura, M. Shiozawa, A. Takeda, K. Ishikawa, A. Minegishi, and Y. Arai, Nucl. Instrum. Meth. **A610**, 710 (2009), arXiv:0911.0986 [physics.ins-det] .

[18] J. Gustafson, *A Search for Baryon Number Violation by Two Units at the Superk-Kamiokande Detector*, Ph.D. thesis, Boston U. (2016).

[19] E. Richard, *Studies of the Energy, Azimuthal, and Time Spectra of the Atmospheric Neutrino Flux at Super-Kamiokande*, Ph.D. thesis, Tokyo U. (2015).

[20] F. Dufour, *Precise Study of the Atmospheric Neutrino Oscillation Pattern Using Super-Kamiokande I and II*, Ph.D. thesis, Brussels U. (2009).

[21] Y. Takenaga, *Atmospheric neutrino oscillation analysis with solar terms in Super-Kamiokande*, Ph.D. thesis, Tokyo U. (2008).

[22] S. Tobayama, *An Analysis of the Oscillation of Atmospheric Neutrinos*, Ph.D. thesis, British Columbia U. (2016).

[23] D. Cokinos and E. Melkonian, Phys. Rev. **C15**, 1636 (1977).

[24] T. J. Irvine, *Development of Neutron-Tagging Techniques and Application to Atmospheric Neutrino Oscillation Analysis in Super-Kamiokande*, Ph.D. thesis, U. Tokyo (main) (2014).

[25] R. Brun and F. Rademakers, *New computing techniques in physics research V. Proceedings, 5th International Workshop, AIHENP '96, Lausanne, Switzerland, September 2-6, 1996*, Nucl. Instrum. Meth. **A389**, 81 (1997).

[26] ROOT, "Tmultilayerperceptron — root," [Online; accessed 3-November-2017].

[27] B. Pontecorvo, Sov. Phys. JETP **26**, 984 (1968).

[28] Z. Maki, M. Nakagawa, and S. Sakata, Prog. Theor. Phys. **28**, 870 (1962).

[29] A. G. Cohen, S. L. Glashow, and Z. Ligeti, Phys. Lett. **B678**, 191 (2009), arXiv:0810.4602 [hep-ph] .

[30] K. Abe *et al.* (Super-Kamiokande), Phys. Rev. **D97**, 072001 (2018), arXiv:1710.09126 [hep-ex] .

[31] T. Kajita, E. Kearns, and M. Shiozawa (Super-Kamiokande), Nucl. Phys. **B908**, 14 (2016).

[32] P. Adamson *et al.* (MINOS), Phys. Rev. Lett. **110**, 251801 (2013), arXiv:1304.6335 [hep-ex] .

[33] M. G. Aartsen *et al.* (IceCube), Phys. Rev. Lett. **111**, 081801 (2013), arXiv:1305.3909 [hep-ex] .

[34] M. H. Ahn *et al.* (K2K), Phys. Rev. **D74**, 072003 (2006), arXiv:hep-ex/0606032 [hep-ex] .

[35] P. Adamson *et al.* (MINOS), Phys. Rev. Lett. **101**, 131802 (2008), arXiv:0806.2237 [hep-ex] .

[36] K. Abe *et al.* (T2K), Phys. Rev. **D91**, 072010 (2015), arXiv:1502.01550 [hep-ex] .

[37] P. Adamson *et al.* (NOvA), Phys. Rev. Lett. **118**, 151802 (2017), arXiv:1701.05891 [hep-ex] .

[38] P. Adamson *et al.* (NOvA), Phys. Rev. Lett. **116**, 151806 (2016), arXiv:1601.05022 [hep-ex] .

[39] N. Agafonova *et al.* (OPERA), Phys. Rev. Lett. **115**, 121802 (2015), arXiv:1507.01417 [hep-ex] .

[40] F. P. An *et al.* (Daya Bay), Phys. Rev. Lett. **115**, 111802 (2015), arXiv:1505.03456 [hep-ex] .

[41] J. K. Ahn *et al.* (RENO), Phys. Rev. Lett. **108**, 191802 (2012), arXiv:1204.0626 [hep-ex] .

[42] Y. Abe *et al.* (Double Chooz), JHEP **10**, 086 (2014), [Erratum: JHEP02,074(2015)], arXiv:1406.7763 [hep-ex] .

[43] S. Abe *et al.* (KamLAND), Phys. Rev. Lett. **100**, 221803 (2008), arXiv:0801.4589 [hep-ex] .

[44] K. Abe *et al.* (Super-Kamiokande), Phys. Rev. **D94**, 052010 (2016), arXiv:1606.07538 [hep-ex] .

[45] B. Aharmim *et al.* (SNO), Phys. Rev. **C72**, 055502 (2005), arXiv:nucl-ex/0502021 [nucl-ex] .

[46] V. N. Aseev *et al.* (Troitsk), Phys. Rev. **D84**, 112003 (2011), arXiv:1108.5034 [hep-ex] .

[47] A. Aguilar-Arevalo *et al.* (LSND), Phys. Rev. **D64**, 112007 (2001), arXiv:hep-ex/0104049 [hep-ex] .

[48] A. A. Aguilar-Arevalo *et al.* (MiniBooNE), Phys. Rev. Lett. **98**, 231801 (2007), arXiv:0704.1500 [hep-ex] .

[49] V. D. Barger, K. Whisnant, S. Pakvasa, and R. J. N. Phillips, Phys. Rev. **D22**, 2718 (1980).

[50] H. A. Bethe, Phys. Rev. Lett. **56**, 1305 (1986), [,324(1986)].

[51] S. K. Agarwalla, Y. Kao, and T. Takeuchi, JHEP **04**, 047 (2014), arXiv:1302.6773 [hep-ph] .

[52] M. Honda, M. Sajjad Athar, T. Kajita, K. Kasahara, and S. Midorikawa, Phys. Rev. **D92**, 023004 (2015), arXiv:1502.03916 [astro-ph.HE] .

[53] R. P. Feynman, M. Kislinger, and F. Ravndal, Phys. Rev. **D3**, 2706 (1971).

[54] D. Rein, Z. Phys. **C35**, 43 (1987).

[55] D. Rein and L. M. Sehgal, Annals Phys. **133**, 79 (1981).

[56] C. Zeitnitz and T. A. Gabriel, Nucl. Instrum. Meth. **A349**, 106 (1994).

[57] A. M. Dziewonski and D. L. Anderson, Physics of the Earth and Planetary Interiors **25**, 297 (1981).

[58] G. L. Fogli, E. Lisi, A. Marrone, and A. Palazzo, Phys. Lett. **B583**, 149 (2004), arXiv:hep-ph/0309100 [hep-ph] .

[59] G. L. Fogli, E. Lisi, A. Palazzo, and A. M. Rotunno, Phys. Rev. **D67**, 073001 (2003), arXiv:hep-ph/0211414 [hep-ph] .

[60] A. Renshaw *et al.* (Super-Kamiokande), Phys. Rev. Lett. **112**, 091805 (2014), arXiv:1312.5176 [hep-ex] .

[61] V. C. Rubin, N. Thonnard, and W. K. Ford, Jr., Astrophys. J. **238**, 471 (1980).

[62] G. Bertone, D. Hooper, and J. Silk, Phys. Rept. **405**, 279 (2005), arXiv:hep-ph/0404175 [hep-ph] .

[63] K. G. Begeman, A. H. Broeils, and R. H. Sanders, Mon. Not. Roy. Astron. Soc. **249**, 523 (1991).

[64] D. Clowe, M. Bradac, A. H. Gonzalez, M. Markevitch, S. W. Randall, C. Jones, and D. Zaritsky, Astrophys. J. **648**, L109 (2006), arXiv:astro-ph/0608407 [astro-ph] .

[65] P. Tisserand *et al.* (EROS-2), Astron. Astrophys. **469**, 387 (2007), arXiv:astro-ph/0607207 [astro-ph] .

[66] L. Wyrzykowski *et al.*, Mon. Not. Roy. Astron. Soc. **416**, 2949 (2011), arXiv:1106.2925 [astro-ph.GA] .

[67] C. Alcock *et al.* (MACHO), Astrophys. J. **542**, 281 (2000), arXiv:astro-ph/0001272 [astro-ph] .

[68] D. S. Akerib *et al.* (LUX), Phys. Rev. Lett. **112**, 091303 (2014), arXiv:1310.8214 [astro-ph.CO] .

[69] Z. Ahmed *et al.* (CDMS-II), Science **327**, 1619 (2010), arXiv:0912.3592 [astro-ph.CO] .

[70] E. Aprile *et al.* (XENON100), Phys. Rev. Lett. **109**, 181301 (2012), arXiv:1207.5988 [astro-ph.CO] .

[71] S. Desai *et al.* (Super-Kamiokande), Phys. Rev. **D70**, 083523 (2004), [Erratum: Phys. Rev.D70,109901(2004)], arXiv:hep-ex/0404025 [hep-ex] .

[72] M. Rameez and T. Montaruli (IceCube), *Proceedings, 34th International Cosmic Ray Conference (ICRC 2015): The Hague, The Netherlands, July 30-August 6, 2015*, PoS **ICRC2015**, 1209 (2016).

[73] S. Adrian-Martinez *et al.* (ANTARES), JCAP **1311**, 032 (2013), arXiv:1302.6516 [astro-ph.HE] .

[74] G. Aad *et al.* (ATLAS), Eur. Phys. J. **C75**, 299 (2015), [Erratum: Eur. Phys. J.C75,no.9,408(2015)], arXiv:1502.01518 [hep-ex] .

[75] V. Khachatryan *et al.* (CMS), Eur. Phys. J. **C75**, 235 (2015), arXiv:1408.3583 [hep-ex] .

[76] C. Kraus *et al.*, Eur. Phys. J. **C40**, 447 (2005), arXiv:hep-ex/0412056 [hep-ex] .

[77] P. B. Pal and L. Wolfenstein, Phys. Rev. **D25**, 766 (1982).

[78] E. Bulbul, M. Markevitch, A. Foster, R. K. Smith, M. Loewenstein, and S. W. Randall, Astrophys. J. **789**, 13 (2014), arXiv:1402.2301 [astro-ph.CO] .

[79] A. Boyarsky, O. Ruchayskiy, D. Iakubovskyi, and J. Franse, Phys. Rev. Lett. **113**, 251301 (2014), arXiv:1402.4119 [astro-ph.CO] .

[80] R. D. Peccei and H. R. Quinn, Phys. Rev. **D16**, 1791 (1977).

[81] S. Weinberg, Phys. Rev. Lett. **40**, 223 (1978).

[82] F. Wilczek, Phys. Rev. Lett. **40**, 279 (1978).

[83] P. Sikivie, *11th International Symposium on Lepton and Photon Interactions at High Energies Ithaca, New York, August 4-9, 1983*, Phys. Rev. Lett. **51**, 1415 (1983), [Erratum: Phys. Rev. Lett.52,695(1984)].

[84] R. Ballou *et al.* (OSQAR), Phys. Rev. **D92**, 092002 (2015), arXiv:1506.08082 [hep-ex] .

[85] S. Andriamonje *et al.* (CAST), JCAP **0704**, 010 (2007), arXiv:hep-ex/0702006 [hep-ex] .

[86] S. J. Asztalos *et al.* (ADMX), Phys. Rev. Lett. **104**, 041301 (2010), arXiv:0910.5914 [astro-ph.CO] .

[87] K. Agashe, Y. Cui, L. Necib, and J. Thaler, JCAP **1410**, 062 (2014), arXiv:1405.7370 [hep-ph] .

[88] J. Huang and Y. Zhao, JHEP **02**, 077 (2014), arXiv:1312.0011 [hep-ph] .

[89] J. F. Cherry, M. T. Frandsen, and I. M. Shoemaker, Physical Review Letters **114**, 231303 (2015).

[90] A. Bhattacharya, R. Gandhi, and A. Gupta, JCAP **1503**, 027 (2015), arXiv:1407.3280 [hep-ph] .

[91] J. Kopp, J. Liu, and X.-P. Wang, Journal of High Energy Physics **2015**, 105 (2015).

[92] K. Kong, G. Mohlabeng, and J.-C. Park, Physics Letters B **743**, 256 (2015).

[93] J. Berger, Y. Cui, and Y. Zhao, Journal of Cosmology and Astroparticle Physics **2014**, 062 (2014).

[94] F. D'Eramo and J. Thaler, JHEP **06**, 109 (2010), arXiv:1003.5912 [hep-ph] .

[95] G. Belanger and J.-C. Park, JCAP **1203**, 038 (2012), arXiv:1112.4491 [hep-ph] .

[96] H. S. Cheon, S. K. Kang, and C. S. Kim, Phys. Lett. **B675**, 203 (2009), [Erratum: Phys. Lett.B698,324(2011)], arXiv:0807.0981 [hep-ph] .

[97] T. Hambye, JHEP **01**, 028 (2009), arXiv:0811.0172 [hep-ph] .

[98] T. Hambye and M. H. G. Tytgat, Phys. Lett. **B683**, 39 (2010), arXiv:0907.1007 [hep-ph] .

[99] C. Arina, T. Hambye, A. Ibarra, and C. Weniger, JCAP **1003**, 024 (2010), arXiv:0912.4496 [hep-ph] .

[100] G. Belanger, K. Kannike, A. Pukhov, and M. Raidal, JCAP **1204**, 010 (2012), arXiv:1202.2962 [hep-ph] .

[101] E. D. Carlson, M. E. Machacek, and L. J. Hall, Astrophys. J. **398**, 43 (1992).

[102] A. A. de Laix, R. J. Scherrer, and R. K. Schaefer, Astrophys. J. **452**, 495 (1995), arXiv:astro-ph/9502087 [astro-ph] .

[103] Y. Hochberg, E. Kuflik, T. Volansky, and J. G. Wacker, Phys. Rev. Lett. **113**, 171301 (2014), arXiv:1402.5143 [hep-ph] .

[104] D. Kim, J.-C. Park, and S. Shin, (2016), arXiv:1612.06867 [hep-ph] .

[105] A. Bhattacharya, R. Gandhi, A. Gupta, and S. Mukhopadhyay, JCAP **1705**, 002 (2017), arXiv:1612.02834 [hep-ph] .

[106] L. Necib, J. Moon, T. Wongjirad, and J. M. Conrad, Phys. Rev. **D95**, 075018 (2017), arXiv:1610.03486 [hep-ph] .

[107] H. Alhazmi, K. Kong, G. Mohlabeng, and J.-C. Park, JHEP **04**, 158 (2017), arXiv:1611.09866 [hep-ph] .

[108] H. Yüksel, S. Horiuchi, J. F. Beacom, and S. Ando, Physical Review D **76**, 123506 (2007).

[109] J. F. Navarro, C. S. Frenk, and S. D. M. White, The Astrophysical Journal **462**, 563 (1996).

[110] B. Moore, T. Quinn, F. Governato, J. Stadel, and G. Lake, Monthly Notices of the Royal Astronomical Society **310**, 1147 (1999).

[111] A. V. Kravtsov, A. A. Klypin, J. S. Bullock, and J. R. Primack, The Astrophysical Journal **502**, 48 (1998).

[112] C. Kachulis *et al.* (Super-Kamiokande), (2017), arXiv:1711.05278 [hep-ex] .

[113] G. L. Fogli, E. Lisi, A. Marrone, D. Montanino, and A. Palazzo, Physical Review D **66**, 053010 (2002).

Curriculum Vitae

Christopher J. Kachulis

590 Commonwealth Avenue
Department of Physics, Boston University
Boston, MA 02215, U.S.A.

Mobile: (413)230-7430
Office: (617)353-6040
E-mail: kachulis@bu.edu

EDUCATION

- Boston University, Boston, Massachusetts
  - **PhD** in Experimental Particle Physics, expected in May 2018
- Yale University, New Haven, Connecticut
  - **Bachelor of Science** in Physics, May 2011

RESEARCH EXPERIENCE

Super-Kamiokande Nov 2013 to present

Processed, analyzed, and visualized large complex datasets.

Trained, tested, and oversaw performance of neural network machine learning algorithm.

Developed analysis searching for boosted dark matter, setting first experimental constraints on such models. First author on paper submitted to *Phys. Rev. Lett.*

Analyzed atmospheric neutrino data for signs of Earth matter effects. Result included in paper accepted for publication in *Phys. Rev. D.*

Participated in large international collaboration, requiring communication and cooperation with colleagues from around the world.

Hyper-Kamiokande Dec 2014 to present

Created a C++ software package interfacing with neutrino interaction simulation software for Monte Carlo production. Used package for production of Hyper-K atmospheric neutrino and neutrino beam Monte Carlo. For code, see github.com/hyperk/NGen.

MiniCLEAN May 2012 to Apr 2014

Developed an event display written in C++ for both real-time and off-line visualization of MiniCLEAN data.

Performed cryogenic testing of photomultiplier tubes and built HV-block electronics cards.

Participated in assembly of MiniCLEAN detecor 6800 feet underground at SNOLAB in Ontario, Canada.

TEACHING EXPERIENCE

Boston University

PY 211 - General Physics

Led discussion sections, held office hours for students, graded homeworks and exams.

Undergraduate Tutor 2010-2011

Yale University

Tutored undergraduate students privately in Physics and Mathematics.

SELECTED PUBLICATIONS

Kachulis, C. *et al* (Super-Kamiokande) "Search for Boosted Dark Matter Interacting With Electrons in Super-Kamiokande." arXiv:1711.05278 [hep-ex], 2017. Submitted to *Phys. Rev. Lett.*

Abe, K. *et al* (Super-Kamiokande) "Atmospheric neutrino oscillation analysis with external constrains in Super-Kamiokande I-IV." arXiv:1710.09126 [hep-ex], 2017. Accepted to *Phys. Rev. D.*

A full list of publications can be found at inspirehep.net/author/profile/C.Kachulis.2.

REFERENCES

Edward P. Kearns

Professor of Physics — Phone: 617-353-3425

Department of Physics — E-mail: kearns@bu.edu

Boston University

Roger Wendell

Associate Professor of Physics — Phone: +(81) 075-753-3837

Physics Division II — E-mail: wendell.roger.4s@kyoto-u.ac.jp

Kyoto University